GEOMETRICALLY NONLINEAR FEATURES OF ACOUSTIC BLACK HOLE (ABH) BEAMS AND NONLINEARITY-ENHANCED ABH EFFECTS

XIANG SUN

PhD

The Hong Kong Polytechnic University

2024

The Hong Kong Polytechnic University

Department of Mechanical Engineering

Geometrically Nonlinear Features of Acoustic Black Hole (ABH) Beams and Nonlinearity-Enhanced ABH Effects

Xiang Sun

A thesis submitted in partial fulfillment of the requirements for the degree of Doctor of Philosophy

January 2024

CERTIFICATE OF ORIGINALITY

I hereby declare that this thesis is my own work and that, to the best of my knowledge and belief, it reproduces no material previously published or written, nor material that has been accepted for the award of any other degree or diploma, except where due acknowledgement has been made in the text.

(Signed)

Xiang Sun (Name of student)

Abstract

Acoustic black hole (ABH) techniques have demonstrated remarkable ability for passive vibration and noise control. As a result of a power-lawed thickness decrease, bending waves are slowed down to produce wave compression and energy concentration, conducive to vibration/sound radiation control and energy harvesting. However, the reduced thickness profile of a long and thin ABH beam poses a challenge for both numerical and experimental investigations. Particularly, a large vibration amplitude is produced around the ABH tip to result in significant geometric nonlinearities. In addition, manufacturing limitations may lead to imperfect geometry, such as initial curvature or a residual platform at the tip end of the beam, which can further affect the vibration responses of the nonlinear system. Besides, existing research shows that the ABH effect suffers from a deficiency at low frequencies, typically below the so-called cut-on frequency. Therefore, how to accurately model the geometric nonlinearity of ABH beams with imperfect geometry and to enhance the low-frequency ABH effect remains a bottleneck problem.

In the first part of this thesis, an inextensible condensation model, with the consideration of the initial curvature, is proposed based on a geometrically exact model for an Euler-Bernoulli cantilever beam. The free boundary of the cantilever gives rise to more significant longitudinal motion, which increases the inertia effects in the beam vibration which is in turn enhanced by the initial curvature. Specific techniques are proposed to numerically implement the developed model with increased accuracy and robustness. Numerical simulations are then conducted to validate the proposed model through comparisons with the finite element method (FEM), to

examine the assumptions underpinning the model and to explore the salient physical features, in particular the inertia-induced effects in both linear and nonlinear cases. Results show a decrease in the natural frequencies due to the initial curvature effect, a transition of the first mode from hardening to softening caused by enhanced curvature-induced inertia effect, and a pronounced asymmetry of the higher-order modes with respect to frequencies.

Then, the nonlinear features arising from these geometric factors in imperfect ABH beams are investigated, both numerically and experimentally. Geometric parameters of the ABH beams are updated according to the linear experimental results, which give a better geometry representation of the beams. Numerical results show that the hardening effect dominates in the first two modes of the perfect ABH beam due to the reduced nonlinear inertia effect by the tapered thickness. Then, geometric imperfections are intentionally introduced to the numerical model. With the consideration of the initial curvature, the hardening effect is enhanced by the locally curved ABH tip, which is different from its uniform counterpart, showing a hardening-to-softening transition for the first mode. With an embedded platform of uniform thickness at the free end of the beam, the linear and nonlinear responses are dependent on the platform length alongside enhanced geometric nonlinearities. As a result, the second mode becomes softening-dominant in the platform-embedded ABH beam. The nonlinear experiments confirm that the embedded platform is the major geometric imperfection in the sample. Both simulations and experiments demonstrate the geometrically nonlinear features of ABH beams.

Due to the inefficiency of geometric nonlinearity, mechanical nonlinearity is introduced

into a cantilever ABH beam to enhance the low-frequency ABH effect through low-to-high frequency energy transfer. Using a grounded cable with cubic stiffness, the sweeping results (with excitation frequency below the cut-on frequency) show that the displacement of the low-order modes of the nonlinear ABH beam decreases while the amplitude of its high-order harmonics increases compared to that of its linear counterpart, indicating a significant energy transfer phenomenon enabled by the cable in the nonlinear system. Due to the inherent ABH effect at high frequencies, the damped nonlinear ABH beam absorbs the transferred energy to result in a reduction of the vibration amplitude. To quantify the ABH effect under nonlinear conditions, the damping loss factor of the system is evaluated from energy viewpoint alongside the harmonic balance method. Below the cut-on frequency, the damping loss factor of some dominant modes in the ABH beam is drastically increased, indicating an enhanced ABH effect. This is also confirmed by the time response in the free decay test. Experiments demonstrate the energy transfer phenomenon and the efficient damping effect achieved in the nonlinear system.

As a final remark, the study sheds light on the physics behind the geometric and mechanical nonlinear features of ABH beams, alongside useful analysis and numerical tools in tackling such problems. Meanwhile, some promising solutions based on nonlinear principles to alleviate the low-frequency barrier of conventional ABH structures are examined. This constitutes a useful step forward in the ever-increasing endeavors that researchers are making on ABH technology.

Publications

Journal paper

[1] **X. Sun**, G. Kerschen, L. Cheng*, Geometrical nonlinearities in a curved cantilever beam: a condensation model and inertia-induced nonlinear features, Nonlinear Dynamics, 111 (2023) 6533-6556.

[2] **X. Sun**, G. Kerschen, L. Cheng*, Energy transfer for enhanced acoustic black hole effect through a cable-induced mechanical nonlinearity, International Journal of Non-Linear Mechanics, (2024) 104682.

[3] **X. Sun**, G. Kerschen, L. Cheng*, On the geometrically nonlinear features of ABH beams with imperfect geometry, Nonlinear Dynamics, (2024) under review.

[4] L. Zhang, **X. Sun**, J. Dietrich, G. Kerschen, L. Cheng*, Enhanced energy transfer and multimodal vibration mitigation in an electromechanical acoustic black hole beam, Journal of Sound and Vibration, 561 (2023) 117841.

[5] L. Xiao, **X. Sun**, L. Cheng, X. Yu*, A 3D-printed quasi-zero-stiffness isolator for low-frequency vibration isolation: modelling and experiments, Journal of Sound and Vibration, (2024) 118308.

Acknowledgements

I would like to express my sincere gratitude to my supervisor, Prof. Li Cheng, whose advice and encouragement have given me a deeper understanding of these thesis topics. It is my great honor and pleasure to study under his guidance and supervision. In addition, I have benefited greatly from his character and diligence, which I will cherish for the rest of my life.

I am also extremely grateful to Prof. Gaëtan Kerschen from University of Liège (UL) for his expert advice on the parts of mechanical coupling and nonlinear analysis in this thesis. Further, I am grateful to him for hosting me during my visit to Liège.

I would also like to thank every member of PolyU Cheng's team, Dr. Shuowei An, Dr. Tong Zhou, Dr. Linli Zhang, Dr. Linfeng Li, Dr. Lei Xiao, Mr. Ze Liu, Mr. Chen Gong, Miss Sihui Li, Mr. Yuanman Zhang, Mr. Yang Song, Mr. Le Chang, Mr. Jinze Li, Mr. Hangxing Li, Mr. Tingjian Li, Mr. Zengshen Yue, Mr. Rendong Pi, Mr. Yuanze Li, Miss Zhaohua Li, Miss Yuting Yang, and my friends Dr. Yanlin Xie, Dr. Ying Li, Dr. Haiyan Fan, Dr. Linyan Chen, who have kindly supported and accompanied me in the preparation of this thesis. I am especially grateful to Dr. Zongfei Tong, who has been a great support to me on my academic journey.

Finally, I would like to thank my parents for their unconditional love. Last but not least, I would like to thank my girlfriend for fully supporting me in my academic and personal decisions.

Contents

CERTIFICATE OF ORIGINALITY I

Abstract II

Publications V

Acknowledgements VI

Contents VIII

List of figures XI

List of tables XVIII

Chapter 1. Introduction 1

1.1 Background 1

1.2 Literature review on acoustic black holes 3

1.2.1 Fundamentals of acoustic black hole 3

1.2.2 Applications of acoustic black hole 9

1.2.3 Cut-on frequency of the ABH effect 17

1.3 Literature review on nonlinearities 18

1.3.1 Fundamentals of nonlinearity 18

1.3.2 Geometric nonlinearity of an initially curved cantilever beam 19

1.3.3 Numerical methods 22

1.3.4 ABH with nonlinearities 24

1.4 Existing problems and research objectives 26

1.4.1 Existing problems 26

1.4.2 Research objectives 27

1.5 Overview of the thesis 28

Chapter 2. Geometric Nonlinearities in a Curved Cantilever Beam 31

2.1 Introduction 31

2.2 Inextensible condensation model with initial curvature 33

2.2.1 Recap on geometrically exact model 33

2.2.2 Shortening effects and assumptions made for an inextensible condensation model 37

2.3 Modified harmonic balance method and generalized-α method 39

2.3.1 Modified harmonic balance method 41

2.3.2 Modified generalized-α method 44

2.4 Numerical results and analyses 51

2.4.1 Curvature-induced inertia/stiffness effects in linear models 51

2.4.2 Nonlinear dynamic features and curvature-induced inertia effect 60

2.5 Summary 69

Chapter 3. Geometrically Nonlinear Features of ABH Beams with Imperfect Geometry 72

3.1 Introduction 72

3.2 Numerical model and experimental setup 74

3.2.1 Recap on inextensible condensation model with initial curvature 74

3.2.2 Experimental setup 77

3.3 Numerical results 78

3.3.1 Updating of geometric parameters 78

3.3.2 Geometrically nonlinear features of ABH beams 82

3.4 Nonlinear experiments 93
3.4.1 Nonlinear modal behavior 93
3.4.2 Energy transfer 97
3.5 Summary 98
Chapter 4. Enhanced Acoustic Black Hole Effect through Energy Transfer Enabled by Intentional Mechanical Nonlinearity 101
4.1 Introduction 101
4.2 Nonlinear ABH beam 102
4.3 Numerical results and analyses 108
4.3.1 Convergency study 109
4.3.2 Linear characteristics of an ABH beam 112
4.3.3 Nonlinear dynamic features and enhanced ABH effects 119
4.4 Experimental confirmation 132
4.5 Summary 137
Chapter 5. Conclusions and Future Work 139
5.1 Conclusions 139
5.2 Suggestions for future research 143
References 145

List of figures

Fig 1.1 Schematic diagram of incident flexural wave propagation in a 1D ABH structure. 3

Fig 1.2 Double-layered compound ABH with (a) outer [36] and (b) inner damping materials [39]. 7

Fig 1.3 Convert 1D ABH to 2D circular ABH [40]. 8

Fig 1.4 (a)-(c) The simulated wave fields with the ray paths, and (d)-(f) the measured ones at different times. The curves with arrows represent the ray trajectories [10]. 9

Fig 1.5 1D ABH rod embedded in a tennis racquet grip covered by a thick absorbing layer [40, 42]. 10

Fig 1.6 (a) Fan blade profile with (a.1) and without (a.2) an ABH at the trailing edge. (b) Flow visualization diagram in cases of (b.1) the reference blade, the ABH blades (b.2) without damping layer, (b.3) with uniform damping layer, (b.4) with shaped damping layer [43]. 11

Fig 1.7 (a) Schematic diagram of the host beam with an ABH-RBD. (b) Experimental set-up. [44] 12

Fig 1.8 Different ABH DVA structures: (a) planar swirl-shaped ABH [45], (b) spiral ABH [46], (c) periodic add-on ABH [47], (d) 2D ABH [37]. 13

Fig 1.9 ABH engine cover (top view) and location of accelerometers on reference engine cover [53]. 14

Fig 1.10 A sonic black hole with perforated boundary [56]. 15

Fig 1.11 Schematic diagram of the coupled system with five identical ABH cells (top) and

the detailed FE model for a single ABH unit covered with PZT patch (bottom). [15] 16

Fig 1.12 Uniform beam (top), beam with periodic ABH elements without studs (middle), beam with periodic ABH elements with studs (bottom). [25] 17

Fig 1.13 Spectrogram of output acceleration for the ABH beam excited at 102 Hz. The excitation force increases from 0 to 15 N in 40 s. [113].....25

Fig 2.1 Definition of coordinate systems and relationship between the undeformed and deformed beam segments.....34

Fig 2.2 (a) Time responses obtained by the generalized-α method with and without OS technique, (b) close-up view taken in the stable region for a period. Note the two curves coincide perfectly so it is difficult to visually differentiate them.....50

Fig 2.3 (a) Residual and (b) minimum iteration in each time point obtained by the generalized-α method with and without OS technique. Note in Fig 2.3 (b), the method using OS needs only one iteration to reach the convergence.....50

Fig 2.4 Definition of the curved configurations for cantilever beam. 52

Fig 2.5 Linear FRFs at the free end tip. From (a) to (d): configuration (*i*)-(*iv*), respectively. 54

Fig 2.6 Normalized mode shapes for curved cantilever beams. Left to right: *u*, *v*.....56

Fig 2.7 $P1$ for different curved configurations. 59

Fig 2.8 The initial curvature effect of linear stiffness and inertia.....60

Fig 2.9 Comparisons of the HB method and the generalized-α method under 1.5 N force in the first mode for the curved beams with different initial curvature. (a) $k3 = 0$, (b)

$k3 = 0.3\pi$, (c) $k3 = 0.4\pi$, (d) $k3 = 0.5\pi$. Circle: reference solution for the straight beam. 62

Fig 2.10 NFR curves of the first mode with the various initial curvature and excitation level, as well as normalized harmonic coefficients. (a) NFR curves when $F0 = 0.5\ 1\ 1.5\ 2\ N$. Circle: reference solution. The first six harmonic coefficients at the forcing level of 2 N: (b) $k3 = 0$, (c) $k3 = 0.3\pi$, (d) $k3 = 0.4\pi$, (e) $k3 = 0.5\pi$. 65

Fig 2.11 NFR curves of higher modes with various initial curvatures and forcing levels. (a)-(b): Mode 2 at the forcing level of 6 N and 12 N, respectively. (c)-(d): Mode 3 at the forcing level of 6 N and 12 N, respectively. Circle in (a)-(b): reference solution of the second mode for the straight beam. 67

Fig 2.12 (a) NFR curves for the first mode when $F0 = 1.5\ 2\ 3\ N$. (b) Normalized harmonic coefficients at the forcing level of 3 N..... 68

Fig 2.13 Normalized harmonic coefficients of the first mode for different curved length at the forcing level of 2 N. Solid line: $lc/L = 0.2$. Dashed line: $lc/L = 0.1$. 69

Fig 3.1 An ABH beam with a curved and thin end tip. 73

Fig 3.2 Deformation relationship of a beam segment. 75

Fig 3.3 Experimental setup. 77

Fig 3.4 Schematic diagram of a straight cantilever ABH beam. 79

Fig 3.5 Comparisons of the experiment and the updated model. (a) FRF, (b) Phase angle. 81

Fig 3.6 NFR curves of the perfect ABH beam around the first three modes. (a)-(c): Modes N1-N3, (d) Mode N2, $Fext = 3$ N..... 85

Fig 3.7 FRFs of the curved ABH beam with $rc = 1$: (a) $k3 = 0.1\pi$, (b) $k3 = 0.5\pi$. ..86

Fig 3.8 NFR curves of the locally curved ABH beam: (a) Mode N1, $rc = 0.108$, $Fext = 50N$, (b) Mode N2, $rc = 0.108$, $Fext = 5N$, (c) Mode N3, $rc = 0.218$, $Fext = 5N$. ..87

Fig 3.9 Schematic diagram of a platform-embedded ABH beam. ..88

Fig 3.10 FRFs of the ABH beam with an embedded platform: (a) $rpf = 0 - 0.02$, (b) $rpf = 0.03 - 0.04$. ..90

Fig 3.11 Phase angle of the ABH beam with a platform $rpf = 0.036$. ..90

Fig 3.12 Normalized mode shapes of the ABH beam. (a) Mode N1, (b) Mode N2. ..91

Fig 3.13 NFR curves of the ABH beam with an embedded platform: (a) $rpf = 0$, (b) $rpf = 0.01$, (c) $rpf = 0.03$, (d) $rpf = 0.036$. Left to right column: Mode N1, Mode N2. ..93

Fig 3.14 Parametric studies of damping loss factors of the platform-embedded ABH beam ($rpf = 0.036$) around modes M2 and N2, $Fext = 1$ N. (a) Linear loss factor η with $\eta nl = 0$, (b) nonlinear loss factor ηnl with $\eta = 0.001$. ..94

Fig 3.15 Comparisons between the experimental results and NFR curves of the numerical model ($rpf = 0.036$, $\eta = 0.001$, $\eta nl = 0.012$) around modes M2 and N2. (a) $Fext = 0.1$ N, (b) $Fext = 0.3$ N, (c) $Fext = 0.5$ N, (d) $Fext = 1$ N. ..96

Fig 3.16 (a) Normalized mode shape of the perfect ABH beam for mode N1 and the imperfect ABH beam for mode N2, (b) potential energy ratio of the platform-embedded ABH beam $rpf = 0.036$ with different forces. ..97

Fig 3.17 Comparison of output velocity for ABH beams with free end and nonlinear cable,

$U = 0.1V$ 98

Fig 4.1 Schematic picture of a cantilever ABH beam with damping layers and grounded nonlinear cables. 103

Fig 4.2 Schematic plot of the beam cross section with two grounded cables. 104

Fig 4.3 Diagram of a NFR curve in the frequency domain. 108

Fig 4.4 Element nodes distribution of 1D beam element in the ABH beam. 110

Fig 4.5 NFR curves of the damped ABH beam with different meshes around the first mode with $NH = 5,\ k3 = 109\ N/m3$ and $Fext = 5$ N. 111

Fig 4.6 NFR curves of the damped ABH beam with different NH around the first natural frequency with regular mesh, $k3 = 109\ N/m3$ and $Fext = 5$ N. 112

Fig 4.7 Mesh distribution in the FEM model with two damping layers. 113

Fig 4.8 Linear FRFs of the uniform beam and the ABH beam at $x = x0$. 115

Fig 4.9 Normalized mode shapes with damping layers. (a) Mode 1, (b) Mode 3, (c) Mode 5, (d) Mode 7 116

Fig 4.10 Damping loss factors of the uniform beam and the ABH beam. 118

Fig 4.11 FFT results of a sweep below the cut-on frequency for the linear (LN) and nonlinear (NL) damped ABH beams, $Fext = 1\ 3\ 5\ 20$ N. 121

Fig 4.12 FFT results of a sweep for the undamped ($\eta d = 0$) and damped ($\eta d = 0.3$) nonlinear ABH beams, $Fext = 1\ 3\ 5\ 20$ N. 122

Fig 4.13 (a) Damping loss factor, and (b) the third normalized harmonic close to the first mode. Dot ● in (a) represents the maximum on the curve, and the point with same sequence in (b). 124

Fig 4.14 Normalized time-domain system responses with $Fext = 0.1$ N, $f = 31$ Hz (frequency at highest point in Fig 4.13(a)). Dot ● on the displacement curve represents the maximum value during a period, and the other two points on velocity and acceleration curves are the corresponding values at the same time. 125

Fig 4.15 Free decay curves and spectrograms for the first mode. (a)-(b): normalized displacement, (c)-(d): normalized acceleration. 127

Fig 4.16 Free decay curves of normalized energy for the first mode. 127

Fig 4.17 (a) Damping loss factor around the second mode, and (b) the third normalized harmonic. Free decay curves: (c) Normalized acceleration, (d) normalized energy. 128

Fig 4.18 Damping loss factors of the linear and nonlinear systems for $Fext = 5$ N...129

Fig 4.19 ΓPE of the nonlinear system with the grounded cable at the ABH tip and $\eta d = 0$.....131

Fig 4.20 Damping loss factors of the nonlinear system with the grounded cable at $x = 87\ mm$. 132

Fig 4.21 Experimental configuration and setup. 133

Fig 4.22 Experimentally measured displacement at $x = 200\ mm$ of a bare ABH beam without the cable. (a) FRF, (b) coherence. 134

Fig 4.23 Measured velocity (sweep below the cut-on frequency) of the nonlinear ABH beam with the cable. (a). Different excitation voltages without damping layers, (b) multiple damping layers with $U = 0.1\ V$. 136

List of tables

Table 3.1 Parameters of the ABH beam. 79

Table 3.2 Resonant frequencies (Hz) of the experiment and the updated model..... 82

Table 3.3 Geometric parameters of the ABH profile. 82

Table 4.1 Geometric and material parameters of the beam and damping layer. 109

Table 4.2 Natural frequencies results calculated from coarse, regular, and fine meshes, respectively. 111

Table 4.3 Natural frequencies (Hz) obtained from FEM with elements of different orders. 113

Table 4.4 Resonant frequencies of the experimental setup without the damping layers and the cable. 134

Chapter 1. Introduction

1.1 Background

Modern society suffers from increasing noise and vibration problems. Apart from the obvious environmental noise issues and their impact on our everyday life, in most engineering practice, structural vibration is regarded as a negative issue, which adversely affects mechanical properties, aggravates fatigue and wear, even causes the destruction of structures [1, 2]. In this regard, developing innovative ideas and technological know-how for conceiving engineering structures with capabilities such as light weight, high vibration damping, and good noise insulation has always been the hot spot in the acoustic and vibration community.

Among numerous passive control methods, acoustic black hole (ABH) is a feasible technique which has aroused intense and ever-increasing interests over the past decades [3-5]. A typical beam or plate-like ABH structure has a tapered thickness profile, so that the local phase (and the group) velocity of the incident bending wave slows down as it propagates along the ABH beam towards the thinner part and, ideally, tends to zero as the structural thickness approaches zero. This wave retarding phenomenon results in well-known ABH effects, including neutralized wave reflection and energy concentration/focalization [6-11], which are conducive to conceiving novel engineering solutions. For example, exploiting these features, lightweight and highly damped structures can be designed with a small amount of damping layer [12, 13], while an efficient energy harvesting (EH) device can be realized using

piezoelectric (PZT) patches [14-17]. In addition, the phase velocity reduction of the bending waves in ABH structures effectively reduces the acoustic radiation efficiency in the free field [18-22] or the structure-acoustic coupling in an enclosed space [23, 24]. Studies in one-dimensional (1D) or two-dimensional (2D) periodic lattices have shown that a combination of ABH-induced local resonance and Bragg scattering can induce wide band gaps [25-29].

Existing research shows that the aforementioned ABH effect excels in vibration suppression and noise attenuation mainly at high frequencies but shows a deficiency below the so-called cut-on (or characteristic) frequency [26]. Past attempts to reduce the frequency limit have been achieved by extending the effective ABH length, at the expenses of generating two potential issues, i.e., geometric nonlinearities and imperfect geometry (initial curvature or a residual platform), which may affect the ABH effect and hamper the fundamental understanding of nonlinear dynamic behaviors of ABH beams. Meanwhile, such large structures challenge current manufacturing capabilities and affect the acceptance of the structures. To enhance ABH effects with a reasonable physical size, intentional mechanical coupling with strong nonlinearities can be a useful approach. Due to the generation of super harmonics, nonlinearity can transfer energy into the high frequency range where the ABH effect comes into play, which is expected to improve the performance of ABH in the lower frequency band, and it is at the root of this thesis. In the following, relevant existing work pertaining to ABHs and nonlinearities are reviewed.

1.2 Literature review on acoustic black holes

1.2.1 Fundamentals of acoustic black hole

Following the concept of the black hole in astrophysics, acoustic black hole (ABH) has been proposed in the field of wave motion and vibration and has garnered growing interest from the engineering community in the last decade [3]. The typical ABH phenomenon was firstly reported in 1988 by Mironov [6]. In that work, the thickness of a tapered 1D structure decreases smoothly following a power-law profile, i.e., $h(x) = \varepsilon x^m (m \geq 2)$, which leads to a reduced propagation velocity of bending waves within the ABH portion. In an ideal scenario, wherein the thickness at the ABH end is diminished to zero, the phase and group velocity tend towards zero concurrently. As a result, the incident flexural wave is incapable of advancing towards the ABH end, leading to the emergence of quasi-zero wave reflection and energy concentration. Meanwhile, the wavelength λ is compressed and the magnitude of vibration at the ABH end increases, ideally, to infinity. The wave propagation in a 1D ABH structure is shown in Fig 1.1.

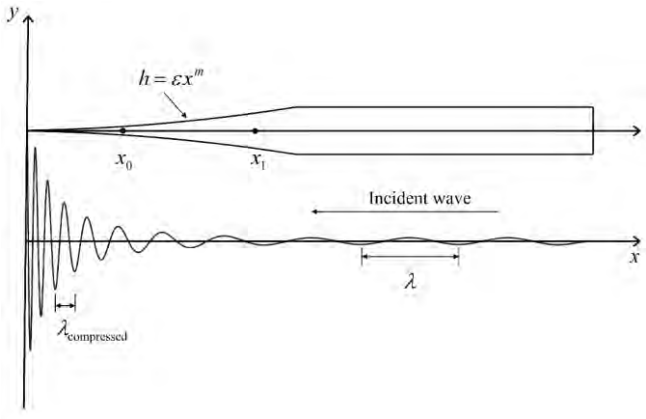

Fig 1.1 Schematic diagram of incident flexural wave propagation in a 1D ABH structure.

To uncover the mechanism of the ABH phenomenon, the geometric acoustic approximation (GAA) method [6-8] was utilized to illustrate flexural wave propagation in elastic beams and plates. The local wave number in a 1D beam with rectangular cross section follows $k(x) = \sqrt[1/4]{3\rho\omega^2/Eh^2(x)}$, in which ρ, E and h are the density, Young's modulus and half thickness of the structure (Fig 1.1); ω is the angular frequency. Therefore, the phase velocity c_p and the group velocity c_g in a tapered structure following a power-law profile $h(x) = \varepsilon x^m (m > 0)$ are given by

$$\begin{aligned} c_p &= \frac{\omega}{k} = \varepsilon^{1/2}\left(\frac{E\omega^2}{3\rho}\right)^{1/4} x^{m/2} \\ c_g &= \frac{\partial\omega}{\partial k} = 2\varepsilon^{1/2}\left(\frac{E\omega^2}{3\rho}\right)^{1/4} x^{m/2} \end{aligned}, \tag{1.1}$$

where both c_p and c_g tend to zero as $x \to 0$, indicating the presence of wave retarding in such tapered structure. Then, the transit time of a wave from x_1 to x_0 is

$$T = -\int_{x_1}^{x_0} \frac{dx}{c_g} = \begin{cases} \dfrac{1}{\varepsilon^{1/2}\left(\dfrac{E\omega^2}{3\rho}\right)^{1/4}(2-m)}\left(x_1^{(2-m)/2} - x_0^{(2-m)/2}\right), & 0 < m < 2 \\ \dfrac{1}{2\varepsilon^{1/2}\left(\dfrac{E\omega^2}{3\rho}\right)^{1/4}} \ln\left(\dfrac{x_1}{x_0}\right), & m = 2 \\ \dfrac{1}{\varepsilon^{1/2}\left(\dfrac{E\omega^2}{3\rho}\right)^{1/4}(m-2)}\left(\dfrac{1}{x_0^{(m-2)/2}} - \dfrac{1}{x_1^{(m-2)/2}}\right), & m > 2 \end{cases} . \tag{1.2}$$

Eq.(1.2) shows that, for the profile with $0 < m < 2$, the transit time T is finite and wave reflection occurs even though the configuration impairs the wave speed as $x \to 0$ (Eq.(1.1)). However, for the profile with $m \geq 2$, the flexural wave from the uniform part cannot reach the beam end in any finite time as $x_0 \to 0$, resulting in zero wave reflection and high energy

concentration. With proper damping treatment, total energy absorption can be achieved. The combination of energy concentration and dissipation accounts for the ABH phenomenon.

Unfortunately, zero thickness in an ideal ABH structure is not possible due to manufacturing limitations, thus creating a truncated thickness at the end of a 1D structure, which is detrimental to the ABH phenomenon. The reflection coefficient R_0 can be used to evaluate the ABH effect. With introduction of damping effects, the local wave number $k(x)$ has an imaginary part. By integrating $\mathrm{Im}k(x)$ from x_1 to x_0, R_0 is expressed by [6, 8]

$$R_0 = \exp\left(-2\int_{x_1}^{x_0} \mathrm{Im}\, k(x)dx\right), \tag{1.3}$$

which varies between 0 and 1. With any infinitely small damping, such as structural damping, R_0 approaches zero as $x_0 \to 0$ in an ideal ABH beam, indicating total energy absorption and no wave reflection. Nevertheless, even a small truncation thickness will result in a significant increase in the reflection coefficient R_0 which can reach as large as 0.5-0.7 [6, 8]. To counter this, a feasible solution was offered by deploying damping layers over the ABH end. Analytical results showed that a small amount of damping layers can significantly reduce the reflection coefficient R_0. This effect is more pronounced for the structural profile with a higher value of m [8].

Restricted to the assumptions of the geometric acoustics, the damping layer thickness should be sufficiently less than the structural thickness, whereas this cannot be assured in the ABH end region, which, therefore, challenges the optimization design of the damping layer. To

overcome this, Georgiev *et al.* [12] proposed the impedance matrix (IM) method, a more reliable approach with less hypotheses, to investigate damping performance of ABH structures. Furthermore, considering finite structures, semi-analytical (SA) methods [13, 30-33] based on the Lagrange variational principle have been developed. By including energy terms into the Lagrangian function, it becomes possible to achieve complete description of the coupling between damping layers or piezoelectric layers and the host system. In addition, the utilization of wavelet basis allows for more precise wave modeling near the ABH end, especially for high-order modes, which is challenging to achieve with alternative numerical techniques. The numerical results were verified experimentally [13, 31, 33]. Apart from above methods, the finite element method (FEM), a more general and efficient simulation approach, was utilized for multiple investigations on embedded or integrated ABH structures [17, 18, 23-25, 34-37].

Although 1D ABH structures have shown superior performance in terms of structural vibration reduction, their fragile outer tips are prone to tearing and damage. One possible solution is to place the ABH tip inside a structure, which is referred to as double-layered compound ABH structures [35, 38], as shown in Fig 1.2. Damping materials can be deployed outside or inside the structure, while the latter (Fig 1.2(b)) would provide extra stiffness to improve the overall structural load-bearing capacity. Moreover, a strengthening stud proposed in [25] can go even further in this regard.

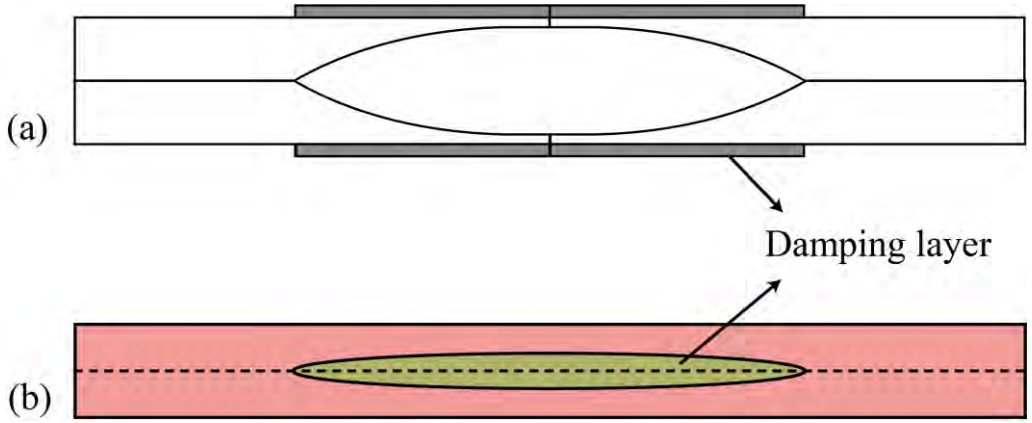

Fig 1.2 Double-layered compound ABH with (a) outer [35] and (b) inner damping materials [38].

From another perspective, the fragile wedges of an ABH can be hidden inside the structures like plates. Specifically, a 2D ABH structure can be obtained by rotating a cross section of a 1D ABH structure around the tip [39], as shown in Fig 1.3. Similarly, the thickness of 2D ABH decreases as a power-law function of radius. When bending waves propagate into the ABH area, the wave direction will be deflected, and the velocity will gradually decrease. Ideally, the bending waves will be concentrated in the center of the ABH, and the propagation velocity will decrease to zero. An important practical advantage of using 2D black holes is that they are relatively easy to make. The simplest way to make a 2D black hole is to use a circular steel blade to drill a dimple until the blade almost protrudes. The resulting spherical shape approximates the required quadratic profile near the center of the pit, making it behave like a black hole.

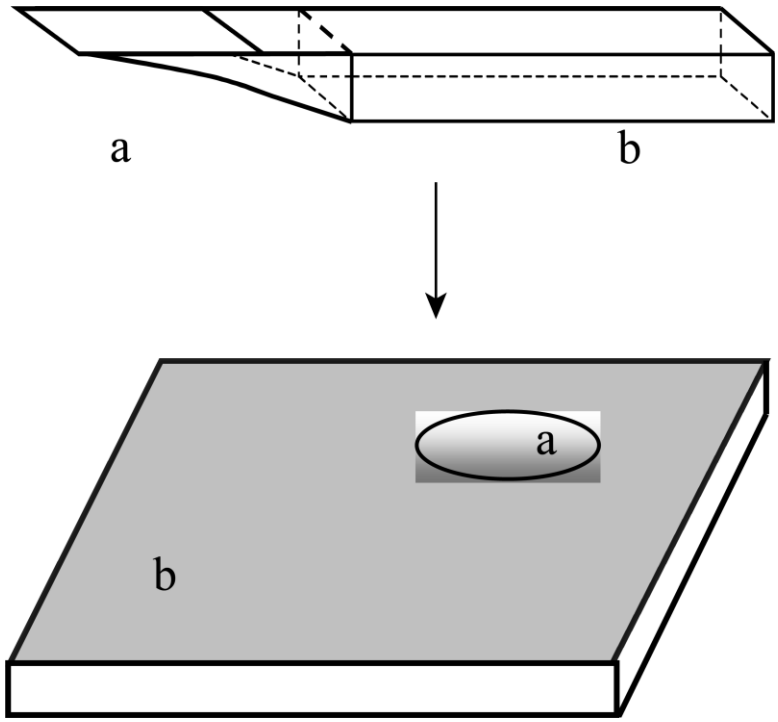

Fig 1.3 Convert 1D ABH to 2D circular ABH [39].

Unlike wave propagation in 1D structures, flexural waves in 2D structures can propagate in any direction within the plane. Thus, 2D ABH structures can manipulate the direction of wave propagation. Huang *et al.* [10] investigated wave propagation process in 2D circular ABH with a central plateau. Fig 1.4 shows a good agreement of the numerical and experimental results at different times. Both results demonstrate that the propagation path of the incident wave changes as it passes through the ABH structure and becomes focused in the vicinity of the ABH tip, not exactly at the ABH center. Meanwhile, the wavelength decreases as the thickness decreases. Besides, the truncation thickness results in a weakening of the focusing features. Aklouche *et al.* [40] studied the scattering properties of flexural waves from a 2D circular ABH, seen as a penetrable scatterer. The results show that the ABH functions as a resonant scatterer.

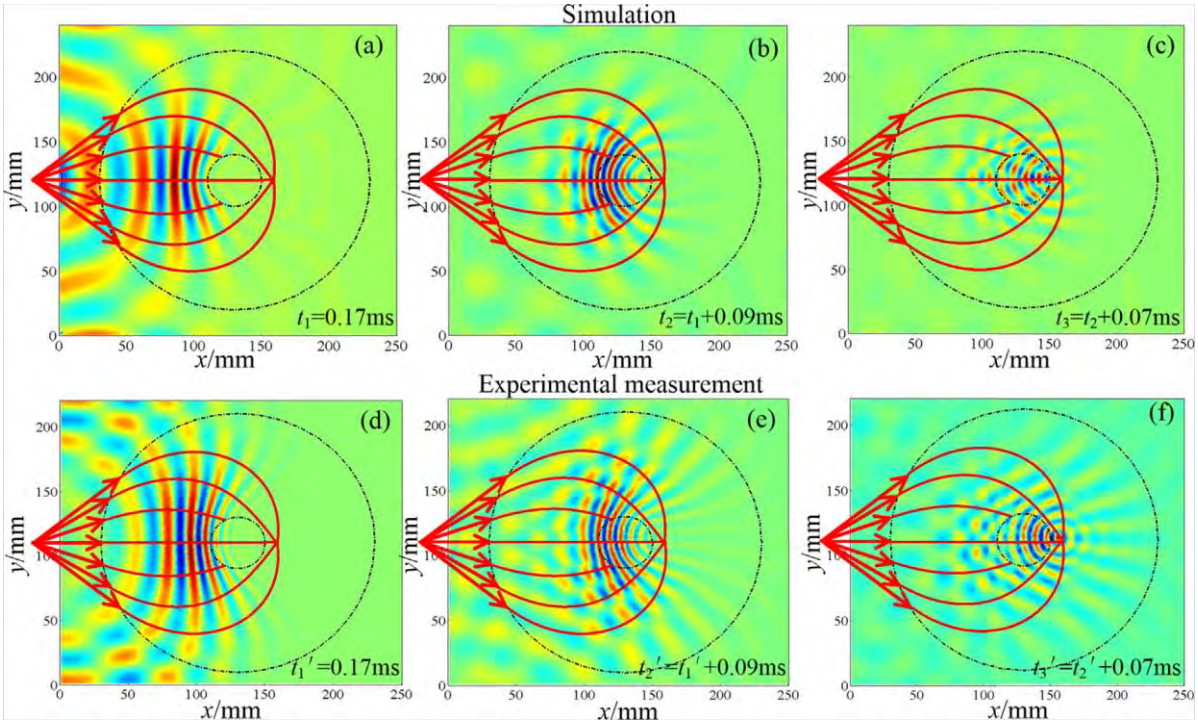

Fig 1.4 (a)-(c) The simulated wave fields with the ray paths, and (d)-(f) the measured ones at different times. The curves with arrows represent the ray trajectories [10].

1.2.2 Applications of acoustic black hole

1). Vibration suppression

Due to high damping effects and unique wave propagation patterns, ABH structures have a wide range of applications in the field of noise and vibration reduction. By tailoring the thickness of part of the structure following a power-law function, a 1D ABH rod is embedded in the tapered cylindrical rod [41], whose sharp end is covered by an absorbing layer for efficient vibration suppression. By deploying a thick absorbing layer as shown in Fig 1.5, impact-induced resonant vibrations in the primary structure of tennis racquets can be effectively attenuated [39]. Such an implementation can be applied not only to the structure

with a uniform thickness, but also to the one with a tailoring profile. A well-known example is the turbofan blade made from a streamlined body, which has a tapered profile at the trailing edge as shown in Fig 1.6(a.2). As the blades of jet engines rotate at high speeds, fluctuations in the lift force acting on the blades give rise to significant structural vibrations, which is the primary cause of engine failure. A feasible solution is to embed an ABH at the trailing edge of the blade airfoil, as shown in Fig 1.6(a.1). Compared to the reference blade, the ABH blade covered by damping layers achieves significant vibration reduction [42]. However, the ABH blade with and without damping layers breaks the laminar flow and induces flow separation (shown in the flow visualization diagram Fig 1.6(b.2)-(b.3)), resulting in increased turbulence and lower efficiency. To counter this, the damping layer is shaped to recreate the original profile. Fig 1.6(b.4) shows that the refined configuration remains laminar flow.

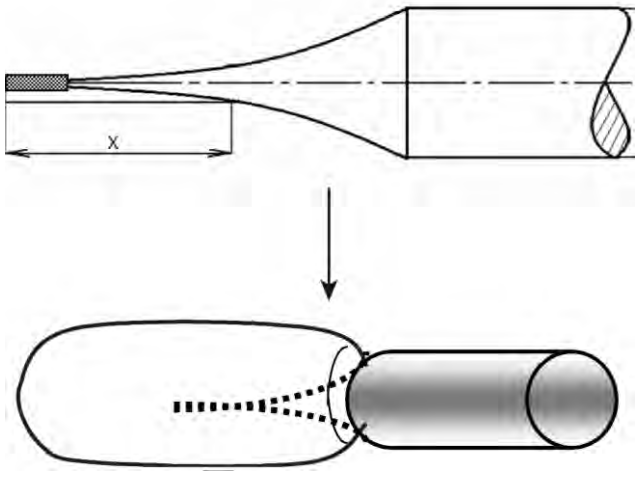

Fig 1.5 1D ABH rod embedded in a tennis racquet grip covered by a thick absorbing layer [39, 41].

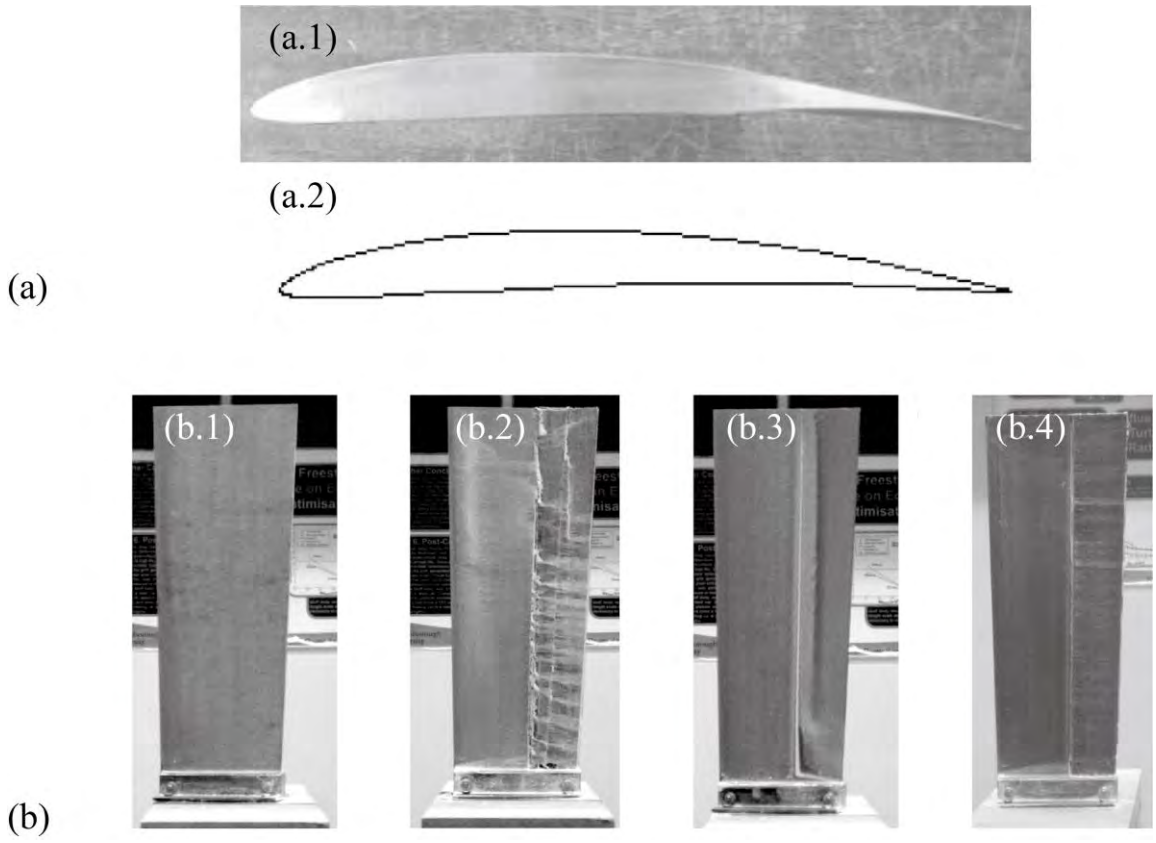

Fig 1.6 (a) Fan blade profile with (a.1) and without (a.2) an ABH at the trailing edge. (b) Flow visualization diagram in cases of (b.1) the reference blade, the ABH blades (b.2) without damping layer, (b.3) with uniform damping layer, (b.4) with shaped damping layer [42].

Although ABH embedded structures are lightweight and highly damped, their tailoring thickness reduces the load-bearing capacity and limits their application. Recently, ABHs have become increasingly popular as add-on devices. A dynamic vibration absorber (DVA) is a common vibration suppression method that attenuates the resonance peak through interactions between the add-on device and the host structure, which is normally tuned to the target resonance peak but can hardly be extended to a wide frequency bandwidth. However, Zhou and Cheng [43] achieved broadband vibration suppression of a host beam by attaching an ABH-

featured resonant beam damper (ABH-RBD) (Fig 1.7), which maximized both the structure interaction and the highly damping effect. Additionally, 1D straight ABHs exhibit a strong orientation dependence, which hinders their application in the 2D vibration field where waves propagate along various directions [44]. This issue was also mentioned in [45]. Therefore, the planar swirl-shaped ABH absorber (Fig 1.8(a)) [44] was proposed to entail broadband and multi-directional vibration suppressions for a vibrating structure. Meanwhile, such configuration, as well as spiral ABH (Fig 1.8(b)) [45], would reduce space occupation. The periodic add-on ABH-DVA (Fig 1.8(c)) [46] was investigated through exact dynamic stiffness method. The results show that the periodic arrangement of multiple ABH beams causes multiple local resonant bandgaps for broadband vibration suppression. Despite these efforts made on 1D ABH DVAs, excellent vibration reduction in multiple directions requires substantial add-on devices, which is considered a limitation. Obviously, a 2D ABH structure with richer modes and multidirectional features is appropriate for this problem. In [36], a single 2D circular ABH was proposed as an auxiliary add-on device for the vibration suppression in a 2D structure.

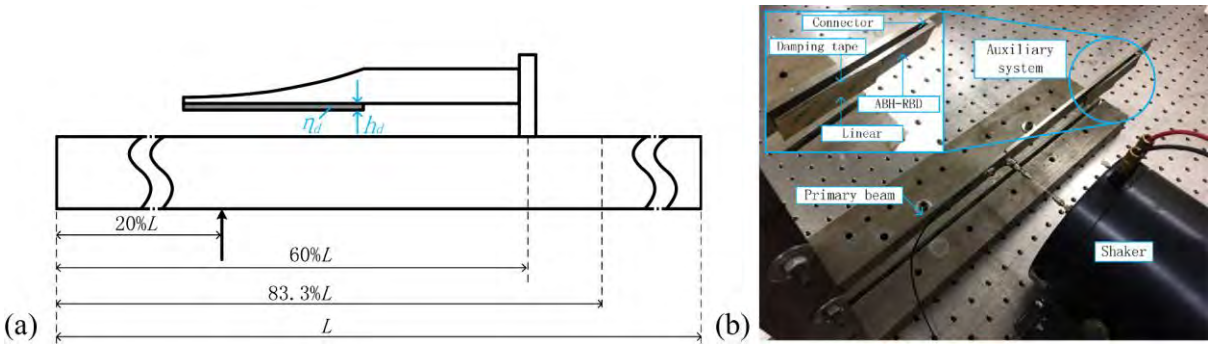

Fig 1.7 (a) Schematic diagram of the host beam with an ABH-RBD. (b) Experimental set-up. [43]

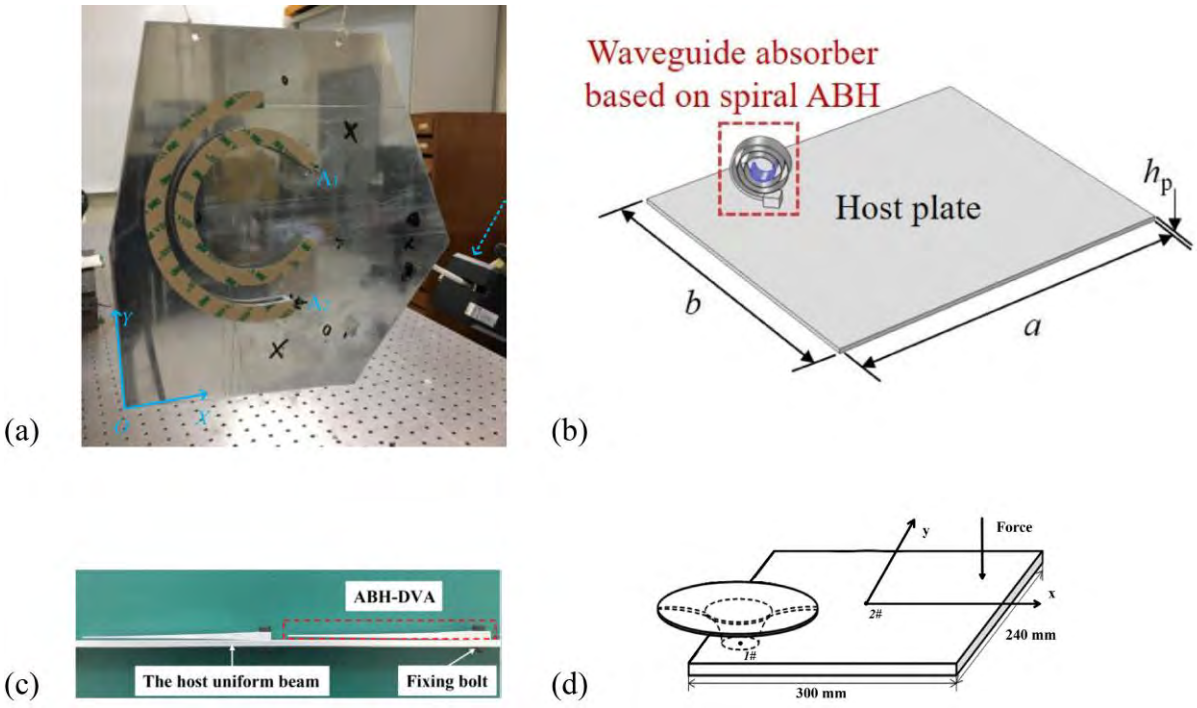

Fig 1.8 Different ABH DVA structures: (a) planar swirl-shaped ABH [44], (b) spiral ABH [45], (c) periodic add-on ABH [46], (d) 2D ABH [36].

2). Noise attenuation and sound absorption

Except for vibration suppression, the wave retarding phenomenon in ABH structures provides a useful approach to addressing vibro-acoustic issues. Initially, experiments [47, 48] show that, compared to the uniform plate, the ABH embedded plate with damping layers exhibits a significant decrease in the radiated sound power. Subsequently, numerical analyses revealed and analyzed the mechanism of this phenomenon [18, 19, 22, 49]. In fact, the sound radiation of a structure reaches its peak when the wave speed of the bending wave matches the speed of sound in air. Due to the ABH effect, the supersonic waves (compared to the sound speed) in the uniform part of the plate are greatly reduced to subsonic waves in the ABH region, resulting in a significant reduction of the sound radiation efficiency in the free field. Besides,

the embedded ABH reduces the coupling strength between the plate and the cavity, which allows for significant noise attenuation inside the cavity [23, 24, 50, 51]. Preliminary efforts have been made to use ABH structures for noise control in practical applications. Bowyer and Krylov [52] investigated an engine cover with multiple ABH indentations (Fig 1.9), and measured the sound pressure around the engine by multiple condenser microphones. The results show that the ABH engine cover leads to an average reduction of 6.5dB from the reference sample.

Fig 1.9 ABH engine cover (top view) and location of accelerometers on reference engine cover [52].

Recently, the sonic black hole (SBH) structure has been proposed as the sound counterpart of the structural ABH. This structure involves various rings inside a duct, which impairs the propagation velocity of sound and traps wave energy [53]. Combined with Micro-perforated panel (MPP), the SBH with perforated boundary (shown in Fig 1.10) achieves broadband quasi-zero wave reflection and sound absorption, both numerically and experimentally [54, 55].

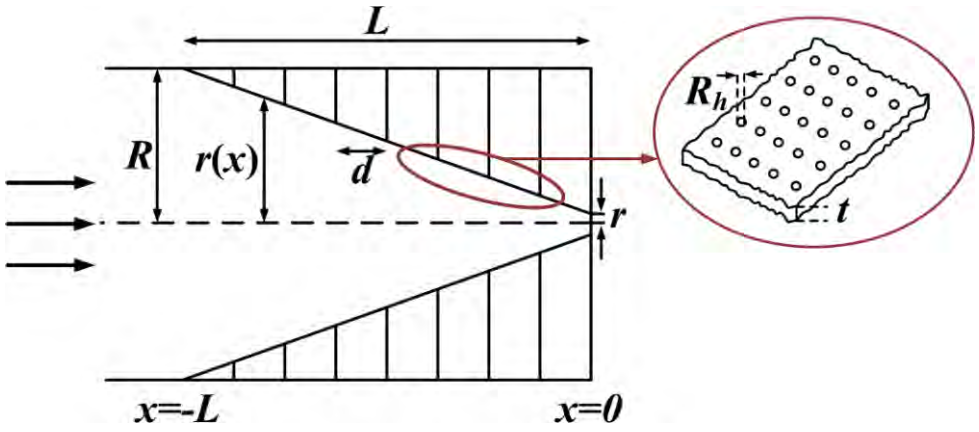

Fig 1.10 A sonic black hole with perforated boundary [55].

3). Energy harvesting

The intense energy focalization in ABH structures contributes to the development of highly efficient vibration-based energy harvesting (EH) devices. Zhao *et al.* [15] first developed a fully coupled electromechanical model consisting of five ABH cells, each covered with a uniform piezoelectric patch (shown in Fig 1.11). Simulation results show that the ABH embedded structure exceeds the conventional structure in terms of energy harvesting. Such observation was experimentally verified in [56]. Ji *et al.* [17] proposed an enhanced EH device using compound ABHs. For this structure, the coated PZT patches are sliced into multiple microarrays to avoid neutralization of positive and negative electrical charges on the PZT surfaces, thus effectively extracting mechanical energy. Different from the above case-by-case analysis, Zhang *et al.* [14] established a semi-analytical model considering the full coupling among various electromechanical components in the system. The results show that ABH effects result in effective and broadband EH when the system is properly designed, by taking into account the PZT layout in terms of wavelength and frequency range. Further, Li et al. [57]

performed a systematic parameter optimization of the harvested power using a modal-based analysis.

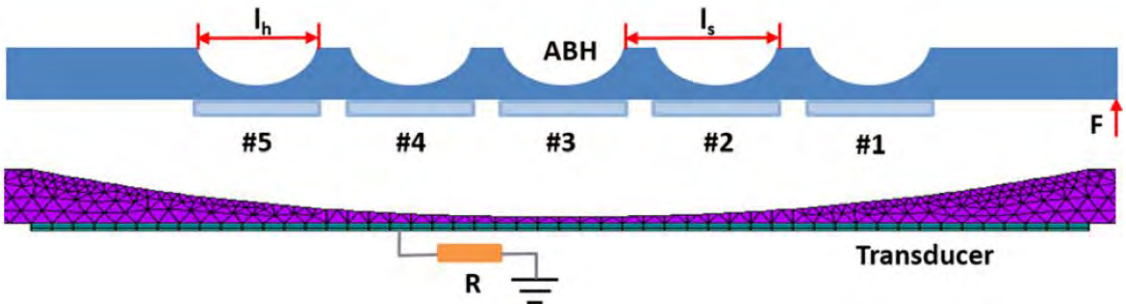

Fig 1.11 Schematic diagram of the coupled system with five identical ABH cells (top) and the detailed FE model for a single ABH unit covered with PZT patch (bottom). [15]

4). Metamaterial structures

Acoustic metamaterials with repeating elements have shown excellent performance in wave manipulation, such as band gaps [58], wave front manipulation [59], and robust wave transport [60], etc. Among them, the band gaps caused by Bragg scattering [61] or local resonance [62] have promising applications in vibration isolation and noise reduction. Nevertheless, the conventional method of multiple local resonators is deficient in terms of efficiency and implementation. To solve this problem, Tang and Cheng [26] investigated an infinite structure with periodic ABH elements via semi-analytical method. The results show that a few ABH elements can generate broadband attenuation bands, as a result of the local resonances of the ABH elements. Further, strengthening studs were installed in double-leaf ABH structures, as shown in Fig 1.12. Due to the impedance mismatch between the stud and the ABH, Bragg scattering was generated to extend band gaps [25, 27]. Additionally, periodic

ABH components have been attached to the host structure as add-on devices to mitigate vibration, as studied in [29, 46].

Fig 1.12 Uniform beam (top), beam with periodic ABH elements without studs (middle), beam with periodic ABH elements with studs (bottom). [25]

1.2.3 Cut-on frequency of the ABH effect

Although ABH structures exhibit exceptional properties at high frequencies, their low-frequency effects are deficient, especially below the cut-on frequency [18]. As the half incident bending wavelength is typically longer than the ABH length, i.e. $\lambda/2 \geq L_{ABH}$, it is challenging for the bending wave to enter the ABH part, which leads to insufficient energy concentration and a reduced damping effect. In addition, the wave-based analysis gives an analytical definition of the cut-on frequency for the ABH profile with $m = 2$, which is the threshold for wave propagation in the ABH part [40, 63]. The unavoidable truncated thickness will also shorten the effective length of the ABH, which further jeopardizes the application of the ABH at low frequencies. Therefore, considerable research efforts have been made to broaden the effective frequency band of ABH. The extension of the ABH length is a prevalent

and straight forward approach to reduce the frequency threshold. By adding an extended platform of constant thickness at the ABH tip, the low-frequency ABH effects can be enhanced by increasing the effective ABH length without over-tailoring, as demonstrated in [64]. Long spiral ABH beams were also utilized to reach a broadband vibration reduction and reduce space occupation [65]. Meanwhile, periodic ABH structures can be used to increase the effective ABH length [18]. Another strategy is to design embedded ABH structure by using the concept of a metamaterial [21, 66], or DVA [67]. Recently, Quaegebeur *et al.* [68] replaced a mechanical ABH by a digital controller to create the so-called virtual acoustic black hole (VABH). Ideally, the infinite ABH length can be realized by proper digital design so that the cut-on frequency can theoretically approach zero. However, the abovementioned implementations challenge current manufacturing capabilities and affect the acceptance of the structures. Therefore, how to improve the ABH effect below the cut-on frequency is still a bottleneck problem.

The nonlinearity-induced energy transfer phenomenon offers a feasible solution to inefficiency of ABH effect. In the following, intrinsic nonlinearities of beams with initial curvature and ABH with nonlinearities are reviewed.

1.3 Literature review on nonlinearities

1.3.1 Fundamentals of nonlinearity

Nonlinearity is a rich phenomenon existing in nature and our daily life. The most famous

nonlinear phenomenon is the turbulence in hydrodynamics, which displays the perturbation from the uniform flow and chaos, known as “butterfly effect” [69]. Nonlinear phenomenon provides great additional design flexibility and opens up new horizons in diverse disciplines. Strong nonlinearity is now exploited in a variety of mechanical and physical applications including metamaterials [70], nonlinear vibration absorbers and energy harvesters [71-73] , and nano- and micro-electromechanical systems [74] etc. Well-known features of nonlinear system display the generation of multiple harmonics [75], even when the system is excited at one specific frequency. This particular dynamic mechanism has been exploited for several decades to transfer energy from across different frequency ranges. However, the geometric and mechanical nonlinearities are generated from different sources, thus leading to sophisticated nonlinear behaviors, whose handling is both technically challenging and practically important.

1.3.2 Geometric nonlinearity of an initially curved cantilever beam

Towards the tapered end tip of an ABH beam, the reduced local phase and group velocities and the resulting energy accumulation lead to much amplified vibration amplitude and non-negligible geometric nonlinearities. Meanwhile, due to manufacturing imperfection, the tip region of an ABH is unavoidably curved, which may further enable additional nonlinear dynamic behaviors. The ultimate nonlinear modal behavior (hardening or softening) in such structures is determined by the domination level of nonlinear stiffness and nonlinear inertia. Moreover, the consideration of the initial curvature creates additional challenges in both system

modelling, numerical implementation, and the understanding of nonlinear phenomena with increasing complexities.

The issue has been predominantly addressed on clamped-clamped beams with initial curvature [76-79]. The nonlinear stretching is an intrinsic nonlinearity feature specific to a clamped-clamped beam due to constrained ends. Among several contributions, the classical von Karman model [80-83], with axial stain truncated to quadratic terms, was developed and applied to geometric nonlinearity analyses in a straight configuration [75, 84]. This analytical model combines the membrane and bending forces, in which the internal longitudinal force is generated by the end-constraint-induced tensile rigidity. In the proposed treatment, the axial inertia term is deemed negligible and therefore omitted [85, 86]. Such models lead to a resultant nonlinear force described by cubic terms which dominate the hardening effects on all vibration modes [87]. Considering an initial curvature, a modified von Karman model [88] was proposed through two separate equations: one on the transverse motion and another on longitudinal force inside a beam. Analyses show quadratic terms which cause the softening phenomenon of vibration modes [88, 89]. From a different perspective, by integrating all nonlinear terms into one equation, Nayfeh and Mook [75] and Lacarbonara *et al.* [90] developed an integral-differential condensation model with the consideration of nonlinear stretching. The work clearly illustrates that the initial curvature generates quadratic terms instead of cubic terms in the system equation. The ultimate hardening/softening is determined by the domination level of these competing terms. Meanwhile, Yi *et al.* [91] investigated the nonlinear dynamic

behaviors and modal interactions in the presence of elastic supports, in which hardening/softening can coexist. Qiao *et al.* [78] utilized a refined multi-scale method to simulate the hardening-softening transition with the consideration of the initial curvature. Analyses show that a near-transition region appears where the competing nonlinearities from hardening/softening balance each other. Meanwhile, Ghayesh *et al.* [92] exploited coupled stress tensor in a micro-beam structure, with results showing that the softening induced by the initial curvature can turn into hardening with increasing forcing level.

Different from end-constrained structures, i.e. clamped or pinned boundaries, a free boundary in a cantilever beam would cause the shortening effect [93], which creates intriguing problems. More specifically, the strain along the neural axis of the beam becomes zero and the coupling between the transverse and longitudinal motions of the beam is enhanced. Together with the initial curvature, significant nonlinear inertia effect is expected to surge to significantly impact on the nonlinear dynamic behaviors of the system. Note this inertia effect has traditionally been ignored in an end-constrained beam. Meanwhile, as to be illustrated later, the consideration of the inertia effect also creates additional difficulties in solving the system dynamic equations. Past attempts to address similar problems were only based on straight cantilever beams using geometrically exact beam models [93-98]. In particular, an inextensible condensation model on a straight cantilever beam [85, 93, 97, 99-102] shows cubic nonlinear terms arising from the nonlinear stiffness and nonlinear inertia, whose relative dominance levels ultimately determine the modal hardening or softening. In general, nonlinear inertia

effect is commonly considered to dominate high frequencies in a uniform beam, which is accountable for the modal softening [75], whilst nonlinear stiffness has noticeable effects on the first vibration mode through producing hardening effect, as verified both theoretically [93, 99-101] and experimentally [103-105]. More recently, Thomas *et al.* [100] extended the inextensible model to a rotating cantilever beam and discussed distinctions between von Karman's theory and the inextensible model. Considering the rotation-induced centrifugal force, a reduced order model was applied to investigate the hardening/softening phenomena. With increasing rotating speed, the rotary effect, coupled with the nonlinear stiffness and nonlinear inertia, results in a hardening-softening transition for the first mode, and an enhanced softening effect for higher-order modes. Meanwhile, Farokhi *et al.* [105] utilized a geometrically exact model to investigate the scenario of extremely large motion in cantilevers with experimental validations, and the reported results emphasized the deficiency of the well-known truncated inextensible model [93, 97] in this extreme case. Amabili *et al.* [106] considered shear effects and rotary inertia, which may become more important than nonlinear inertia in a thick cantilever beam.

1.3.3 Numerical methods

The aforementioned challenges are also accompanied by some specific needs and difficulties associated with the numerical implementation of the model, particularly in terms of discretization and numerical solver development. In fact, proper numerical treatments are

needed to cope with the large deformation and inertia-induced nonlinearity terms, which are distributed over the entire structure. On account of this, geometric nonlinearities, from a modal viewpoint, can be regarded as the result of nonlinear coupling of linear modes [85], which carry clear physical meaning in real life and commonly used as discrete basis in modal approach. The popular technique known as reduced-order model (ROM) [85, 100, 107] can then be applied to construct semi-discrete system equations to mimic/simulate nonlinear complexity in a full order model. Nonlinear frequency response (NFR) curves, backbones and nonlinear normal modes (NNMs) can be numerically solved by asymptotic numerical method (ANM) combined with harmonic balance (HB) method [85, 100, 105, 107, 108]. This approach, though widely used in geometric nonlinearity analysis with great success, suffers from two drawbacks. The first one is related to ROM, which usually requires a prohibitive number of linear modes to reach convergence, most of them having natural frequencies out of the frequency band of interest. The second issue relating to ANM is the need for recasting the nonlinear terms into quadratic order by introducing auxiliary variables and additional equations, in which the second order PDEs are transformed to the first order, for which a sufficiently large number of harmonics are required in harmonic balance procedure [109]. As to be demonstrated later in this thesis, both limitations are detrimental for the problem to be investigated in this thesis, since both the free end of the cantilever beam and its initial curvature would jeopardize the applicability of these techniques.

Although conventional HB continuation method (based on alternating frequency/time

procedure) [87, 110] can be directly applied to semi-discretized equations, no attempt has been made so far to cope with nonlinear inertia terms using this method, which is also one of the problems to be addressed in this work through the proposal of a dedicated numerical technique. The generalized- α method [111] (one of the time-integration methods), which is conventionally used to confirm the frequency domain results, is very time-consuming and such method is sensitive to geometric nonlinearities [100]. This problem also needs to be tackled, which is accomplished in the later part of this thesis by introducing an operator splitting (OS) method in the Newton iteration procedure.

1.3.4 ABH with nonlinearities

Due to the amplified vibration amplitude at the free end of an ABH cantilever, it is also natural to think about inducing geometric nonlinearities in the ABH structure to enable energy transfer, as studied in [112]. Fig 1.13 shows output acceleration for the ABH beam excited at 102 Hz, and the excitation force level increases with time. Less than 11 seconds, the frequency components above the excitation frequency are barely visible. Suddenly, all frequency components are excited from 11 seconds, indicating energy transfer from low to high frequencies.

Apart from intrinsic nonlinearity, intentional nonlinearity is considered as an alternative. Vibro-impact ABH (VI-ABH) was then investigated [113, 114]. This system was shown to

generate significant energy transfer from low to high frequencies, conducive to passive vibration control at low frequencies. A nonlinear energy sink (NES) was also integrated into the ABH structure to achieve targeted energy transfer (TET) [115-117]. In these systems, the

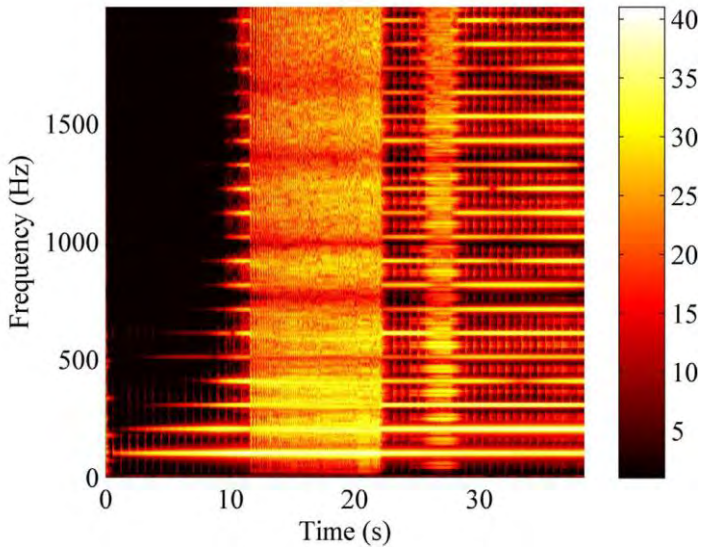

Fig 1.13 Spectrogram of output acceleration for the ABH beam excited at 102 Hz. The excitation force increases from 0 to 15 N in 40 s. [112]

energy of a base structure can be irreversibly transferred to the NES through nonlinear energy interactions [71] and then dissipated through NES damping. In addition, energy transfer was also achieved by electromechanical coupling with nonlinear capacitances in a resonant shunt which is connected to an ABH structure through piezoelectric materials [118], where a reduction in vibration amplitude was observed at low resonant frequencies.

1.4 Existing problems and research objectives

1.4.1 Existing problems

Previous efforts to explore various aspects related to ABH structures and nonlinearities have been presented in the literature review. Despite some progress in their respective fields, research on ABH structures with intrinsic and intentional nonlinearities is still in its early stage, and there are still unresolved issues at both the fundamental and engineering levels.

Although ABH has promising applications in vibration and noise reduction, the ABH effect remains in the high-frequency range. When the bending wavelength is comparable to or greater than the characteristic ABH length, ABH shows insufficient energy focusing and reduced damping. This shortcoming hinders its application in the low-frequency range. To counter this, an extraordinarily large structure is required to reduce the frequency limit. Nevertheless, due to the very thin thickness at the ABH tip, the amplified vibration amplitude results in noticeable geometric nonlinearities. Besides, manufacturing limitations produce imperfect geometry, such as initial curvature and a residual platform, which leads to more complex nonlinear dynamic behaviors. From a scientific viewpoint, the geometrically nonlinear features of ABH beams with geometric imperfections remain largely unknown. From a general purpose, this problem also poses challenges for initially curved cantilevers in system modeling, numerical techniques, and physical understanding, which should be addressed first.

Conventional methods aiming at improving low-frequency ABH effect present a challenge to existing manufacturing capabilities and affect the acceptance of the structures. Meanwhile, the energy transfer induced by nonlinearity can provide a feasible solution. The first attempt was to utilize geometric nonlinearities [112], whereas this implementation requires excessively long structures, which is considered as a limitation. Within a reasonable structural size, intentional nonlinearities can facilitate substantial energy transfer to enhance the ABH effect. However, the methods reviewed in Section 1.3.4, such as vibro-impact or electromechanical nonlinearities, either threaten structural safety or lack efficiency. Thus, this thesis presents an alternative solution by introducing grounded cables with cubic stiffness in an ABH beam, which, to the authors' knowledge, has not been attempted before in the context of ABH.

1.4.2 Research objectives

This thesis attempts to target the following objectives to solve these problems:

(1) To propose a geometrically exact inextensible condensation model on a curved cantilever beam with uniform thickness and to modify the HB continuation method and the generalized-α method in iteration procedure on account of inertia terms. To explore salient nonlinear dynamic features of the structure with particular emphasis on the effects of the nonlinear inertia enhanced by the curvature and the free boundary of the beam.

(2) To investigate the geometrically nonlinear features of the ABH beam with imperfect geometry. To conduct physical nonlinear experiments, and to confirm the simulation results with specific geometric parameters in both linear and nonlinear regimes.

(3) To propose the idea of using mechanical nonlinearity to enhance the low-frequency performance of ABH effects, exemplified by a ABH cantilever with coated damping layers and a grounded cubic stiffness cable, and to develop a simulation model accordingly. To carry out numerical simulations in the time and frequency domains to demonstrate the dynamic behaviors and the mechanism of energy transfer of the nonlinear ABH beam, which can be quantified via the damping loss factor of the system; and to conduct physical experiments to demonstrate the energy transfer phenomena and the enhanced ABH effect of the nonlinear damped ABH beam.

1.5 Overview of the thesis

The rest of the thesis is organized as follows.

Chapter 2 presents the theoretical formulation. A set of modified numerical methods is then proposed to cope with the numerical problems arising from the inertia effects. The established model is compared with a linear finite element (FE) model to validate the linear features of the model on the one hand and to assess the simplification assumptions being made in the

development of the nonlinear model so that its applicable range can be established on the other hand. Discussions on the stiffness and inertia terms induced by the initial curvature are then carried out. Numerical analyses are then conducted to elucidate the hardening/softening phenomena as well as the influence of the initial curvature.

In Chapter 3, an inextensional condensation model on an ABH beam with initial curvature is first described and applied to the present geometric nonlinear problems, which are then solved numerically by the harmonic balance (HB) method combined with a continuation approach. The numerical modeling and the experimental setup are summarized. Then, nonlinear results of a straight ABH beam with perfect geometry are presented, and the effects of imperfect geometry are investigated. Experiments are conducted to confirm the simulation results.

Chapter 4 presents a numerical model in which a grounded cubic stiffness cable and damping layers are integrated to a base ABH cantilever beam. The basic ABH-induced features under linear conditions are firstly illustrated using linear frequency response functions (FRFs), mode shapes, and damping loss factors. Then, linear and nonlinear cases are compared to demonstrate the effect of the nonlinearity in the low frequency range and energy transfer and dissipation process. Mechanical nonlinearity effects inside the damped ABH beam are quantified by an energy-based damping loss factor, and free decay tests verify these results in the time domain. Finally, the enhanced ABH effect resulting from the intentional nonlinearity

is experimentally demonstrated.

The major conclusions of this work are drawn and summarized in Chapter 5, with discussions and suggestions provided for possible future works

Chapter 2. Geometric Nonlinearities in a Curved Cantilever Beam

2.1 Introduction

Before embarking into an ABH structure, the general geometric nonlinear features of a curved cantilever will be investigated. Focus will be put on developing a general condensation model and exploring inertia-induced nonlinear features of the beam. The outcome of this investigation will be used in the subsequent ABH structural analyses.

The wide use of lightweight and flexible structures in engineering applications has aroused persistent interest in studying their intrinsic nonlinear behaviors. Among various types of basic structural elements, beam-like structures with initial curvature are of particular interest to the scientific community, exemplified by rotor blades [94], buckled beams [119], thin-walled composite beams [76], imperfect micro-beams [92] and shallow arches [77, 78] etc. Their highly flexible and thin-walled nature, especially for ABH structures, usually results in large amplitude vibration which gives rise to significant geometric nonlinearity and leads to rich and complex nonlinear dynamic behaviors which are absent in linear systems. Different from other types of nonlinearities such as mechanical or contact nonlinearity, geometric nonlinearity is distributed over the entire structure, which makes the problem more complicated. Whilst literature provides rather comprehensive knowledge on the source of intrinsic nonlinearities as well as the resultant dynamic behaviors such as hardening/softening phenomena [85], existing

condensation models are mostly associated with specific boundary condition [93, 120]. The so-called condensation model couples multi-dimensional internal forces or displacements to form one governing equation with explicit nonlinear terms. In addition, the introduction of initial curvature places higher demands on both physical modeling and simulation methods.

The condensed model for initially curved end-constrained structures is relatively well developed in terms of system modeling and numerical approaches [76-79]. As reviewed in Section 1.3.2, the nonlinear stretching force along the arc length enhances the hardening effect of the structure, while the initial curvature results in the softening effect. Typically, such imperfect structure with initial curvature exhibits softening even for the first mode [121]. However, the free boundary condition of cantilevers leads to the combined motions between the longitudinal and the transverse directions, thus introducing nonlinear stiffness and nonlinear inertia in cantilevers. Although considerable research has been done for straight free-clamped beams [85, 93, 97, 99, 101, 102], there is a significant gap in research on condensation modeling of initially curved cantilevers, which is extremely unfavorable for subsequent investigations on ABH beams with geometric imperfections. Furthermore, the inertia-induced nonlinear features bring challenges to numerical methods.

Therefore, in this chapter, an inextensible condensation model with initial curvature is proposed and used to examine initially curved uniform cantilever beams. The modified HB method is developed to solve inertia-induced problems and the operator splitting technique is

applied to time marching method with enhanced efficiency and robustness.

2.2 Inextensible condensation model with initial curvature

We consider a highly flexible and initially curved cantilever beam, which undergoes transverse flexural vibration coupled to the longitudinal motion along its length direction. Due to the free end, large deformation is induced which leads to non-negligible geometric nonlinearity and compelling nonlinear stiffness and inertia effects. The initial curvature of the beam would further enrich the nonlinear behaviors of the structure as well as the complexity in their analyses. After a brief recap on the geometrically exact model, a novel inextensible condensation model for a cantilever with initial curvature is developed in this section.

2.2.1 Recap on geometrically exact model

For the completeness of the paper, the geometrically exact model is briefly recalled hereafter. As shown in Fig 2.1, three coordinate systems are adapted to describe the geometric deformations of a curved beam segment. As the reference frame, Cartesian coordinate ab is used to define the local rotating coordinates xy and $\xi\eta$. Before the beam segment is deformed, the undeformed coordinate xy is fixed to the structure and rotates in the plane alongside the initial curve of the beam segment, whereas the deformed coordinate $\xi\eta$ specifies the segment motion with respect to xy. Their unit vectors are denoted, respectively, by $(\mathbf{i}_a, \mathbf{i}_b)$, $(\mathbf{i}_x, \mathbf{i}_y)$

and $(\mathbf{i}_1, \mathbf{i}_2)$ in the 2D plane. The location of an arbitrary point p on the beam is defined as $\mathbf{D}_p = A\mathbf{i}_a + B\mathbf{i}_b$ in the ab coordinate, and the point q is $\mathbf{D}_q = \mathbf{D}_p + \mathbf{D}'_p ds$ through infinitesimal distance ds, which gives

$$\mathbf{i}_x = \mathbf{D}'_p = A'\mathbf{i}_a + B'\mathbf{i}_b, \quad \mathbf{i}_y = -B'\mathbf{i}_a + A'\mathbf{i}_b, \tag{2.1}$$

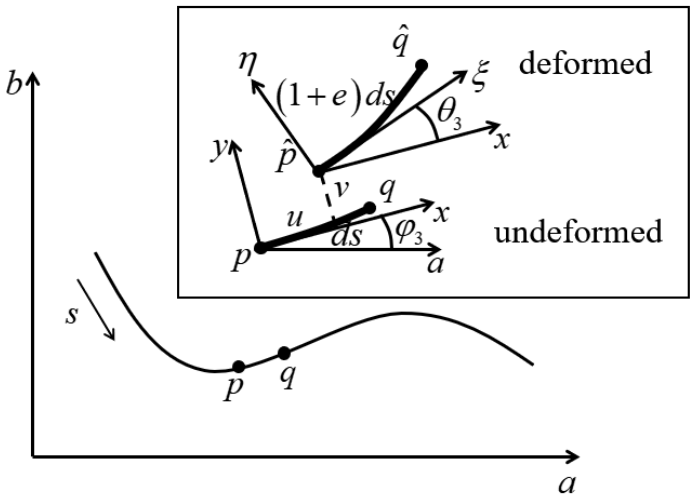

Fig 2.1 Definition of coordinate systems and relationship between the undeformed and deformed beam segments.

where $\cdot' = \partial \cdot / \partial s$ is the derivative with respect to the arclength s, and the module of $\mathbf{i}_x$ follows $A'^2 + B'^2 = 1$ whose first derivative follows $A'A'' + B'B'' = 0$. The rotation angle between the reference and the undeformed coordinates is φ_3 calculated by $\cos\varphi_3 = \mathbf{i}_x \cdot \mathbf{i}_a = A'$ and $\sin\varphi_3 = \mathbf{i}_x \cdot \mathbf{i}_b = B'$, of which the derivative with respect to s is the initial curvature k_3,

$$k_3 = \varphi'_3 = A'B'' - B'A''. \tag{2.2}$$

Combining Eq.(2.1), Eq.(2.2), and the above-mentioned relations of $\mathbf{i}_x$, the derivatives of

$(\mathbf{i}_x, \mathbf{i}_y)$ write

$$\mathbf{i}'_x = k_3 \mathbf{i}_y, \quad \mathbf{i}'_y = -k_3 \mathbf{i}_x . \tag{2.3}$$

Unlike the conventionally global description of displacements in the reference coordinate system, the co-rotational frame fastens deformed beam segment to the deformed coordinate without relative motion. The local displacement is therefore described by (u, v), which is the distance between $\xi\eta$ coordinate with xy coordinate. The end points p, q of the deformed segment are represented by $\mathbf{D}_p = \mathbf{D}_p + u\mathbf{i}_x + v\mathbf{i}_y$, $\mathbf{D}_q = \mathbf{D}_p + \mathbf{D}'_p ds$, based on which the unit vector $\mathbf{i}_1$ of the deformed coordinate is expressed by

$$\mathbf{i}_1 = \frac{\mathbf{D}'_{\hat{p}}}{(1+e)ds} = \frac{1+u'-vk_3}{1+e}\mathbf{i}_x + \frac{v'+uk_3}{1+e}\mathbf{i}_y , \tag{2.4}$$

where e is the axial strain along the undeformed neutral axis, and $\mathbf{i}_1$ is orthogonal to $\mathbf{i}_2$, i.e., $\mathbf{i}_1 \cdot \mathbf{i}_2 = 0$. Projecting $\mathbf{i}_1$ to xy axes and calculating its module, one obtains

$$\cos\theta_3 = \frac{1+u'-vk_3}{1+e}, \quad \sin\theta_3 = \frac{v'+uk_3}{1+e} , \tag{2.5}$$

$$e = \sqrt{(1+u'-vk_3)^2 + (v'+uk_3)^2} - 1 , \tag{2.6}$$

where θ_3 is the deformed angle between $\mathbf{i}_1$ and $\mathbf{i}_x$. Eq.(2.5) shows that the initial curvature affects the deformation of the beam through orthogonal components like vk_3, and then causes changes in the bending as well as the stretching properties different from a straight beam.

A flexible and thin structure would experience large deformation but small strain. In this case, it has been demonstrated that [100] engineering strains, consistent linearization of Green–Lagrange strains and Biot-Jaumann strains [94, 122] are identical in an Euler-Bernoulli beam. Consider a cantilever beam with a length L, a cross sectional area A, moment of inertia I,

made of homogeneous and isotropic elastic material of density ρ, Young's modulus E. For the bending-dominant oscillations, the normal strains ε_{11}, ε_{22} and shear strain ε_{12} on the cross section write

$$\begin{aligned} \varepsilon_{11} &= e - y\theta_3' \\ \varepsilon_{12} &= \varepsilon_{22} = 0 \end{aligned}, \tag{2.7}$$

which gives the normal stress $\sigma_{11} = E\varepsilon_{11}$. By integrating the normal stress over the cross section A, the longitudinal internal force F_1 and the bending moment M can be obtained as

$$\begin{aligned} F_1 &= \int_A \sigma_{11} dA = EAe \\ M &= -\int_A \sigma_{11} y dA = EI\theta_3' \end{aligned}, \tag{2.8}$$

which can lead to the transverse internal force $F_2 = -M'/(1+e)$ through moment balance equation by neglecting the rotating inertia [93]. Since the accelerations $\mathbf{a} = (u, v)$ is defined in xy coordinate, internal forces are projected to $(\mathbf{i}_x, \mathbf{i}_y)$ giving

$$\mathbf{F} = F_x \mathbf{i}_x + F_y \mathbf{i}_y = \left(F_1 \cos\theta_3 - F_2 \sin\theta_3\right)\mathbf{i}_x + \left(F_1 \sin\theta_3 + F_2 \cos\theta_3\right)\mathbf{i}_y . \tag{2.9}$$

Applying Newton's second law $d\mathbf{F} = mds\mathbf{a}$ to an infinitesimal segment ds of an initially curved beam, one has

$$\left(F_1 \cos\theta_3 - F_2 \sin\theta_3\right)' - k_3\left(F_1 \sin\theta_3 + F_2 \cos\theta_3\right) = m\ddot{u}, \tag{2.10}$$

$$\left(F_1 \sin\theta_3 + F_2 \cos\theta_3\right)' + k_3\left(F_1 \cos\theta_3 - F_2 \sin\theta_3\right) + f_{ext} = m\ddot{v}, \tag{2.11}$$

where $m = \rho A$ and f_{ext} is the external force applied to the transverse direction of the beam. Note that the above governing equations obtained by Newton's second law could also be derived from extended Hamilton principle [123] for Euler-Bernoulli beam vibrating in the xy plane. At the end of the curved cantilever beam fixed at $s = L$, boundary conditions write

$$\begin{aligned} u = v = \theta_3 = 0, \qquad & at\ s = L, \\ F_x = F_y = M = 0, \quad & at\ s = 0. \end{aligned} \tag{2.12}$$

2.2.2 Shortening effects and assumptions made for an inextensible condensation model

Compared with an end-constrained beam, a cantilever beam with a free boundary bears no axial strain along its central line, called neutral line, i.e., $e = 0$. The longitudinal displacement is coupled with the transverse displacement through Eq.(2.6) and expressed as

$$u' = \sqrt{1-\left(v' + uk_3\right)^2} - 1 + vk_3, \tag{2.13}$$

$$u = -\int_s^L \left(\sqrt{1-\left(v' + uk_3\right)^2} - 1 + vk_3\right) ds, \tag{2.14}$$

by using $u_L = 0$ at the constrained end $s = L$. Analytical solution of u is not available even though v is known. We herein assume that in the bending dominant oscillation, the transverse displacement v and its derivative v' have greater impact than uk_3 on calculation of the longitudinal displacement u in Eq.(2.14). Omitting uk_3 in the presence of v' with moderate initial curvature or local curvature (an assumption whose validity and the applicable range are to be assessed later), one has

$$u \approx -\int_s^L \left(\sqrt{1-v'^2} - 1 + vk_3\right) ds \approx \int_s^L \left(\frac{1}{2}v'^2 - vk_3\right) ds, \tag{2.15}$$

by keeping those terms up to quadratic order through Taylor expansion. Compared to a straight configuration, the longitudinal displacement u reaches the first order magnitude because of the initial curvature effect, which means that the coupled motion could be enhanced, either by the magnitude of k_3 or the curved length. Considering the force-free condition $F_x = 0$ at

$s=0$ and neglecting $F_1\sin\theta_3$ as a higher order term, the internal longitudinal force, from Eq.(2.10), can be obtained as

$$F_1=\frac{1}{\cos\theta_3}\left[\int_0^s\left(m\ddot{u}+F_2\cos\theta_3 k_3\right)ds+F_2\sin\theta_3\right]. \tag{2.16}$$

Eq.(2.16) shows the involvement of the nonlinear inertia in the beam vibration. Meanwhile, the initial curvature as well as the curved length affect both the nonlinear inertia and nonlinear stiffness. Substituting Eqs.(2.15) and (2.16) into Eq.(2.11), assuming a constant initial curvature k_3 and expanding all the terms up to the cubic order, one has the full set of condensed dynamic equation which governs the vibration of the cantilever expressed as

$$\begin{aligned}
&m\ddot{v}+c\dot{v}+\left(EIv''\right)''+k_3^2\left(EIv\right)''+k_3\left[k_3EI\left(v''+vk_3^2\right)\Big|_0^s\right]+k_3\int_0^s m\int_s^L\ddot{v}k_3dsds\\
&+\left\{\begin{array}{l}\dfrac{1}{2}\left\{\left[EIv'^2\left(v''+vk_3^2-k_3\right)\right]'+v'^2\left[EI\left(v''+vk_3^2\right)\right]'+2v'\left[k_3EI\left(v''+vk_3^2-\dfrac{1}{2}v'^2k_3\right)\Big|_0^s\right]\right\}'\\ +k_3\displaystyle\int_0^s EI\left(v''+vk_3^2\right)v'v''k_3ds-\frac{1}{2}k_3\left(k_3^2EIv'^2\Big|_0^s\right)\end{array}\right\}.\\
&-\left(v'\int_0^s m\int_s^L\left(\dot{v}'^2+v'\ddot{v}'-\ddot{v}k_3\right)dsds\right)'-k_3\int_0^s m\int_s^L\left(\dot{v}'^2+v'\ddot{v}'\right)dsds\\
&=f_{ext}
\end{aligned} \tag{2.17}$$

Note the above equation contains all linear and nonlinear effects in the system, which describes the full dynamics of the system in the most comprehensive and coupled manner. It is therefore the key equation to be further exploited in this paper. More specifically, the equation explicitly shows that stiffness, inertia, and initial curvature interact with each other both linearly and nonlinearly, giving rise to complex and rich dynamics (to be demonstrated later). More specifically, the first row (comprising the first four terms) presents the linear stiffness $k_3^2(EIv)''+k_3[k_3EI(v''+vk_3^2)\big|_0^s]$ and inertia $k_3\int_0^s m\int_s^L\ddot{v}k_3dsds$ induced by the initial curvature.

The second and the third rows account for the nonlinear stiffness and nonlinear inertia, respectively, cast into quadratic and cubic order terms. The most significant stiffness terms are connected to the local region of the structure, whereas the double integral of inertia terms takes into account the entire structure. It implies that inertia effect increases with the curved length due its increased portion participating in the vibration. Quadratic order terms appear in the curved cantilever beam, whose nonlinear features rise from the competing effects between the quadratic and cubic order nonlinear terms, which is similar to an end-constrained beam. However, nonlinear stiffness and inertia effects competing inside quadratic order terms are also responsible for the nonlinear dynamic responses.

2.3 Modified harmonic balance method and generalized-α method

This section proposes an efficient numerical approach, in frequency domain or time domain, respectively, to implement and solve the afore-established model with the consideration of the enhanced inertia effects. With Fourier series truncated to limited terms, HB method, combined with the continuation method, would allow for the calculation of the nonlinear frequency response by balancing the coefficients of the dominant harmonic orders. However, as discussed in Introduction, nonlinear inertia terms are usually handled in ANM by transforming the second order PDEs to the first order through introducing additional equations, which requires sophisticated mathematic treatment especially for systems with initial curvature. Besides, analytical mode shape functions are seldom available for complex structures, for

which we have to resort to FEM. Therefore, we hereafter combine the HB continuation method with FEM. This turns out to be possible since, thanks to the inextensible condensation model, the nonlinear inertia terms are explicitly expressed, which allows proper modifications on the Jacobian matrix, as to be detailed in section 2.3.1.

In a slightly different perspective, the generalized-α method is often used in nonlinear analyses. However, nonlinear systems usually require sufficiently small time steps, which becomes exorbitantly demanding in the present inertia-dominant system with initial curvature. Thomas *et al.* [100] opined that time evaluations should be carried out by using very small time steps and stepped-sine excitation to reach convergent results. This proved to be extremely time-consuming (typically 9 million time increment in a single curve) and sensitive to geometric nonlinearities. To achieve efficient simulation under the proposed modelling umbrella, we propose a splitting technique in the iteration stage of the Newton-Raphson method at each time step, to be detailed in section 2.3.2.2.

To discretize Eq.(2.17), the finite element method is followed by Galerkin procedure to build semi-discrete governing equation, with its element vector expressed as

$$\begin{aligned}&\int_0^{l_e}[N]^T\left[m\ddot{v}+c\dot{v}+\left(EIv''\right)''\right]ds_e\\&=\int_0^{l_e}[N]^T f_{ext}ds_e-\int_0^{l_e}[N]^T f_{int}\left(v,v',v'',\ddot{v},\dot{v}',\ddot{v}'',k_3\right)ds_e\end{aligned}, \tag{2.18}$$

where $[N]$ is the cubic shape function of Hermitian element containing four degrees of freedom (DOFs), l_e is the element length, superscript T is the vector transpose operator. The

continuous variable v in an element is approximated by $v = [N][d_e]$, in which $[d_e] = [v_0 \ v_0' \ v_1 \ v_1']^T$ is the element vector of the DOF. The global mass, damping as well as stiffness matrices are then constructed for left side terms of Eq.(2.18), with the clamped boundary conditions imposed [124]. All other portions including curvature-induced linear and nonlinear terms are gathered into a resultant force f_{int} vector, which allows for the treatment of piece-wise constant initial curvature for locally curved configuration.

2.3.1 Modified harmonic balance method

Based on Eq.(2.18), the corresponding general non-autonomous nonlinear dynamic system with N DOFs is cast into the following general form

$$\mathbf{M}\ddot{\mathbf{x}} + \mathbf{C}\dot{\mathbf{x}} + \mathbf{K}\mathbf{x} + \mathbf{f}_{int}\left(\mathbf{x}, \dot{\mathbf{x}}, \ddot{\mathbf{x}}\right) = \mathbf{f}_{ext}\left(\omega, t\right), \tag{2.19}$$

in which all internal force terms are regrouped in to $\mathbf{f}_{int}(\mathbf{x}, \mathbf{x}, \mathbf{x})$, $\mathbf{x}(t)$ and $\mathbf{f} = \mathbf{f}_{ext}\ \omega, t\ - \mathbf{f}_{int}(\mathbf{x}, \mathbf{x}, \mathbf{x})$ in Eq.(2.19) are approximated by Fourier series truncated to the N_H-th harmonic as

$$\mathbf{x}(t) = \frac{\mathbf{c}_0^x}{\sqrt{2}} + \sum_{k=1}^{N_H}\left(\mathbf{s}_k^x \sin(k\omega t) + \mathbf{c}_k^x \cos(k\omega t)\right), \tag{2.20}$$

$$\mathbf{f}(t) = \frac{\mathbf{c}_0^f}{\sqrt{2}} + \sum_{k=1}^{N_H}\left(\mathbf{s}_k^f \sin(k\omega t) + \mathbf{c}_k^f \cos(k\omega t)\right). \tag{2.21}$$

The coefficients are gathered into the $2N_H + 1$ $N \times 1$ vectors as

$$\mathbf{z} = \left[\left(\mathbf{c}_0^x\right)^T \quad \left(\mathbf{s}_1^x\right)^T \quad \left(\mathbf{c}_1^x\right)^T \quad \cdots \quad \left(\mathbf{s}_{N_H}^x\right)^T \quad \left(\mathbf{c}_{N_H}^x\right)^T\right]^T, \tag{2.22}$$

$$\mathbf{b} = \left[\left(\mathbf{c}_0^f\right)^T \quad \left(\mathbf{s}_1^f\right)^T \quad \left(\mathbf{c}_1^f\right)^T \quad \cdots \quad \left(\mathbf{s}_{N_H}^f\right)^T \quad \left(\mathbf{c}_{N_H}^f\right)^T\right]^T. \tag{2.23}$$

Substituting Eqs.(2.20)-(2.23) into Eq.(2.19) and following the standard Fourier-Galerkin balance procedure, a new target function $\mathbf{h}$ [110] depending on Fourier coefficients gives

$$\mathbf{h}(\mathbf{z},\omega)=\mathbf{A}(\omega)\mathbf{z}-\mathbf{b}(\mathbf{z})=\mathbf{0}, \tag{2.24}$$

with

$$\mathbf{A}=\nabla^2\otimes\mathbf{M}+\nabla\otimes\mathbf{C}+\mathbf{I}_{2N_H+1}\otimes\mathbf{K}, \tag{2.25}$$

where $\mathbf{A}$ is $2N_H+1\ N\times 2N_H+1\ N$ matrix for linear system; $\otimes$ stands for the Kronecker tensor product; ∇ and ∇^2 are gradient and Laplace operator matrices defined in [110]. The above equation is settled once the force coefficient vector $\mathbf{b}$ is provided. Through displacement-force relationship in time domain, alternating frequency/time method [125] and trigonometric collocation method are applied through Fast Fourier Transform (FFT) procedure, which gives

$$\mathbf{z}\xrightarrow{FFT^{-1}}\tilde{\mathbf{x}}=\mathbf{\Gamma}(\omega)\mathbf{z}\rightarrow\tilde{\mathbf{f}}\xrightarrow{FFT}\mathbf{b}(\mathbf{z})=\mathbf{\Gamma}^{+}(\omega)\tilde{\mathbf{f}}, \tag{2.26}$$

where $\mathbf{x}=[x_1(\mathbf{t})\cdots x_N(\mathbf{t})]$ and $\mathbf{f}=[f_1(\mathbf{t})\cdots f_N(\mathbf{t})]$ contain N_T time samples $\mathbf{t}=[t_1\cdots t_{N_T}]$ in each DOF, and the superscript + stands for the Moore–Penrose pseudoinverse. The linear operator matrix for inverse Fourier transform of displacement writes

$$\begin{aligned}\mathbf{\Gamma}(\omega)=\Big[&\mathbf{I}_N\otimes\left[0\cdot\tilde{\mathbf{t}}\right]^T\quad\mathbf{I}_N\otimes\left[\sin(\omega\tilde{\mathbf{t}})\right]^T\quad\mathbf{I}_N\otimes\left[\cos(\omega\tilde{\mathbf{t}})\right]^T\quad\cdots\\&\mathbf{I}_N\otimes\left[\sin(N_H\omega\tilde{\mathbf{t}})\right]^T\quad\mathbf{I}_N\otimes\left[\cos(N_H\omega\tilde{\mathbf{t}})\right]^T\Big]\end{aligned}, \tag{2.27}$$

and similar matrices for velocity and acceleration are

$$\begin{aligned}\dot{\mathbf{\Gamma}}(\omega)=\Big[&\mathbf{I}_N\otimes\left[0\cdot\tilde{\mathbf{t}}\right]^T\quad\mathbf{I}_N\otimes\omega\left[\cos(\omega\tilde{\mathbf{t}})\right]^T\quad\mathbf{I}_N\otimes\omega\left[-\sin(\omega\tilde{\mathbf{t}})\right]^T\cdots\\&\mathbf{I}_N\otimes N_H\omega\left[\cos(N_H\omega\tilde{\mathbf{t}})\right]^T\quad\mathbf{I}_N\otimes N_H\omega\left[-\sin(N_H\omega\tilde{\mathbf{t}})\right]^T\Big]\end{aligned}, \tag{2.28}$$

$$\ddot{\mathbf{\Gamma}}(\omega) = -\Big[\mathbf{I}_N \otimes \big[0 \cdot \tilde{\mathbf{t}}\big]^T \quad \mathbf{I}_N \otimes \omega^2 \big[\sin\big(\omega\tilde{\mathbf{t}}\big)\big]^T \quad \mathbf{I}_N \otimes \omega^2 \big[\cos\big(\omega\tilde{\mathbf{t}}\big)\big]^T \quad \cdots \\ \mathbf{I}_N \otimes \big(N_H\omega\big)^2 \big[\sin\big(N_H\omega\tilde{\mathbf{t}}\big)\big]^T \quad \mathbf{I}_N \otimes \big(N_H\omega\big)^2 \big[\cos\big(N_H\omega\tilde{\mathbf{t}}\big)\big]^T \Big] \,. \tag{2.29}$$

The Newton-Raphson method is utilized to reach the final solution iteratively through the calculation of the Jacobian matrix, which has impact on stability and accuracy of solution specific to inertia-induced feature. Using the chain rule, the Jacobian matrix of Eq.(2.24) with respect to $\mathbf{z}$ is written as

$$\begin{aligned} \frac{\partial \mathbf{h}}{\partial \mathbf{z}} &= \mathbf{A} - \frac{\partial \mathbf{b}}{\partial \mathbf{z}} \\ &= \mathbf{A} - \frac{\partial \mathbf{b}}{\partial \tilde{\mathbf{f}}} \frac{\partial \tilde{\mathbf{f}}}{\partial \mathbf{z}} \\ &= \mathbf{A} - \frac{\partial \mathbf{b}}{\partial \tilde{\mathbf{f}}} \left(\frac{\partial \tilde{\mathbf{f}}}{\partial \tilde{\mathbf{x}}} \frac{\partial \tilde{\mathbf{x}}}{\partial \mathbf{z}} + \frac{\partial \tilde{\mathbf{f}}}{\partial \dot{\tilde{\mathbf{x}}}} \frac{\partial \dot{\tilde{\mathbf{x}}}}{\partial \mathbf{z}} + \frac{\partial \tilde{\mathbf{f}}}{\partial \ddot{\tilde{\mathbf{x}}}} \frac{\partial \ddot{\tilde{\mathbf{x}}}}{\partial \mathbf{z}} \right), \\ &= \mathbf{A} - \mathbf{\Gamma}^+ \frac{\partial \tilde{\mathbf{f}}}{\partial \tilde{\mathbf{x}}} \mathbf{\Gamma} - \mathbf{\Gamma}^+ \frac{\partial \tilde{\mathbf{f}}}{\partial \dot{\tilde{\mathbf{x}}}} \dot{\mathbf{\Gamma}} - \mathbf{\Gamma}^+ \frac{\partial \tilde{\mathbf{f}}}{\partial \ddot{\tilde{\mathbf{x}}}} \ddot{\mathbf{\Gamma}} \end{aligned} \tag{2.30}$$

which includes independent variables related to resultant forces $\mathbf{f}(\mathbf{x}, \mathbf{x}, \mathbf{x})$, and inertia effects associated with entire DOFs. Since the stiffness terms are only connected to adjacent DOFs, the matrix $\partial \mathbf{f} / \partial \mathbf{x}$ is sparse and diagonally dominant, which usually has analytical formulation [87]. On the contrary, $\partial \mathbf{f} / \partial \mathbf{x}$ and $\partial \mathbf{f} / \partial \mathbf{x}$ are dense matrices because of the integral term in Eq.(2.17), and numerically approached by finite difference method. However, this approximation approach would slow down the convergence of iteration. To work out partial equations both efficiently and precisely, the eighth-order central difference scheme is adopted to calculate $\partial \mathbf{f} / \partial \mathbf{x}$, $\partial \mathbf{f} / \partial \mathbf{x}$ and $\partial \mathbf{f} / \partial \mathbf{x}$. The predicted solution is then corrected by Moore-Penrose continuation method. This is formulated as

$$\begin{aligned} \mathbf{y}_{(i,j+1)} &= \mathbf{y}_{(i,j)} - \mathbf{G}_{y,(i,j)}^{-1} \mathbf{G}_{(i,j)} \\ \mathbf{v}_{(i,j+1)} &= \mathbf{v}_{(i,j)} - \mathbf{G}_{y,(i,j)}^{-1} \mathbf{R}_{(i,j)} \end{aligned}, \tag{2.31}$$

with

$$\mathbf{G}=\begin{bmatrix}\mathbf{h}\\0\end{bmatrix},\quad \mathbf{J}=\begin{bmatrix}\mathbf{h}_z & \mathbf{h}_\omega\end{bmatrix},\quad \mathbf{G}_y=\begin{bmatrix}\mathbf{J}\\\mathbf{v}^T\end{bmatrix},\quad \mathbf{R}=\begin{bmatrix}\mathbf{Jv}\\0\end{bmatrix}, \tag{2.32}$$

by introducing optimization tangent vectors initialized as $\mathbf{v}_{(i,1)}=\mathbf{t}_i$, and $\mathbf{y}_{(i,j)}=\begin{bmatrix}\mathbf{z}_{i,j} & \omega_{i,j}\end{bmatrix}^T$.

2.3.2 Modified generalized-α method

2.3.2.1 The generalized-α method

Time-integration methods are often used in dynamic simulation of cantilevers [100, 101, 126], and additionally become a basic part of more sophisticated algorithms like nonlinear normal modes (NNMs) [127]. In the present case with the presence of initial curvature, the generalized-α method is utilized to calculate the time history to confirm the frequency domain results. Detailed derivations of this method are given as follows.

The generalized-α method is applied to offer intuitive time history of the system responses. In Section 2.3.1, Eq.(2.19) requires the treatment of different system response terms, especially displacement $\mathbf{x}$, as well as its derivatives representing velocity $\dot{\mathbf{x}}$ and acceleration $\ddot{\mathbf{x}}$. The interrelation among them can be cast into the following general form [111]:

$$\begin{aligned}\dot{\mathbf{x}}_{i+1}&=\dot{\mathbf{x}}_i+(1-\gamma)\Delta t\ddot{\mathbf{x}}_i+\gamma\Delta t\ddot{\mathbf{x}}_{i+1}\\ \mathbf{x}_{i+1}&=\mathbf{x}_i+\Delta t\dot{\mathbf{x}}_i+\Delta t^2\left(\frac{1}{2}-\beta\right)\ddot{\mathbf{x}}_i+\Delta t^2\beta\ddot{\mathbf{x}}_{i+1}\end{aligned}. \tag{2.33}$$

The governing equation of motion, Eq.(2.19), is built on semi-point scheme in the time discretization. The semi-point values of these quantities write

$$\begin{aligned}
\mathbf{x}_{i+1-\alpha_f} &= \left(1-\alpha_f\right)\mathbf{x}_{i+1} + \alpha_f \mathbf{x}_i \\
\dot{\mathbf{x}}_{i+1-\alpha_f} &= \left(1-\alpha_f\right)\dot{\mathbf{x}}_{i+1} + \alpha_f \dot{\mathbf{x}}_i \\
\ddot{\mathbf{x}}_{i+1-\alpha_m} &= \left(1-\alpha_m\right)\ddot{\mathbf{x}}_{i+1} + \alpha_m \ddot{\mathbf{x}}_i \\
t_{i+1-\alpha_f} &= \left(1-\alpha_f\right)t_{i+1} + \alpha_f t_i
\end{aligned} . \tag{2.34}$$

A residual vector is formulated from Eq.(2.19) as

$$\mathbf{r}\left(\mathbf{x}\right) = \mathbf{M}\ddot{\mathbf{x}} + \mathbf{C}\dot{\mathbf{x}} + \mathbf{K}\mathbf{x} + \mathbf{f}_{nl}\left(\mathbf{x},\dot{\mathbf{x}},\ddot{\mathbf{x}}\right) - \mathbf{f}_{ext} = \mathbf{0} . \tag{2.35}$$

Discretized version of the above equation in terms of $\left(\mathbf{x}_{i+1-\alpha_f}, \mathbf{x}_{i+1-\alpha_f}, \mathbf{x}_{i+1-\alpha_m}\right)$ writes

$$\mathbf{r}\left(\mathbf{x}_{i+1-\alpha_f}, \dot{\mathbf{x}}_{i+1-\alpha_f}, \ddot{\mathbf{x}}_{i+1-\alpha_m}\right) = \mathbf{0} . \tag{2.36}$$

Let us denote $\left(\mathbf{x}^k_{i+1-\alpha_f}, \mathbf{x}^k_{i+1-\alpha_f}, \mathbf{x}^k_{i+1-\alpha_m}\right)$ as the approximate value of $\left(\mathbf{x}_{i+1-\alpha_f},\ \mathbf{x}_{i+1-\alpha_f},\right.$ $\left.\mathbf{x}_{i+1-\alpha_m}\right)$ resulting from the iteration k. In the vicinity of the prediction value, the residual equation can be replaced with sufficient accuracy through the following linear expression:

$$\mathbf{r}^{k+1} \approx \mathbf{r}^k + \mathbf{S}^k \Delta\mathbf{x}^k_{i+1-\alpha_f} = \mathbf{r}^k + \mathbf{S}^k_T \Delta\mathbf{x}^k_{i+1} = \mathbf{0} , \tag{2.37}$$

in which the Jacobian (also called iteration) matrix writes:

$$\mathbf{S}^k_T = \left(1-\alpha_f\right)\left.\frac{\partial \mathbf{r}}{\partial \mathbf{x}}\right|_{\mathbf{x}^k_{i+1-\alpha_f}} , \tag{2.38}$$

whose expression is detailed as

$$\mathbf{S}_T\left(\mathbf{x}\right) = \left(1-\alpha_f\right)\left(\mathbf{M}\frac{\partial \ddot{\mathbf{x}}}{\partial \mathbf{x}} + \mathbf{C}\frac{\partial \dot{\mathbf{x}}}{\partial \mathbf{x}} + \mathbf{K} + \frac{\partial \mathbf{f}_{nl}}{\partial \mathbf{x}} + \frac{\partial \mathbf{f}_{nl}}{\partial \dot{\mathbf{x}}}\frac{\partial \dot{\mathbf{x}}}{\partial \mathbf{x}} + \frac{\partial \mathbf{f}_{nl}}{\partial \ddot{\mathbf{x}}}\frac{\partial \ddot{\mathbf{x}}}{\partial \mathbf{x}}\right). \tag{2.39}$$

The integration relationship, Eq.(2.33), can be written as

$$\begin{aligned}\frac{\partial \ddot{\mathbf{x}}_{i+1-\alpha_m}}{\partial \mathbf{x}_{i+1-\alpha_f}} &= \frac{1-\alpha_m}{\left(1-\alpha_f\right)\beta\Delta t^2}\mathbf{I} \\ \frac{\partial \dot{\mathbf{x}}_{i+1-\alpha_f}}{\partial \mathbf{x}_{i+1-\alpha_f}} &= \frac{\gamma}{\beta\Delta t}\mathbf{I}\end{aligned} . \tag{2.40}$$

Combining Eqs.(2.39) and (2.40) yields the expression of the iteration matrix as:

$$\begin{aligned}\mathbf{S}_T\left(\mathbf{x}\right) = &\frac{1-\alpha_m}{\beta\Delta t^2}\mathbf{M} + \frac{\gamma\left(1-\alpha_f\right)}{\beta\Delta t}\mathbf{C} + \left(1-\alpha_f\right)\mathbf{K} \\ &+ \left(1-\alpha_f\right)\frac{\partial \mathbf{f}_{nl}}{\partial \mathbf{x}} + \frac{\gamma\left(1-\alpha_f\right)}{\beta\Delta t}\frac{\partial \mathbf{f}_{nl}}{\partial \dot{\mathbf{x}}} + \frac{1-\alpha_m}{\beta\Delta t^2}\frac{\partial \mathbf{f}_{nl}}{\partial \ddot{\mathbf{x}}}\end{aligned} . \tag{2.41}$$

The nonlinear equation (2.37) is then solved using an iteration scheme using Newton-Raphson method. Substituting Eq.(2.33) and Eq.(2.34) into Eq.(2.37) gives

$$\mathbf{S}_T^k \Delta \mathbf{x}_{i+1}^k = -\mathbf{r}^k , \tag{2.42}$$

with

$$\begin{aligned}&\mathbf{r}^k = \beta\Delta t^2 \mathbf{S}_L \ddot{\mathbf{x}}_{i+1}^k + \mathbf{f}_{nl,i+1}^k - \mathbf{p}_{i+1} \\ &\mathbf{S}_L = \frac{1-\alpha_m}{\beta\Delta t^2}\mathbf{M} + \frac{\gamma\left(1-\alpha_f\right)}{\beta\Delta t}\mathbf{C} + \left(1-\alpha_f\right)\mathbf{K} \\ &\mathbf{p}_{i+1} = \left(1-\alpha_f\right)\mathbf{f}_{ext,i+1} + \alpha_f \mathbf{f}_{ext,i} - \left(\mathbf{a}_1\mathbf{x}_i + \mathbf{a}_2\dot{\mathbf{x}}_i + \mathbf{a}_3\ddot{\mathbf{x}}_i\right) \\ &\mathbf{a}_1 = \mathbf{K} \\ &\mathbf{a}_2 = \mathbf{C} + \left(1-\alpha_f\right)\Delta t\mathbf{K} \\ &\mathbf{a}_3 = \alpha_m\mathbf{M} + \left(1-\alpha_f\right)\left(1-\gamma\right)\Delta t\mathbf{C} + \Delta t^2\left(1-\alpha_f\right)\left(\frac{1}{2}-\beta\right)\mathbf{K}\end{aligned} . \tag{2.43}$$

The velocity and acceleration are found from

$$\begin{aligned}\Delta \ddot{\mathbf{x}}_{i+1}^k &= \frac{1}{\beta\Delta t^2}\Delta \mathbf{x}_{i+1}^k \\ \Delta \dot{\mathbf{x}}_{i+1}^k &= \frac{\gamma}{\beta\Delta t}\Delta \mathbf{x}_{i+1}^k\end{aligned} . \tag{2.44}$$

When $k = 0$, the initial prediction to initialize the process is $\mathbf{x}_{i+1}^0 = \mathbf{x}_i$ as the first order approximation, which would need more correction steps.

To simplify the process and reduce the computation burden, an alternative prediction formulation with third-order precision, i.e., $\mathbf{x}_{i+1}^{0} = 4\mathbf{x}_i - 6\mathbf{x}_{i-1} + 4\mathbf{x}_{i-2} - \mathbf{x}_{i-3}$, is proposed by using the four latest points. Stepwise correction continues until $\| \mathbf{r}\ \mathbf{x}_{i+1}^{k} \| \leq \varepsilon$, where ε is a predefined tolerance value.

The above calculation scheme is combined with the generalized-α method [111]. The parameters are chosen as follows

$$\begin{aligned} &\alpha_m = \frac{2\rho_\infty - 1}{\rho_\infty + 1}, \quad \alpha_f = \frac{\rho_\infty}{\rho_\infty + 1}, \quad \rho_\infty \in [0,1] \\ &\gamma = \frac{1}{2} - \alpha_m + \alpha_f, \quad \beta = \frac{1}{4}\left(1 - \alpha_m + \alpha_f\right)^2 \end{aligned} . \tag{2.45}$$

The dissipation parameter ρ_∞ is set to 0.8 for nonlinear problems with intentional nonlinearity.

2.3.2.2 Operator splitting (OS) technique for the generalized-α method

At each time step, the residual function is calculated as shown in Eq.(2.42), and approaches to zero in an iterative manner until converged results are reached. However, it is found that the numerical calculation is not stable due to the singularity of Jacobian matrix, which is triggered and amplified by the substantial inertia effects in the beam configuration under investigation here. To tackle the problem of avoiding singular iteration matrix, an OS technique is proposed here. The rationale behind is taking apart a complex function into several simple ones which are stable and easy to solve. The sequential splitting idea is herein proposed and presented as follows.

For $k+1$-th iteration at the time step $i+1$, the residual vector is expressed as

$$\mathbf{r}_{i+1}^{k+1} \approx \mathbf{r}_{i+1}^{k} + \left[\mathbf{S}_L + \left(1-\alpha_f\right)\frac{\partial \mathbf{f}_{nl}^{k}}{\partial \mathbf{x}} + \frac{\gamma\left(1-\alpha_f\right)}{\beta\Delta t}\frac{\partial \mathbf{f}_{nl}^{k}}{\partial \dot{\mathbf{x}}} + \frac{1-\alpha_m}{\beta\Delta t^2}\frac{\partial \mathbf{f}_{nl}^{k}}{\partial \ddot{\mathbf{x}}} \right]\Delta \mathbf{x}_{i+1}^{k} = \mathbf{0}\,. \tag{2.46}$$

Taking apart the nonlinear Jacobian matrix and dividing the iteration into 3 steps, by considering the first step $k+1/3$, the residual vector writes

$$\mathbf{r}_{i+1}^{k+\frac{1}{3}} \approx \mathbf{r}_{i+1}^{k} + \left[\mathbf{S}_L + \left(1-\alpha_f\right)\frac{\partial \mathbf{f}_{nl}^{k}}{\partial \mathbf{x}} \right]\Delta \mathbf{x}_{i+1}^{k} = \mathbf{0}\,, \tag{2.47}$$

to obtain the updated value $x_{i+1}^{k+1/3}$ before calculating the second step $k+2/3$,

$$\mathbf{r}_{i+1}^{k+\frac{2}{3}} \approx \mathbf{r}_{i+1}^{k+\frac{1}{3}} + \left[\mathbf{S}_L + \frac{\gamma\left(1-\alpha_f\right)}{\beta\Delta t}\frac{\partial \mathbf{f}_{nl}^{k+\frac{1}{3}}}{\partial \dot{\mathbf{x}}} \right]\Delta \mathbf{x}_{i+1}^{k+\frac{1}{3}} = \mathbf{0}\,. \tag{2.48}$$

By following the same procedure, the final stage $k+1$ is

$$\mathbf{r}_{i+1}^{k+1} \approx \mathbf{r}_{i+1}^{k+\frac{2}{3}} + \left[\mathbf{S}_L + \frac{1-\alpha_m}{\beta\Delta t^2}\frac{\partial \mathbf{f}_{nl}^{k+\frac{2}{3}}}{\partial \ddot{\mathbf{x}}} \right]\Delta \mathbf{x}_{i+1}^{k+\frac{2}{3}} = \mathbf{0}\,. \tag{2.49}$$

If $\| \mathbf{r}\ \mathbf{x}_{i+1}^{k}\ \| \leq \varepsilon(\varepsilon = 10^{-6})$, converged results are reached, and one can proceed to the next time step. Overall, this method divides the original expression into three different nonlinear sub-problems, each involving their respective nonlinear Jacobian matrices, and the sub-problem is accordingly solved in sequence. As such, while the Jacobian matrix involving nonlinear stiffness terms being generally diagonally dominant, the ill-condition problem of Jacobian matrix due to nonlinear inertia terms with increasing geometric nonlinearities is avoided and emerged in the numerical solver. As a result, the splitting procedure improves the accuracy, efficiency and the robustness of the generalized-α method, as demonstrated in the

following.

2.3.2.3 Efficiency and robustness enhanced by OS technique

The OS technique discussed in Section 2.3.2.2 is expected to improve the efficiency and the robustness of the generalized-α method by separating a full complex problem into several sub-problems. To demonstrate this, the generalized-α methods with and without the OS technique are compared using a beam vibration problem.

Examine the straight cantilever beam (used in Section 2.4) excited by a harmonic force at its free end. The excitation force has an amplitude 0.5 N at 3.85 Hz, which is arbitrarily chosen around the first natural frequency of the beam. The computation duration is 70 s, which is long enough to get stable response in the system. The sampling frequency is $f_s = 400$ Hz. Fig 2.2 (a) illustrates the overall time response signals obtained by using the two methods. The two curves coincide completely during the entire time duration, as better shown in the close-up view (Fig 2.2(b)). The residual values (as defined by Eq.(2.43) in Section 2.3.2.1) are calculated for both methods and shown in Fig 2.3(a). It follows that OS technique yields very small residuals, which are smaller than the ones without OS for nearly every single time point, demonstrating the accuracy of the proposed OS technique. Fig 2.3(b) shows the minimum iteration number required to achieve converged result with a residual value capped at 10^{-6}. It can be seen that, by embedding the OS technique into the generalized-α method, it takes only

one iteration to reach converged result, whilst more iterations are required without OS technique. This happens even within the stable region. Moreover, it was also noticed that generalized-α method without OS technique may not always yield converged solution for some frequencies, whilst the one with OS technique always does. The above comparison shows the high efficiency and the robustness of the generalized-α method after embedding the proposed OS technique.

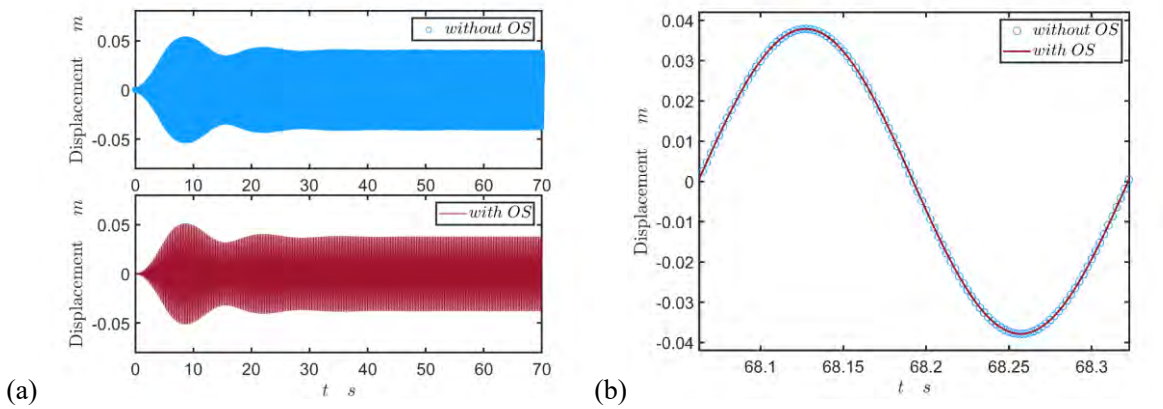

Fig 2.2 (a) Time responses obtained by the generalized-α method with and without OS technique, (b) close-up view taken in the stable region for a period. Note the two curves coincide perfectly so it is difficult to visually differentiate them.

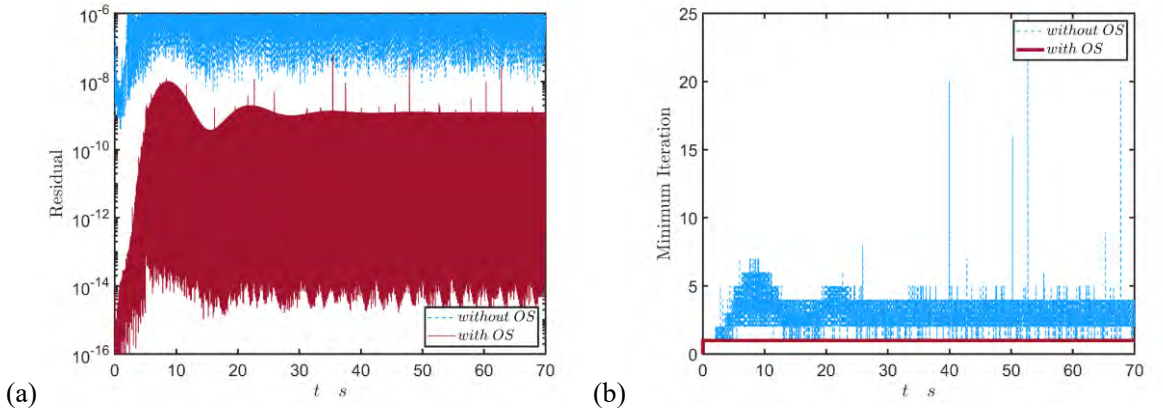

Fig 2.3 (a) Residual and (b) minimum iteration in each time point obtained by the generalized-α method with

and without OS technique. Note in Fig 2.3 (b), the method using OS needs only one iteration to reach the convergence.

2.4 Numerical results and analyses

2.4.1 Curvature-induced inertia/stiffness effects in linear models

This section focuses on the verification of the proposed model through examining the frequency responses and mode shapes of cantilevers in linear cases, to be used as a benchmark for the subsequent nonlinear analyses. Consistent with the reference solutions [100] provided for in a straight beam configuration, the same geometric and material parameters are used: length $L = 1000$ mm, rectangular cross section with a thickness $h = 5$ mm and width $b = 100$ mm, Young's modulus $E = 104$ GPa and density $\rho = 4400\ \mathrm{kg/m^3}$. When the beam is initially bended to form an initial curvature, two additional parameters are used for geometry description of the curved part: level of the initial curvature k_3 as defined in Eq.(2.2) and the curved arc length l_c starting from the free end tip of the beam.

From slightly to largely curved configurations, four cases are first examined as shown in Fig 2.4: i $k_3 = 0.5\pi, l_c/L = 0.1$; ii $k_3 = 0.5\pi, l_c/L = 0.5$; iii $k_3 = 0.5\pi, l_c/L = 1$; iv $k_3 = \pi, l_c/L = 1$. These configurations are also used to clarify the application range of the approximation used during the development of the condensation model in Eq.(2.15). A free boundary is imposed at $s = 0$ and the other extreme end of the beam is clamped at $s = L$. A

concentrated harmonic excitation force with an amplitude F_0 is transversely applied at the free end tip of the beam. Totally 20 uniform elements along the beam are utilized in the proposed model for analyses, and 24 Euler-Bernoulli beam elements are used in the beam interface of COMSOL software to provide linear reference solutions with the consideration of the initial curvature effect. The numerical tolerance of FEM simulation is set to 10^{-6}. For linear cases, a damping matrix $\mathbf{C} = \eta\mathbf{K}/2\pi f_i$, proportional to the stiffness matrix with a structural damping coefficient η of 0.005, is introduced. Denoting the natural frequency of each mode by f_i, both methods give very consistent values for the first four natural frequencies of the straight cantilever beam, i.e., $f_1 = 3.927$ Hz, $f_2 = 24.644$ Hz, $f_3 = 68.907$ Hz and $f_4 = 135.03$ Hz.

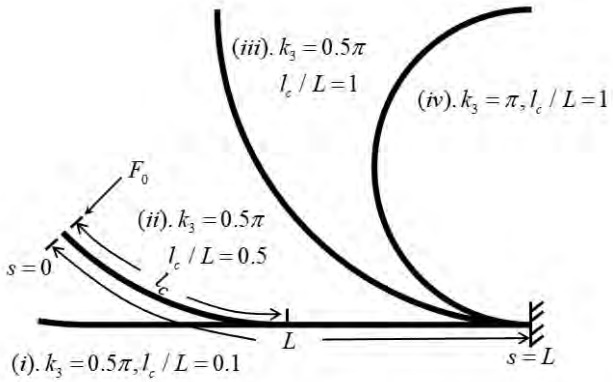

Fig 2.4 Definition of the curved configurations for cantilever beam.

2.4.1.1 Linear frequency response

Linear frequency responses are first calculated using different numerical strategies. The proposed model utilizes the HB method with $N_H = 1$ and Newton iteration $\mathbf{z}^* = \mathbf{z} - \mathbf{h}_z^{-1}\mathbf{h}$, where $\mathbf{z}^*$ is the accurate Fourier coefficient vector when results are converged. Calculated frequencies are equally spaced with $\Delta f = 2$ Hz to cover the range up to 500 Hz. The calculated point mobility of the beams is quantified in terms of $20\log_{10}(v/F_0)$ dB, where v is the transverse velocity defined in local xy coordinate. Fig 2.5 depicts the calculated mobilities of both the straight and curved beams with increasing initial deformation. For all four configurations, results show nice agreement between the results obtained from the proposed model and COMSOL (Fig 2.5(a)-(d)). Upon a very close examination, some barely noticeable differences, especially when the initial deformation becomes severe (e.g., Fig 2.5(d) for a demi-circle), exist but are all within an acceptable error range. This thus validates the linear part of the proposed model.

Cross figure comparisons between Fig 2.5(a)-(d), alongside the comparison with the straight beam, allow for the examination of the effects of the initial curvature and the curved arclength on the dynamics of the beams. It can be observed that the differences between the curved beams and the straight beam increase when the beam is more severely curved. By increasing the curved portion of the beam (through increasing either k_3 or l_c), natural frequencies gradually decrease for all modes. Taking the fourth natural frequency as an example, it drops by 2.03Hz, 6.53Hz and 19.03Hz from Fig 2.5 (b) to (d). Meanwhile,

resonance peaks also change with the frequency shift. It can be seen that, compared with the straight beam, the first resonance peak of the curved beam increases in Fig 2.5(b) but decreases again in Fig 2.5 (c)-(d), and the second to the fourth resonance peaks increase with increased curvature/arclength. All these can be attributed to the curvature, albeit still linear in the present stage, as a result of the coupled motion between the longitudinal and transverse displacements.

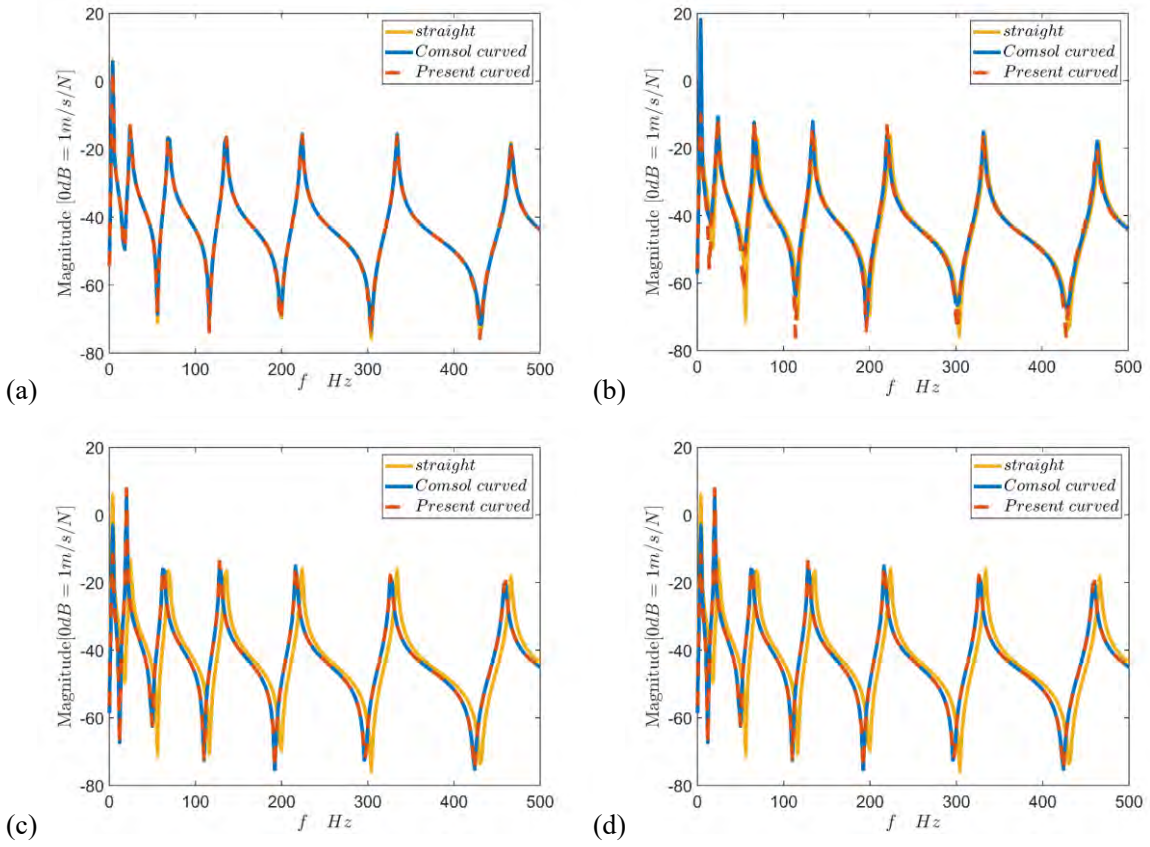

Fig 2.5 Linear FRFs at the free end tip. From (a) to (d): configuration (*i*)-(*iv*), respectively.

2.4.1.2 Linear mode shapes

To further substantiate the above and explain the underlying effects of the initial curvature, Fig 2.6 shows the normalized mode shapes of the first three modes in the four curved

configurations (*i*)-(*iv*) (as illustrated in Fig 2.4). First of all, comparisons of mode shapes show good agreement between the proposed model and COMSOL simulation in terms of modal deformation. Mode shapes, in terms of longitudinal displacement u, are shown in the left column of Fig 2.6. It can be observed that the initial curvature effect causes a larger portion of the beam to deform longitudinally, especially within the curved portion. The longitudinally deformed area expands for higher order modes as shown from Fig 2.6 (a) to (c). It can then be surmised that this phenomenon, coupled with transverse deformation of the beams, would in principle create enhanced inertia effects. Moreover, initial curvature also affects the transverse deformation, as illustrated by the right column in Fig 2.6, although variation patterns would be mode-specific. For example, the first mode (Fig 2.6(a)) shows that the largest displacement of configuration (*iv*) no longer occurs at the free end tip of the beam but moves closer to the middle when the initial deformation is large. The second and the third modes, however, show reduced deformation as compared to the tip when initial curvature increases.

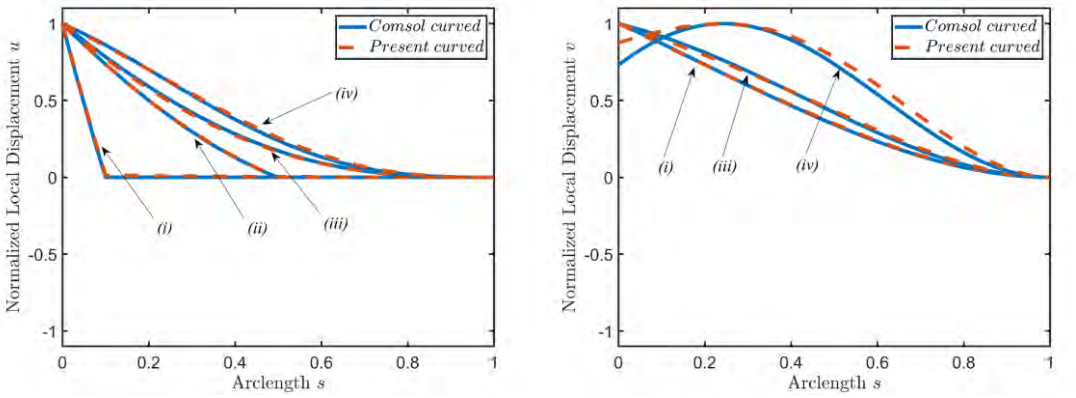

(a) Mode 1

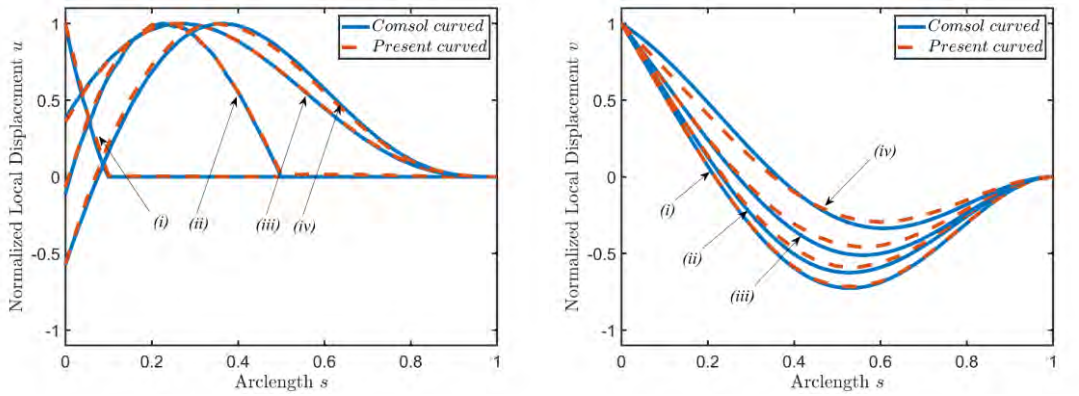

(b) Mode 2

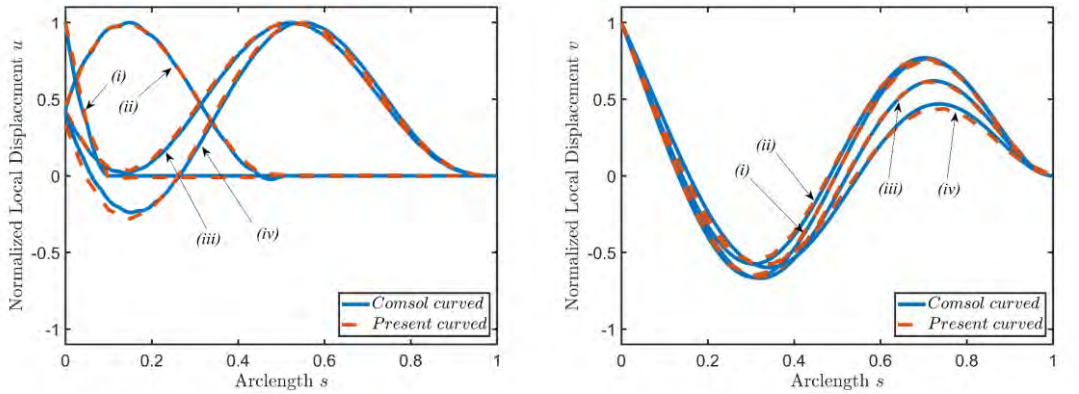

(c) Mode 3

Fig 2.6 Normalized mode shapes for curved cantilever beams. Left to right: u, v.

2.4.1.3 Examination of assumptions and effects of curvature-induced linear stiffness/inertia

In addition to the verification of the frequency responses and changes in the mode shapes, observations on the longitudinal deformation also testify the efficacy of the piece-wise treatment with constant initial curvature used in proposed model, thus expanding the application range to locally curved configuration. As mentioned above, an approximation is

used in Eq.(2.15) to facilitate the treatment of the longitudinal components so that the condensed model can finally be established. Therefore, it is important to revisit and assess this critical assumption which was used for approximation and at the same time check its validation range. To this end, we re-examine Eq.(2.13) by applying Taylor expansion and neglecting terms starting from $uk_3{}^2$. This process leads to the truncated expression of u' written as

$$u' = -\frac{1}{2}\left[2v'k_3 \cdot u + v'^2\right] + vk_3, \tag{2.50}$$

which is then cast into the standard first order non-homogeneous linear differential equation as

$$u' + v'k_3 \cdot u = -\frac{1}{2}v'^2 + vk_3. \tag{2.51}$$

The method of variation of constants [128] is then applied to solve Eq.(2.51) in which the following adjacent homogeneous equation needs to be solved first

$$u' + v'k_3 \cdot u = 0. \tag{2.52}$$

Integrating the above equation from s to L, the homogeneous solution u writes

$$\tilde{u} = Cu(L)e^{\int_s^L v'k_3 ds}, \tag{2.53}$$

where C is a constant. Then replacing the constant C with $C(s)$ and substituting u into Eq.(2.51), the unknown function $C(s)$ can be determined. Substituting $C(s)$ back into u, the final general solution, denoted by u_{full}, of the non-homogeneous equation writes

$$u_{full} = e^{\int_s^L v'k_3 ds}\int_s^L \left(\frac{1}{2}v'^2 - vk_3\right)e^{-\int_s^L v'k_3 ds} ds. \tag{2.54}$$

Note the above procedure allows for a more accurate estimation of the longitudinal displacement than the solution u obtained previously based on the approximation made in Eq.(2.15). To quantify the difference, a relative error factor over the entire beam span is defined as

$$P_1 = \left\| \frac{\int_0^L \|u\| ds - \int_0^L \|u_{full}\| ds}{\int_0^L \|u\| ds} \right\| \times 100\% . \tag{2.55}$$

To introduce noticeable nonlinear effects, the transverse displacement at the free end tip of the beam is set to $v_0 = 50 r_g$ for all modes, where r_g is the radius of gyration and defined by $r_g = h/\sqrt{12}$ with a rectangle cross section. In the present case, $v_0 = 0.072$ m. For even larger deformation used in the subsequent analyses, this issue will be commented again in due course. Using the linear mode shapes calculated above as an approximation, the calculated relative error P_1 for the first three modes in all four previous curved configurations is illustrated in Fig 2.7. It follows that, the slightly curved configuration (*i*) generates a very small error for all three modes, typically below 1%. As the beam is bent more severely, error increases. Nevertheless, even for the largest curved configuration (*iv*), the relative error is still capped below 8%, which is still acceptable. Therefore, the assumption used is deemed valid for all four configurations, even for the last one which is a severely curved semi-circle beam.

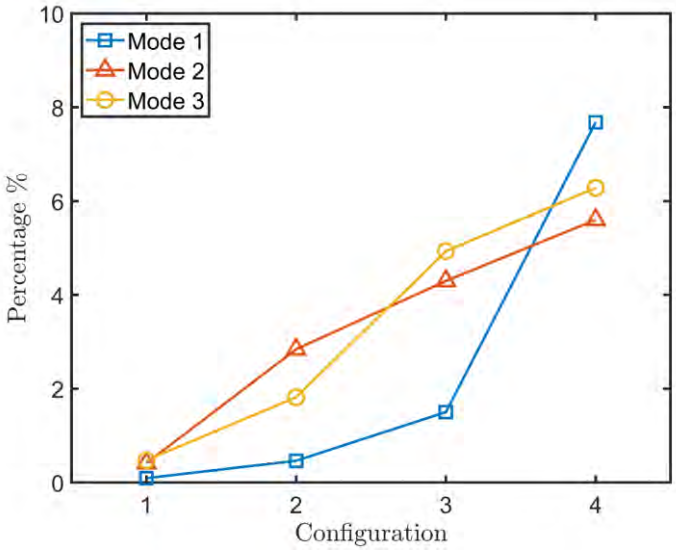

Fig 2.7 P_1 for different curved configurations.

As presented in the governing equation (Eq.(2.17)), the initial curvature affects the linear terms through a combined stiffness term and an inertia term, denoted by

$$k_{IC} = k_3^2 \left(EIv\right)'' + k_3 \left[k_3 EI \left(v'' + v k_3^2 \right) \Big|_0^s \right], \quad m_{IC} = k_3 \int_0^s m \int_s^L \ddot{v} k_3 ds ds \,. \tag{2.56}$$

Their respective impacts on the linear system response are demonstrated. To this end, k_{IC} and m_{IC} are separately considered for the extreme case of the curved configuration (*iv*). The calculated FRFs are depicted in Fig 2.8, which shows that both curvature-induced stiffness and inertia terms cause a reduction in the resonant frequencies, resulting in the ultimate differences between the straight and curved beams. A closer examination suggests that the peak shift caused by the curvature-induced stiffness and inertia is roughly the same starting from the third to higher-order modes, although differences are noticeable on the first two modes. More specifically, for the second mode, the inertia-induced effect affects more the second resonant frequency, while the stiffness-induced effect has a greater impact on the resonance peak level of the first mode.

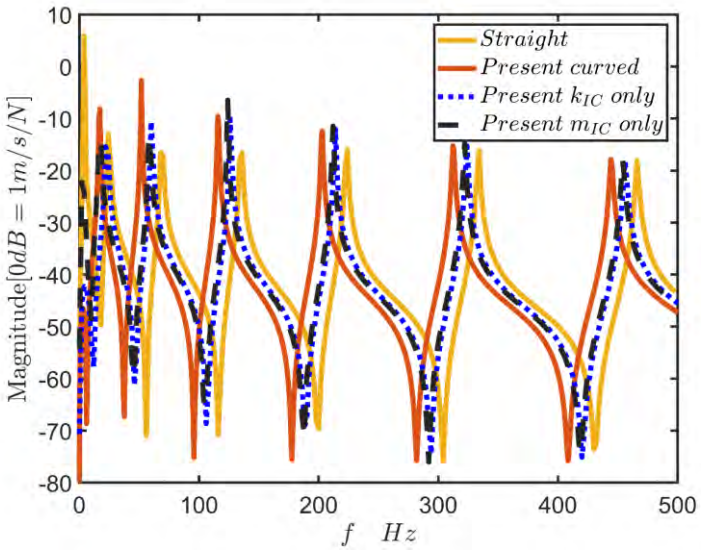

Fig 2.8 The initial curvature effect of linear stiffness and inertia.

2.4.2 Nonlinear dynamic features and curvature-induced inertia effect

This section focuses on the numerical simulations and analyses of nonlinear dynamic behaviors of initially curved cantilever beams. The HB continuation method established in Section 2.3.1 is utilized to provide frequency domain results, to be confirmed by the time history of the response signals. Truncated harmonics and time samples for all numerical simulations are set to $N_H = 5$ and $N_T = 64$, respectively. The generalized-α method should adopt a sufficiently high sampling frequency to slowly sweep in time domain, and the corresponding parameters are determined by the concerned frequency range. A damping matrix $\mathbf{C} = 2\eta\omega_0\mathbf{M}$, proportional to the mass matrix, is introduced, i.e., $\eta = 0.005$ herein. The amplitude of displacement in nonlinear frequency response (NFR) curves writes

$$\text{Displacement} = \frac{c_0^x}{\sqrt{2}} + 0.5\left(\max x\left(\tilde{\mathbf{t}}\right) - \min x\left(\tilde{\mathbf{t}}\right)\right), \tag{2.57}$$

which considers the rigid body motion $c_0^x/\sqrt{2}$, so that observations of asymmetry behaviors in frequency domain could coincide with the time history.

Numerical simulations on the curved beam in frequency domain are conducted and verified through comparisons with the time history of the system responses. With the initial curvature increasing from $k_3 = 0$ (straight beam) to $k_3 = 0.5\pi$ and a curved arclength of $l_c/L = 0.1$, corresponding NFR curves for the first mode are calculated and illustrated in Fig 2.9. In this case, the generalized-α method adopts a sampling frequency $f_s = 400$ Hz to sweep from 3.7 Hz to 4 Hz with a rate of 0.01 Hz/min. The horizontal axis denotes a dimensionless frequency, which is normalized by the first natural frequency of the corresponding straight beam $f_0 = 3.927$ Hz. Note that the straight beam simulations are firstly carried out using the proposed model, whose results have been compared to reference solutions [100]. At 1.5 N excitation level for the straight configuration, Fig 2.9(a) shows that NFR curves obtained by the proposed model agree well with the reference solution. Meanwhile, the observed NFR variation is also in good agreement with the time history responses obtained from frequency sweeping. More importantly, the hardening effect is obvious for the first mode, as a result of dominant level of the nonlinear stiffness effects. As the initial curvature increases in Fig 2.9(b)-(d), the resonance frequency gradually decreases while the hardening evolves to softening. Meanwhile, it can be observed that the resonance frequency peaks of the curved beams are all slightly lower than that of the straight beam (with the normalized frequency smaller than 1). From $k_3 = 0$ to $k_3 = 0.4\pi$, the time domain responses corresponding to the sweeping up process are

completely enveloped by the NFR curves, and the process is reversible. The situation is, however, different when the initial curvature increases to $k_3 = 0.5\pi$. In fact, Fig 2.9(d) shows that there exist two turning points on the NFR curve for the curved beam. The sweeping up curve jumps around the first turning point to the upper stable branch, while the sweeping down curve would jump around the second turning point so that hysteresis occurs.

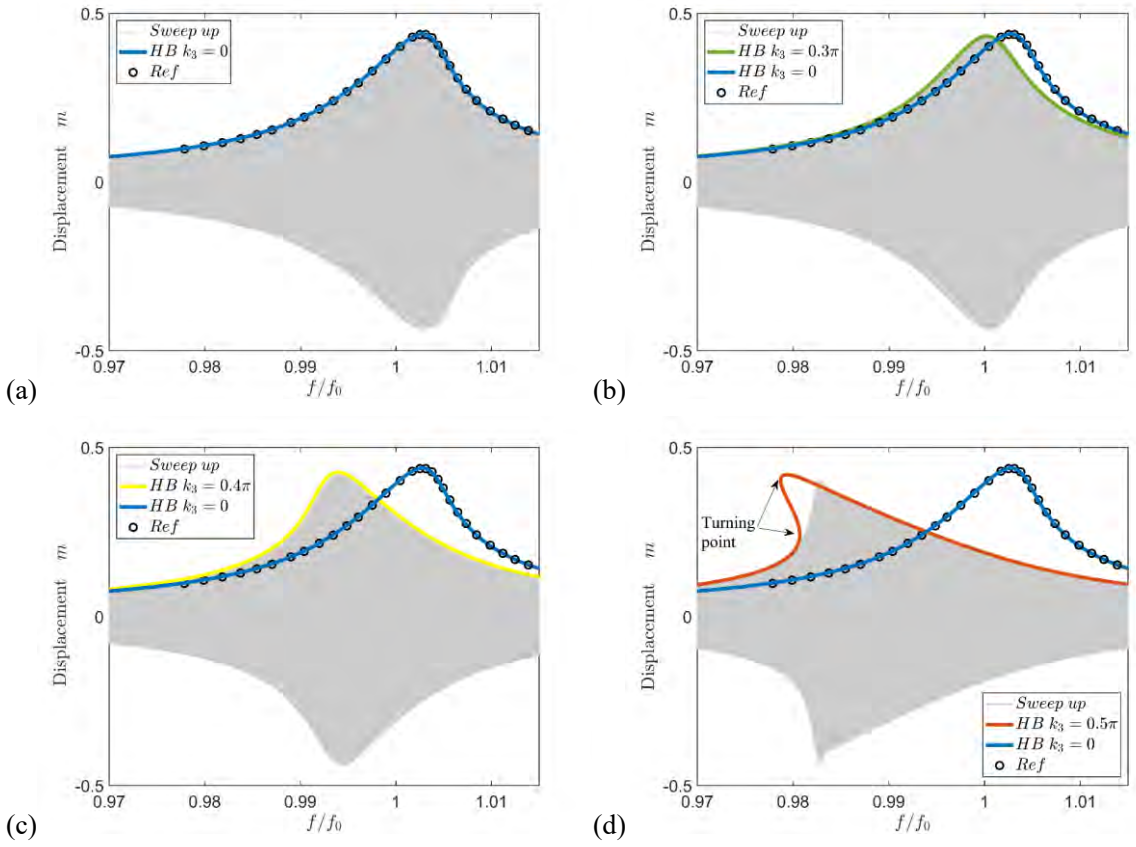

Fig 2.9 Comparisons of the HB method and the generalized-α method under 1.5 N force in the first mode for the curved beams with different initial curvature. (a) $k_3 = 0$, (b) $k_3 = 0.3\pi$, (c) $k_3 = 0.4\pi$, (d) $k_3 = 0.5\pi$. Circle: reference solution for the straight beam.

Additional numerical studies are conducted for different curved configurations and different forcing levels. Multiple harmonics, as a salient feature in nonlinear dynamic analysis,

would better inform on the complex nonlinear behaviors of the system through revealing the energy level of dominant harmonic orders. Therefore, the normalized harmonic coefficient for each order is calculated by

$$\sigma_i = \frac{\phi_i}{\sum_{k=1}^{N_H} \phi_i}, \quad (i = 0,1,2,\cdots,N_H), \tag{2.58}$$

with

$$\phi_0 = \frac{\left|c_0^x\right|}{\sqrt{2}}, \quad \phi_i = \sqrt{\left(s_i^x\right)^2 + \left(c_i^x\right)^2}, \quad (i = 1,2,\cdots,N_H).$$

which depends on the excitation frequency and is comprised between 0 and 1.

The same curved configurations as simulated in the above case are examined with the forcing level changing from 0.5 N to 2 N with a step size of $\Delta F = 0.5$ N. Fig 2.10(a) displays the NFR curves for the first mode. Comparing the straight configuration results from the HB method with ROM [100] shows nice agreement, even for the largest free-end displacement considered, which amounts to $0.6\ m$ (almost 2/3 of the beam length), with the first five harmonics considered in the current numerical method. For this large displacement, the error indicator P_1(as defined in Eq.(2.55)) for this curved configuration is only 0.869%, which is rather small to further confirm the validity of the assumption used in Eq.(2.15). It can be observed that resonance frequencies decrease with the increasing initial curvature (Fig 2.10(a)). Meanwhile a similar hardening-softening transition can be observed when the curvature reaches a certain level, as a result of the effective curvature-induced inertia effect. Obviously, a larger excitation level leads to a more significant frequency shift. There exists a specific initial

curvature value (between $k_3 = 0.3\pi$ and $k_3 = 0.4\pi$), at which the nonlinear system shows no frequency shift like its linear counterpart. Similar phenomenon, called near-transition, has also been observed in the literature although cases are different [78]. At this specific curvature, various competing nonlinear factors in the system balance each other.

The normalized harmonic coefficients are logarithmically shown in Fig 2.10(b)-(e). Consistent with the NFR curves in Fig 2.10(a), the appearance of multiple harmonics also confirms the occurrence of the hardening-softening transition. For the straight configuration, Fig 2.10(b) illustrates that the third harmonic coefficient is the largest followed by the fifth one. Note even-order harmonics, which should not exist theoretically, appear because of the computer calculation error, but they have a smaller magnitude than odd-order harmonics. When a small initial curvature is added, it changes system response and induces zero- and even-order harmonics as shown in Fig 2.10(c). The same pattern basically remains when further increasing the initial curvature, except a slight downshifting of the peak region to lower frequencies as shown in Fig 2.10(d). It can be observed that the dominant even-order harmonics account for the hardening-softening transition. As to the most severely curved beam (Fig 2.10(e)), a turning point phenomenon similar to that observed in Fig 2.10(d) is reflected back to each harmonic. The energy level of the harmonics generally reduces when harmonic order increases. Note that the zero-order harmonic is the largest among all harmonic coefficients in Fig 2.10(d)-(e), since all even-order terms contribute to the zero-order coefficient through the quadratic order terms in the governing equation.

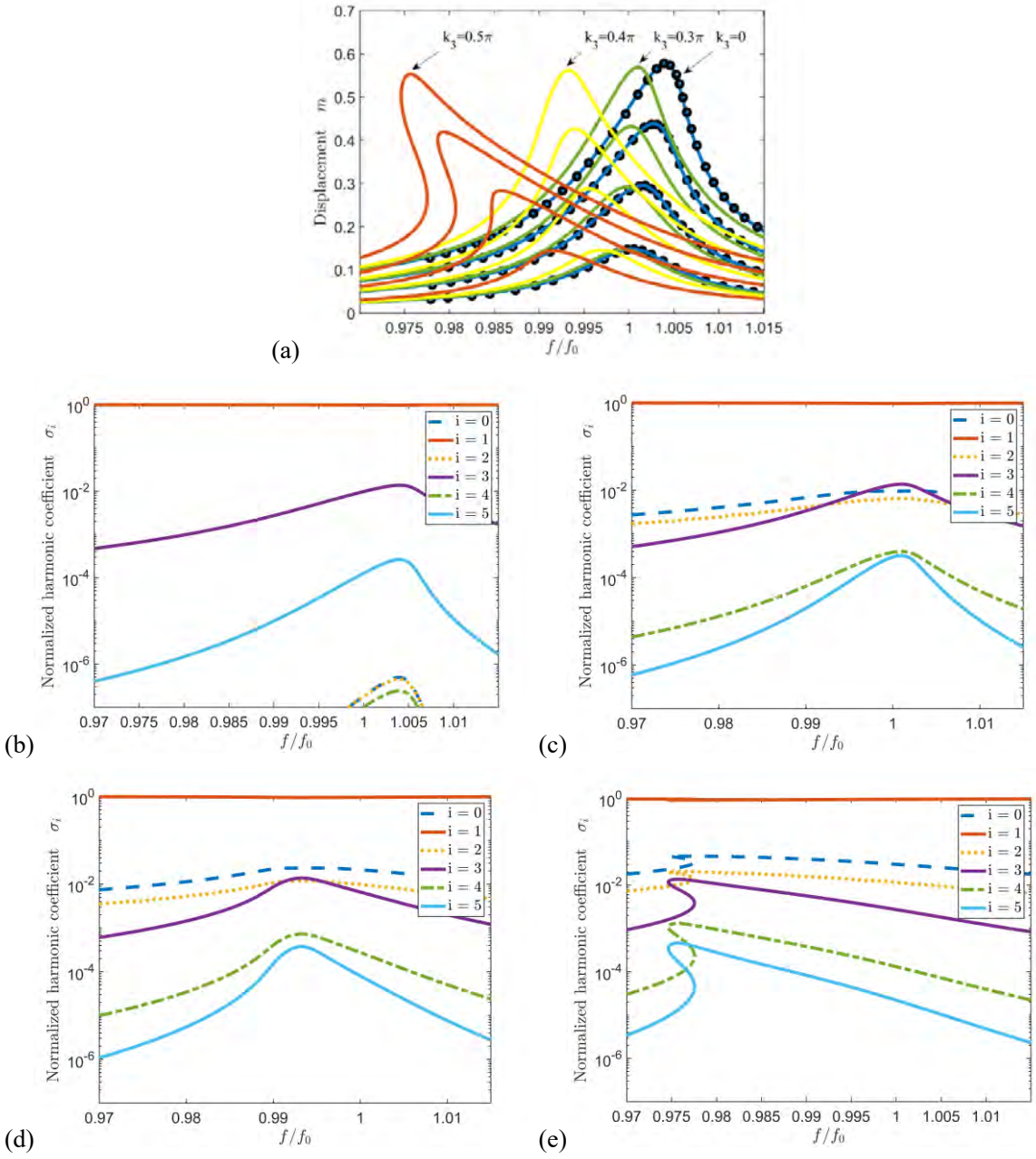

Fig 2.10 NFR curves of the first mode with the various initial curvature and excitation level, as well as normalized harmonic coefficients. (a) NFR curves when $F_0 = [0.5\ 1\ 1.5\ 2]$ N. Circle: reference solution. The first six harmonic coefficients at the forcing level of 2 N: (b) $k_3 = 0$, (c) $k_3 = 0.3\pi$, (d) $k_3 = 0.4\pi$, (e) $k_3 = 0.5\pi$.

Considering the dominant nonlinear inertia, the straight cantilever beam essentially

exhibits softening phenomenon in higher modes, which is different from the first mode [93]. Therefore, the curvature-induced effects on higher modes are demonstrated when the initial curvature is involved. To this end, the NFR curves of the second and third modes are depicted in Fig 2.11 for different initial curvatures and forcing levels. With 6 N and 12 N excitation applied to the second mode, straight configuration shows good agreement between the results obtained from the HB continuation method and ROM (Fig 2.11(a)-(b)). When the initial curvature is added, the resonance peaks of the curved beam shown in Fig 2.11(a) reduces with the increasing initial curvature. To quantify the changes, the relative displacement ratio between the curved configurations $k_3 = 0$ and $k_3 = 0.7\pi$ is calculated, yielding 16.2%. The ratio increases up to 27.6% at the higher forcing level of 12 N, as shown in Fig 2.11(b). Meanwhile, the curved beams in higher modes show slight frequency shift when the initial curvature increases. Nevertheless, because of the curvature-induced quadratic terms in the governing equations, higher modes show asymmetric responses, which can be observed through time responses for the case of $k_3 = 0.7\pi$, shown in the subplot of Fig 2.11(a). This phenomenon becomes more obvious when the forcing level increases, as shown through comparisons between the two figures (Fig 2.11(a) and (b)). Besides, with the largest initial curvature $k_3 = \pi$, Fig 2.11(a) shows a loop in the second mode, which is further enlarged and heads down when the excitation force increases to 12 N, as depicted in Fig 2.11(b). The occurrence of negative displacement represents asymmetric vibration, which can be explained by Eq.(2.57). Similar patterns remain for the third mode (Fig 2.11(c) and (d)). However, the third mode is more difficult to excite to trigger its inherent nonlinear behavior than the second

mode, unless a larger excitation force is applied.

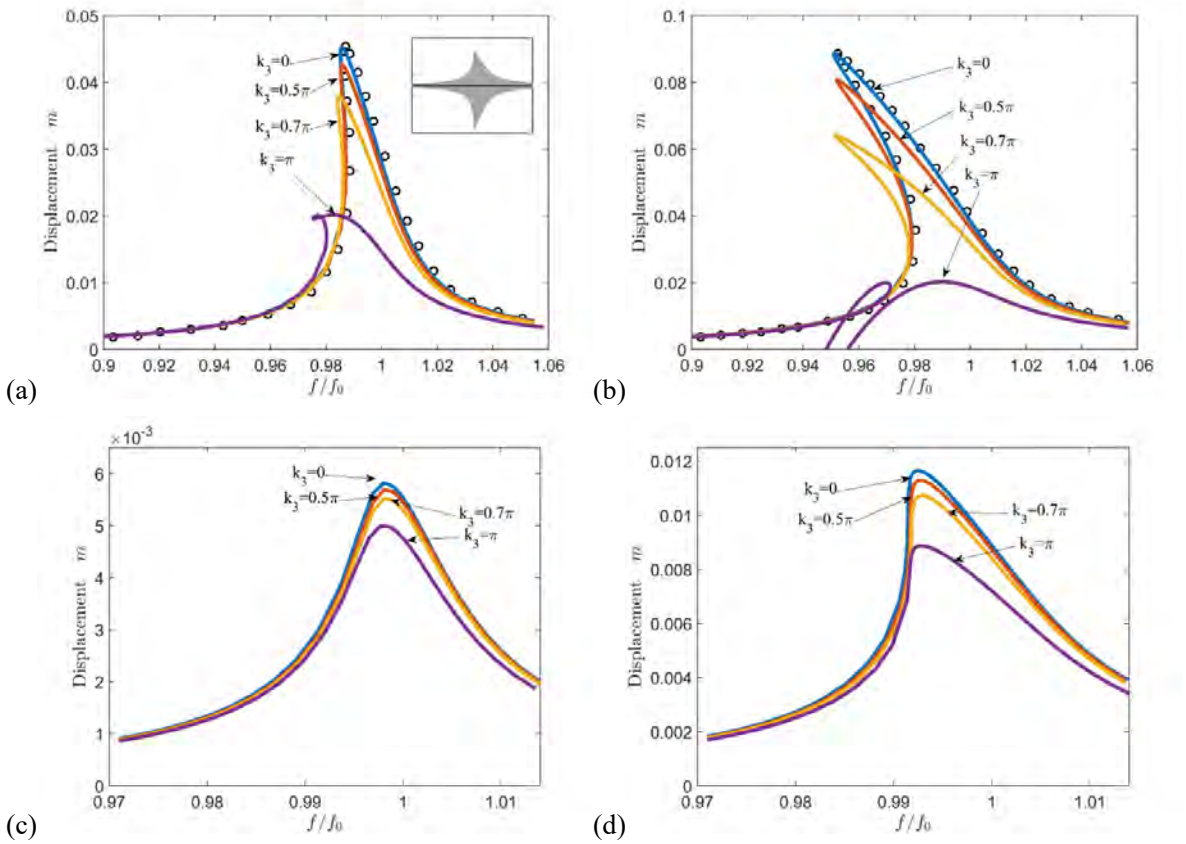

Fig 2.11 NFR curves of higher modes with various initial curvatures and forcing levels. (a)-(b): Mode 2 at the forcing level of 6 N and 12 N, respectively. (c)-(d): Mode 3 at the forcing level of 6 N and 12 N, respectively. Circle in (a)-(b): reference solution of the second mode for the straight beam.

The initial curved deformation of the beam also depends on curved arclength l_c. Therefore, a longer arclength $l_c/L = 0.2$ is investigated. At a moderate forcing level of 1.5 N and 2 N, NFR curves in Fig 2.12(a) shows a reduction of the resonance frequency of the first mode. In this regard, increasing l_c leads to the same effects as k_3 in terms of hardening-softening transition in the first mode. However, at an even higher forcing level, 3 N, the NFR curve becomes more complex. In fact, four turning points can be observed, alongside a reversed trend,

turning from softening to hardening. A plausible explanation can be offered. In a straight beam, the nonlinear stiffness dominates the first mode to produce the commonly-observed hardening phenomenon due to its large deformation. When the beam is initially curved, inertia effects are amplified and compete with the stiffness effects. However, for a sufficiently high forcing level, the larger deformation would enhance nonlinear stiffness effects to produce the ultimate softening-hardening behavior observed in Fig 2.12(a). Similar phenomenon is reflected in the normalized harmonic coefficients at the same forcing level of 3 N (Fig 2.12(b)). In addition, the zero-order and the second harmonics show more complex variation, as evidenced by the appearance of loop, shown in the inset plots. It is relevant to note that nonlinear dynamic behaviors of the curved beam are not only determined by the curved condition (curvature and arclength), but also the excitation level.

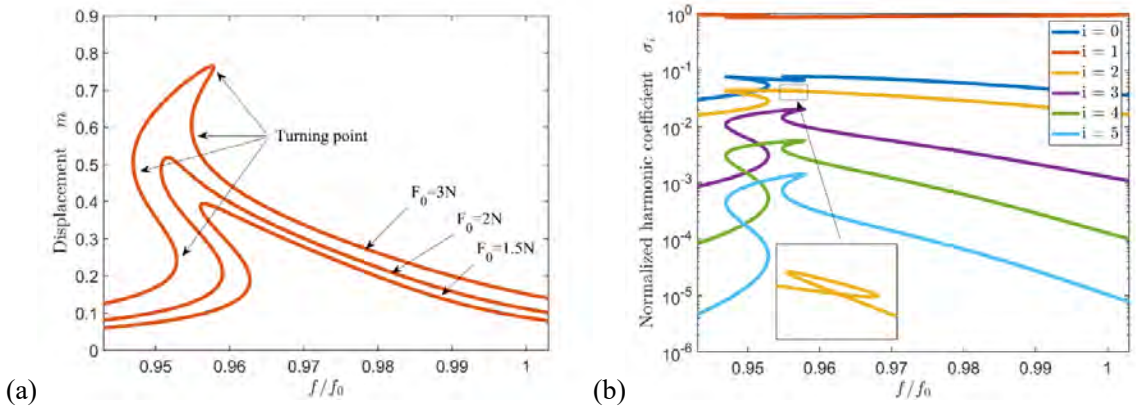

(a) (b)

Fig 2.12 (a) NFR curves for the first mode when $F_0 = [1.5\ 2\ 3]$ N. (b) Normalized harmonic coefficients at the forcing level of 3 N.

To further substantiate the above, effects of different arclengths in terms of harmonics are compared. Fig 2.13 shows that the overall level of the normalized zero- and even-order

harmonic coefficients increases with the curved arclength. However, variations of the odd-order coefficients are marginal and inconsistent in magnitude. For example, the third-order coefficient even decreases slightly. In general, an increase in the initial deformation of the beam would favor the generation of more energetic higher order harmonics, which at the same time generates increased energy transfer, mainly to the even-order components.

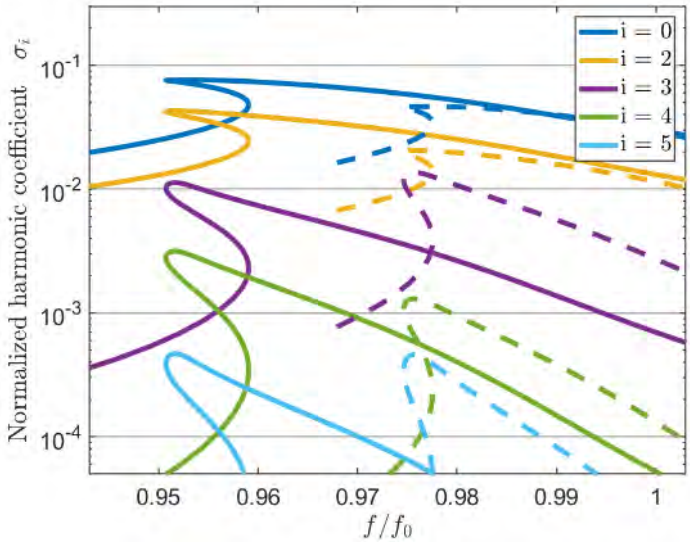

Fig 2.13 Normalized harmonic coefficients of the first mode for different curved length at the forcing level of 2 N. Solid line: $l_c/L = 0.2$. Dashed line: $l_c/L = 0.1$.

2.5 Summary

In this chapter, a cantilever beam with constant initial curvature is investigated. Combining a geometrically exact model and the shortening effect, specific to a cantilever, an inextensible condensation model is established with the consideration of initial curvature. Specific techniques are proposed to numerically implement the developed model with increased

accuracy and robustness. The proposed model explicitly shows different nonlinear stiffness and inertia terms arising from the initial curvature, as well as their interplay in the system equation. This explicit expression allows for the proposal of a modified Jacobian matrix calculation method (a necessity arising from the curvature-induced nonlinear inertia effects) involved in the HB method. Meanwhile, an OS technique is adopted and integrated into the generalized-α method for the calculation of time domain system responses.

The validity and the assumptions made for the development of the model are first validated through comparisons with COMSOL results based on linear FRFs and mode shape analyses. Results show that initial curvature and curved arclength both lead to a decrease in the resonance frequencies, more obvious when the beam is severely bent. Initial curvature causes increased longitudinal motion in the beam, which through its coupling with the transverse vibration, generates enhanced inertia effects. Numerical analyses demonstrate that both curvature-induced linear stiffness and inertia terms in the system equation are responsible for the reduction of the natural frequencies, which can be combined and regarded as effective inertia.

Confirmed by the time-domain results from the generalized-α method, nonlinear frequency responses of the first mode are shown to experience a hardening-softening transition with the increasing initial curvature. This is accompanied by a similar softening process in the harmonics. NFR curves become complex at a high forcing level which might create reversed trend from softening to hardening. The physical process behind can be explained. In fact, the

initial curvature of the beam generates significant inertia effects which compete with the stiffness effects. With a sufficiently high forcing level, the stiffness effects eventually overwhelm and prevail to produce the observed softening-to-hardening reversion. Higher modes, at an increased forcing level, show slight frequency downshifting while experiencing asymmetric responses. Both phenomena become more obvious when the forcing level increases.

As a final remark, this chapter puts emphasis on some fundamental issues related to the intrinsic nonlinearities and inertia-induced features in an initially deformed cantilever from the perspective of system modeling and analyses. Thus, the proposed model can be utilized in the next Chapter, to analyze and examine geometrically nonlinear features of ABH beams with imperfect geometry.

Chapter 3. Geometrically Nonlinear Features of ABH Beams with Imperfect Geometry

3.1 Introduction

A prefect Acoustic Black Hole (ABH) structure features a thickness reduction according to a power-law profile. This slows the propagating velocity of the bending waves and entails energy concentration towards the ABH tip, so that a small amount of damping covering the thinnest part would efficiently absorb vibrational energy. Meanwhile, the reduced wave speed inside the structure is also conducive to reducing the sound radiation of the structure. Owing to the salient ABH features, it is possible to efficiently manage the structure-bone vibration in engineering applications, as reviewed in Section 1.2.2.

Although ABH structures exhibit exceptional properties at high frequencies, their low-frequency effects are deficient, especially below the cut-on frequency [18]. The extension of the ABH length is a prevalent and straight forward approach to reduce the frequency threshold. Nevertheless, an excessively long ABH structure gives rise to a large vibration amplitude towards the ABH tip, resulting in noticeable geometric nonlinearities that challenge both numerical simulations and experimental studies. Extensive research has been conducted on the geometrically nonlinear features and mechanisms of uniform beams, whereas, except for limited efforts, there is a lack of numerical and experimental research focused on ABH beams, both quantitatively and qualitatively.

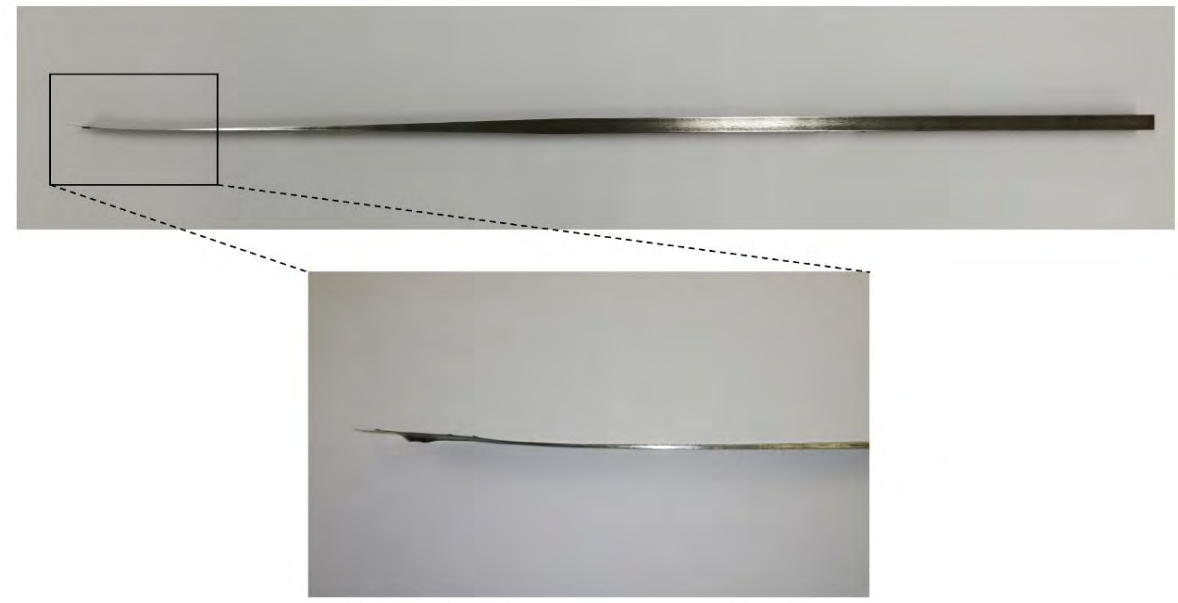

Fig 3.1 An ABH beam with a curved and thin end tip.

In addition, the geometric properties of ABH beams in practical applications may deviate from ideal conditions due to the limitations of manufacturing. As shown in Fig 3.1, an experimental sample is usually imperfect and has a curved and thin part towards the ABH tip. This is typically caused during the manufacturing process, in which thermal stresses were generated and unevenly distributed inside the beam. Besides, the thickness of a long ABH beam cannot be consistently reduced in certain areas near the ABH tip, which could form a platform due to the machining accuracy. Both geometric imperfections can affect geometric nonlinearities and lead to complex nonlinear responses, which up to now, have not been systematically investigated and exploited. Indeed, challenges persist in the direct measurement of an ABH beam with imperfect geometry, mainly arising from the presence of a very thin truncation thickness. Meticulous cares should be taken to determine the primary geometric parameters to establish a meaningful model.

Therefore, this Chapter mainly focuses on geometrically nonlinear features of perfect and imperfect ABH beams and confirms the simulation results with experiments.

3.2 Numerical model and experimental setup

The hardening/softening effect in a nonlinear system relies on the dominant level of nonlinear stiffness and nonlinear inertia, and the final system responses are associated with the boundary conditions [100] and the curved condition. A typical beam structure, like the one shown in Fig 3.1, would require an accurate model for the subsequent analyses. In this paper, the inextensible condensation model, applicable to a clamped-free beam, is used to investigate nonlinear features of a cantilever ABH beam with initial curvature and to carry out parametric studies of geometric imperfections.

3.2.1 Recap on inextensible condensation model with initial curvature

When a cantilever vibrates transversely, the longitudinal strain along the neutral axis is zero, i.e., $e = 0$, which is referred to as inextensibility [93] . As a result, the deformation in two-dimension (2D) plane for an initially curved Euler-Bernoulli beam follows

$$\left(1+u'-vk_3\right)^2+\left(v'+uk_3\right)^2=1, \tag{3.1}$$

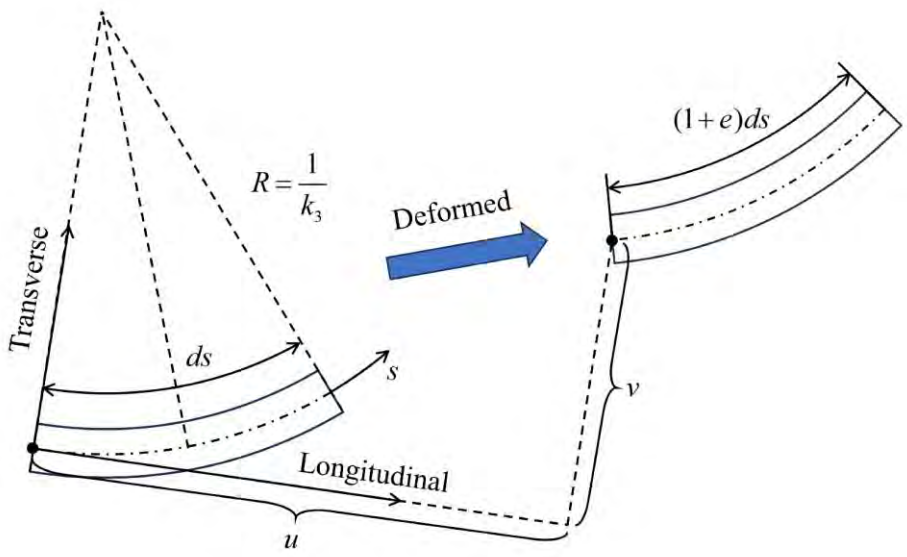

Fig 3.2 Deformation relationship of a beam segment.

where $\cdot' = \partial/\partial s$ stands for the derivative with respect to the arc length s; u and v are motions of a beam segment along longitudinal and transverse directions, respectively, and k_3 is initial curvature. Relationships among these parameters are shown in Fig 3.2. Eq.(3.1) shows that u can be represented by v with the assumption of $uk_3 \ll v'$. Therefore, the governing equations of motion along two directions can be condensed to

$$\begin{aligned} f_{ext} &= m\ddot{v} + c\dot{v} + \left(EIv''\right)'' + k_3^2\left(EIv\right)'' + k_3\left[k_3EI\left(v'' + vk_3^2\right)\Big|_0^s\right] + k_3\int_0^s m\int_s^L \ddot{v}k_3 dsds \\ &+ \left\{\begin{array}{l} \dfrac{1}{2}\left\{\left[EIv'^2\left(v'' + vk_3^2 - k_3\right)\right]' + v'^2\left[EI\left(v'' + vk_3^2\right)\right]' + 2v'\left[k_3EI\left(v'' + vk_3^2 - \dfrac{1}{2}v'^2k_3\right)\Big|_0^s\right]\right\}' \\ +k_3\int_0^s EI\left(v'' + vk_3^2\right)v'v''k_3 ds - \dfrac{1}{2}k_3\left(k_3^2EIv'^2\Big|_0^s\right) \end{array}\right\}, \\ &-\left(v'\int_0^s m\int_s^L\left(\dot{v}'^2 + v'\ddot{v}' - \ddot{v}k_3\right)dsds\right)' - k_3\int_0^s m\int_s^L\left(\dot{v}'^2 + v'\ddot{v}'\right)dsds \end{aligned} \quad (3.2)$$

by keeping nonlinear terms to the third order through the Taylor expansion. The above equation includes both linear and nonlinear effects inside the system, and comprehensively describes the interaction between nonlinear stiffness k_{nl}, nonlinear inertia m_{nl}, and initial curvature k_3.

The first row of the above equation concerns linear terms, while the second and third rows present nonlinear stiffness and nonlinear inertia terms, respectively. In consequence, the nonlinear modal behavior, hardening or softening, depends on the overall effects of nonlinear stiffness and nonlinear inertia, and the initial curvature.

The inextensible model in Eq.(3.2) is then discretized through the Galerkin approach to form element matrices and vectors. For the specific ABH beam under investigation (whose geometry and parameters are to be defined later), there are 39 beam elements with Hermitian interpolation employed in the following simulation. The linear global matrices $\mathbf{M}$, $\mathbf{K}$ are then assembled. The damping matrix is defined as $\mathbf{C} = \eta\mathbf{K}/\omega$, with a structural damping loss factor η at an excitation angular frequency ω. All nonlinear terms, including initial curvature, are regrouped into the internal force vector $\mathbf{f}_{int}$. The resultant discrete governing equation in matrix form writes

$$\mathbf{M}\ddot{\mathbf{x}} + \mathbf{C}\dot{\mathbf{x}} + \mathbf{K}\mathbf{x} + \mathbf{f}_{int} = \mathbf{f}_{ext}, \tag{3.3}$$

where $\mathbf{x}$ is the vector of the generalized degree of freedom (DOF). The above nonlinear equations, in which the external excitations are harmonic, can be numerically solved using the HB method coupled with a continuation approach, as detailed in Section 2.3.1 and the literature [110].

3.2.2 Experimental setup

The purpose of the experiments is to demonstrate the geometrically nonlinear features of the ABH beam and to confirm the geometric imperfections of the experimental sample. The experimental setup is shown in Fig 3.3. The uniform end of an ABH beam was fixed by a vice and the ABH tip was set free. An impedance head (DYTRAN 5860B) was glued to the beam surface and connected to the electrodynamic shaker (TIRA TV51075), which was driven by a power amplifier. The vibration velocity of the beam was measured by a laser vibrometer (Polytec NLV-2500-5). The force and velocity signals were transmitted to the data acquisition hardware (Simcenter LMS SCADAS) and subsequently processed by the Simcenter Testlab software.

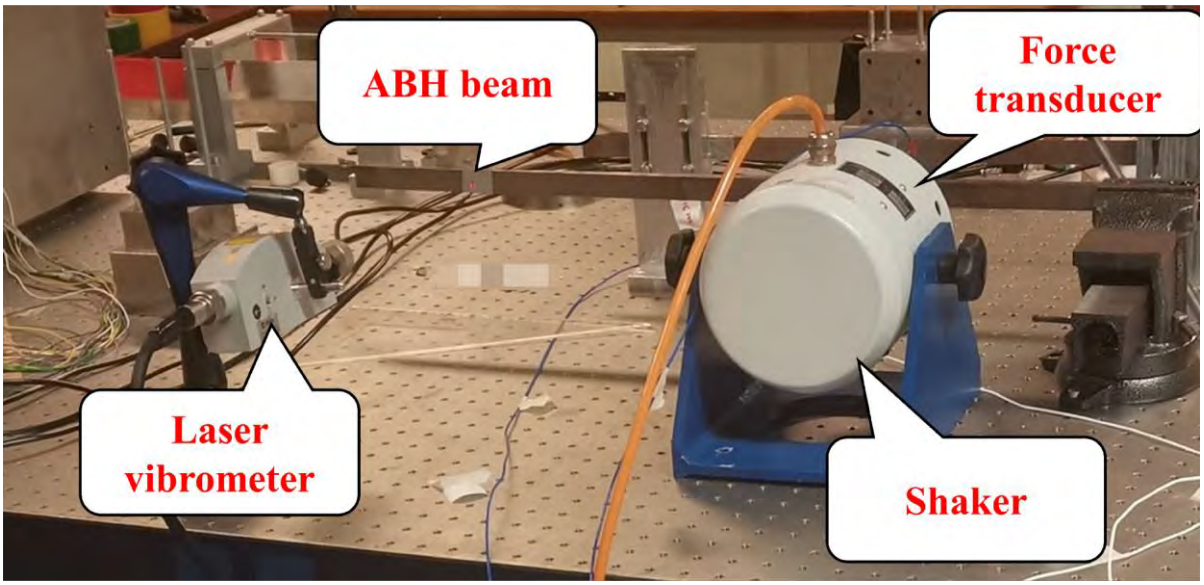

Fig 3.3 Experimental setup.

The swept and stepped sine testing interface were used to conduct linear and nonlinear tests, respectively. The former was achieved using a low forcing amplitude, while the latter was

accomplished by increasing the excitation levels. Linear results were obtained using a sweep excitation signal at a rate of $5\ \mathrm{Hz}/s$, and results were averaged over 40 measurements, thus minimizing experimental error and increasing data confidence level. The stepped sine testing interface was run for nonlinear tests, in which the force amplitudes were controlled via negative feedback to provide stable responses at each frequency point. The range of force variations were constrained within a tolerance of ± 1 dB relative to the base force level.

3.3 Numerical results

3.3.1 Updating of geometric parameters

As shown in Fig 3.1, a realistic ABH beam, in contrast to the ideal one, is truncated with finite thickness at the free end, and geometric imperfections arise from the machining inaccuracy as mentioned in Introduction. That makes it imperative to update geometric parameters of the numerical model through experimental comparisons. Fig 3.4 shows the diagram of a cantilever ABH beam, whose general thickness profile is expressed as

$$h=\begin{cases}\varepsilon\left(x-x_0\right)^m+h_0, & x_s\le x<x_m\\ h_u, & x_m\le x\le x_e\end{cases} \tag{3.4}$$

where ε is a constant; x_0 is the origin of the thickness profile; m is a power exponent usually greater than or equal to 2; h_0 and h_u are the half thickness of the platform and the uniform part, respectively. It is worth noting that the thickness profile in Eq.(3.4) does not include the initial curvature k_3 for further parameter updating. This omission is justified by

the limited effects of k_3 on the linear results, even for the extremely curved configuration [65], which will also be demonstrated later. The cantilever ABH beam has a free end at x_s and a clamped end at x_e. The entire beam is composed of the ABH part from x_s to x_m and the uniform part from x_m to x_e with a rectangular cross-section (width w, height $2h$), which has an area $A = 2wh$ and a moment of inertia $I = 2wh^3/3$. In addition to the parameters pertaining to the power-law thickness (to be updated later), the rest of the geometric parameters (directly measured) and material parameters of the ABH beam are given in Table 3.1. An external excitation force is applied at the uniform part at x_f, and system response is measured close to the ABH tip at x_p.

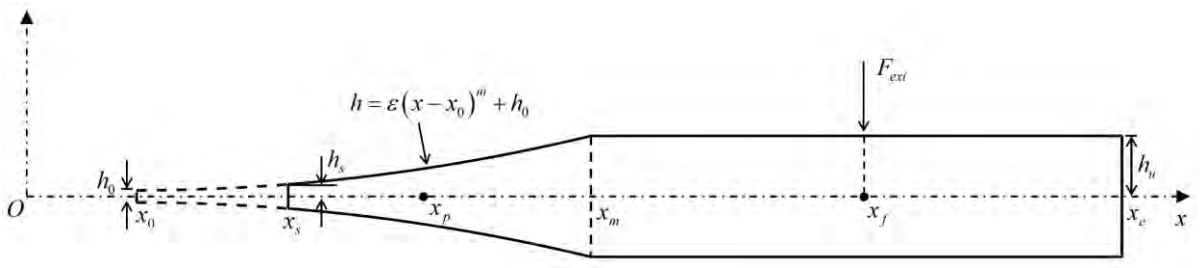

Fig 3.4 Schematic diagram of a straight cantilever ABH beam.

Table 3.1 Parameters of the ABH beam.

Geometry	**Material**
$x_s = 83$ mm, $x_m = 400$ mm, $x_e = 750$ mm	$\rho = 7850$ kg/m^3
$x_p = 200$ mm, $x_f = 600$ mm, $l_{ABH} = 317$ mm	$E = 200$ GPa
$L = 667$ mm, $h_u = 5$ mm, $w = 20$ mm	$\eta = 0.005$

Unlike the length of the beam, the geometric parameters of the tapered ABH profile are

difficult to be accurately obtained by normal measurements, especially for a long ABH beam with very thin tip. The uncertainty in the ABH profile was identified as the main modeling error. Thus, three parameters x_0, m and h_0 in Eq.(3.4) are chosen to be updated according to the experimental results. The constant ε is obtained by $\varepsilon = (h_u - h_0)/\ x_m - x_0\ ^m$. To evaluate differences between the numerical model and the experiment, an objective function G is built as

$$G = \left\| \log_{10}\left(\mathbf{H}_{\text{Model}}\right) - \log_{10}\left(\mathbf{H}_{\text{Experiment}}\right) \right\|, \tag{3.5}$$

where the vector $\mathbf{H}\ f\ = \boldsymbol{x}(f)/F$ contains the cross-point mobility. The objective is to minimize G to mitigate the model error. This approach has been widely employed in many structural analyses based on model updating, as reviewed in [129]. This paper hence makes use of the particle swarm optimization (PSO) method, a nature-inspired intelligent algorithm, to update the parameters ($\varepsilon,\ x_0,\ m,\ h_0$), under imposed constraints as listed in Table 3.3. The result is obtained when the variation between the ten consecutive values of G is lower than 10^{-6}.

The Bode plot of linear results is shown in Fig 3.5. The frequency band along the horizontal axis is capped at 400 Hz with a frequency resolution of $\Delta f = 0.5$ Hz. The magnitude of frequency response function (FRF) curves is expressed in $20\log_{10}\mathrm{H}(f)$ dB, and the phase angle changes within ± 180 degrees. Together with the phase variation, six main experimental modes are marked by M1-M6 (with M standing for "measured") in Fig 3.5(a), albeit mode M1 is barely visible. Based on the experimental data sets, the numerical model is updated and its

FRF curve is also shown in Fig 3.5(a). It can be seen that the updated model generally agrees well with the experimental results, whereas only five main modes (denoted by N1-N5, with N standing for “numerically predicted”) are found. M1 mode is missing in the updated model. The reason is that the thickness profile of the ABH part is determined by the global parameters ($\epsilon,\ x_0,\ m,\ h_0$), minor variations of which can affect the results. As a result, it is difficult to fit every single mode, especially in the presence of local geometric imperfections. Despite that, all major modes involved in the system response are well represented by the updated model. Table 3.2 lists the resonant frequencies of the experiments and the updated model. Apart from mode M5(N4), the discrepancies between them are less than 3 Hz.

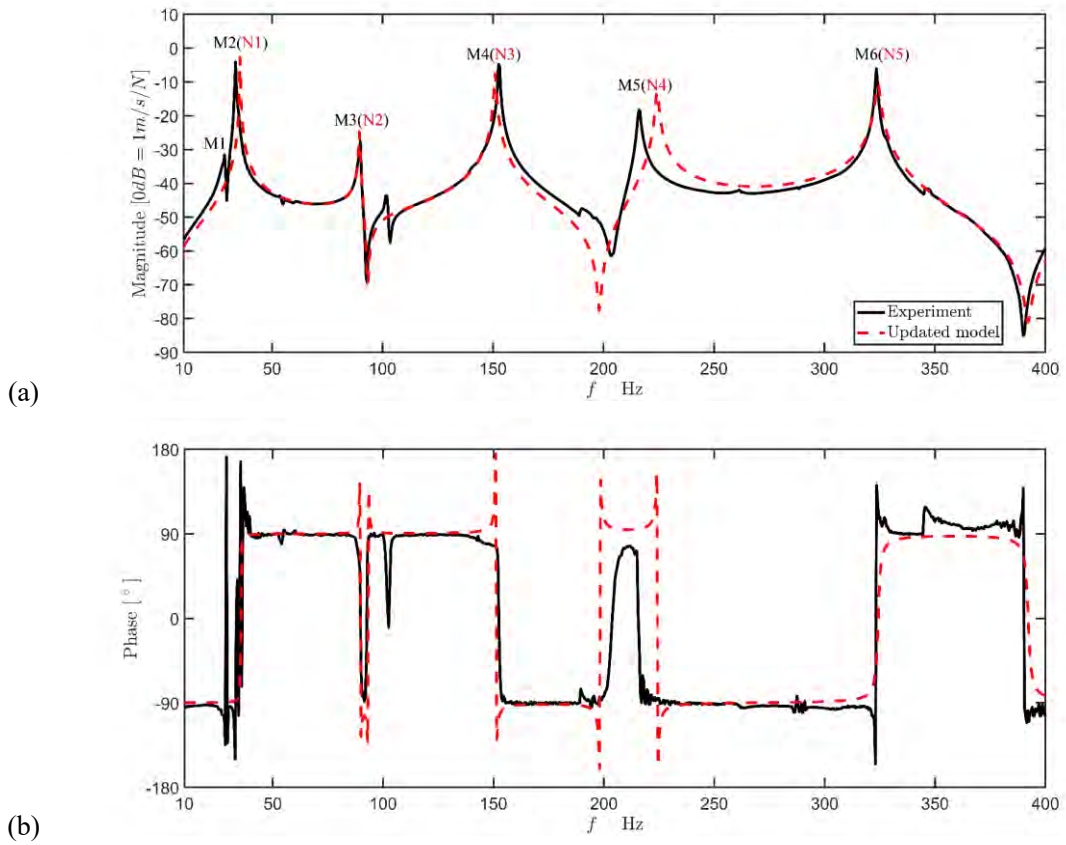

Fig 3.5 Comparisons of the experiment and the updated model. (a) FRF, (b) Phase angle.

Table 3.2 Resonant frequencies (Hz) of the experiment and the updated model.

Modes	M1	M2(N1)	M3(N2)	M4(N3)	M5(N4)	M6(N5)
Experiment	29	33.5	90	152.5	216	323.5
Updated model	/	35.5	89.5	151	224.5	324

Table 3.3 Geometric parameters of the ABH profile.

Parameters	x_0 (mm)	h_0 (mm)	ε	m
Limits	$[10, 300]$	$[0.005, 0.5]$	/	$[1, 3]$
Updated	54.8	0.005	5.29×10^{-5}	2.2185

The updated geometric parameters are listed in Table 3.3. It shows that the updated power exponent m is greater than 2, indicating that the experimental sample does obey the theoretical requirement on an ABH profile (m equal to or greater than 2). Meanwhile, the ratio $h_0/h_u = 0.001$ is so small that the impact of h_0 on the linear responses is significantly limited. Therefore, h_0 can be neglected and the linear experimental results produce a perfect ABH beam.

3.3.2 Geometrically nonlinear features of ABH beams

Due to large vibration amplitudes, especially at the tip portion, geometric nonlinearities are prevalent in flexible ABH beams, while relevant research is inadequate and the

geometrically nonlinear characteristics and mechanisms of an ABH beam (perfect or imperfect) are still unknown. Moreover, the effects of the geometric imperfections, which are not identified in the above linear studies, could be amplified by nonlinear effects, e.g., the first mode exhibits a hardening-to-softening transition in the uniform beam, due to the fact that a short portion of the beam is curved. This section focuses on the nonlinear studies of the perfect ABH beam and the effects of imperfect geometry. The HB method is used to perform nonlinear simulations with the parameters of $N_H = 5$ and $N_T = 128$.

3.3.2.1 ABH beams with perfect geometry

Subjected to high excitation levels, the nonlinear frequency response (NFR) curves of the perfect ABH beam (without initial curvature) around the first three modes (N1-N3) are first shown in Fig 3.6(a)-(c). The horizontal axis is the normalized frequency, and the vertical axis is the displacement of the beam at $x = x_p$. As observed in Fig 3.6(a), the first mode (N1) for the perfect ABH beam hardens as the excitation force increases. Contrary to a uniform beam, Fig 3.6(b) shows that the present ABH beam exhibits a significant hardening behavior for the second mode. This particular nonlinear phenomenon can be explained by the intrinsic nonlinearities of the cantilever beams. As reported in Chapter 2, a free boundary gives rise to the nonlinear inertia m_{nl}, which dominates in the high order modes and lead to a softening effect. However, the structural thickness of the ABH beam continuously decreases towards the free end, which results in a corresponding reduction in the inertia-induced effects. Besides, the

nonlinear stiffness effects are enhanced due to larger vibration amplitudes. This consequently changes the dominant level of the two competing effects. To illustrate these effects, k_{nl} and m_{nl} are individually calculated in the case of the second mode with $F = 3$ N, and the results are shown in Fig 3.6(d). As observed, the nonlinear stiffness k_{nl} has a greater impact on the frequency shift than the nonlinear inertia m_{nl}, hence leading to a hardening tendency in the second mode. Nevertheless, the third mode in Fig 3.6(c) shows a softening behavior, indicating the dominance level of m_{nl} for higher-order modes. In addition to the variation of the nonlinear modal tendency, there is also an increase in geometric nonlinearities as the modal order becomes higher. More specifically, with an excitation force of $F = 10$ N, the first mode exhibits a linear behavior, while the second mode shows a notable frequency shift of 0.014, which further increases to 0.0146 for the third mode. This is due to the efficient energy concentration in the high order modes.

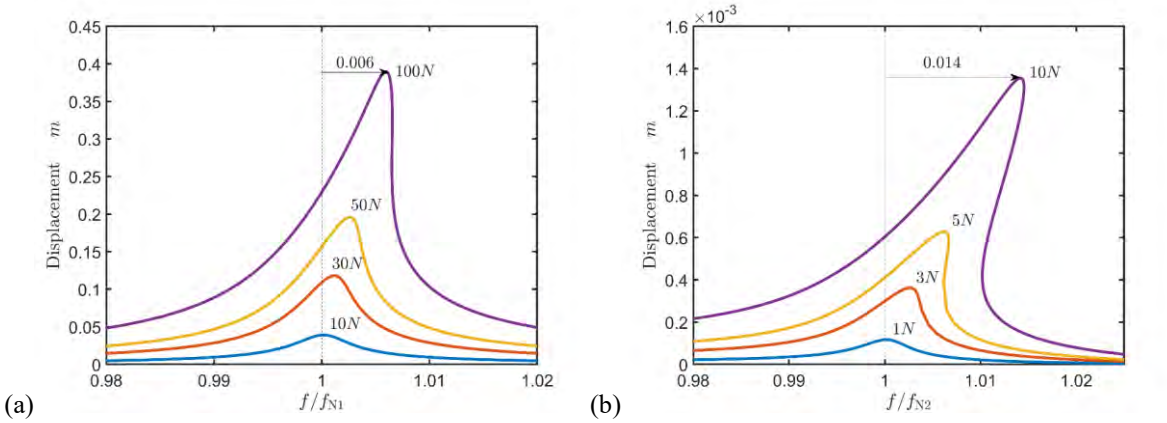

(a) (b)

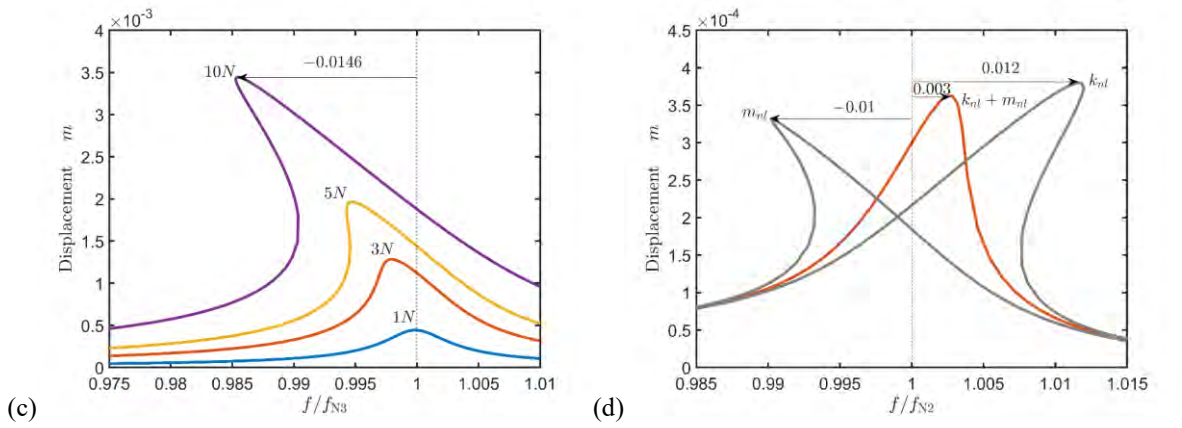

Fig 3.6 NFR curves of the perfect ABH beam around the first three modes. (a)-(c): Modes N1-N3, (d) Mode N2, $F_{ext} = 3$ N.

3.3.2.2 Effect of initial curvature

This part of the study examines the curvature-induced effect on the linear and nonlinear behavior of the ABH beams, affected by two factors, i.e., the magnitude of the initial curvature k_3 and the initially curved length in the ABH beam. The latter is represented by the factor r_c, which is defined as

$$r_c = \frac{x - x_s}{l_{ABH}}, \quad x_s \le x \le x_m, \tag{3.6}$$

which considers the curved part within the ABH portion and varies between 0 and 1.

Linear simulations are first carried out to investigate the initially curved ABH beam with a length of l_{ABH}, i.e., $r_c = 1$. The inextensible model with initial curvature is numerically solved by the HB method with $N_H = 1$. The reference solutions are provided by the Comsol software with the interface of solid mechanics. Fig 3.7 shows the linear FRF curves with a

frequency resolution of $\Delta f = 1$ Hz. As seen, the present model agrees well with the results of Comsol, except for a slight deviation at the first mode in Fig 3.7(b). However, regardless of initial curvature k_3 with the value of 0.1π or 0.5π, the linear results of the curved configuration are virtually identical to those of the straight one. Accordingly, the effect of the locally curved length ($r_c < 1$) is even less, which could justify the omission of k_3 in the model updating procedure for the current experimental sample as shown in Fig 3.5.

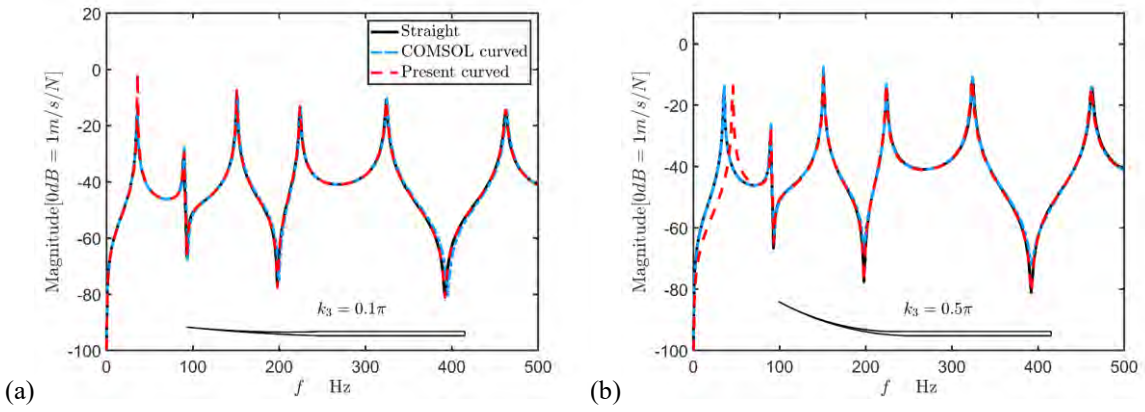

Fig 3.7 FRFs of the curved ABH beam with $r_c = 1$: (a) $k_3 = 0.1\pi$, (b) $k_3 = 0.5\pi$.

Despite the limited effect of initial curvature on the linear results, nonlinearity could result in significant changes in the system response. From a straight configuration $k_3 = 0$ to a curved configuration $k_3 = \pi$, Fig 3.8 shows the nonlinear frequency response (NFR) curves of the locally curved ABH beam with $r_c = 0.108$ for modes N1 and N2 and $r_c = 0.218$ for mode N3. As observed in Fig 3.8(a), the hardening effect of the first mode (N1) is enhanced with increasing k_3 and the frequency shift increases by 26.9% from 0.0026 to 0.0033 for $k_3 = 0 \rightarrow \pi$. Fig 3.8(b)-(c) illustrate similar phenomena for modes N2 and N3. The observed phenomenon is explained as follows. From Eq.(3.2), it can be seen that initial curvature k_3

generates not only quadratic terms, but also cubic terms involving nonlinear stiffness and nonlinear inertia. For the ABH beam, the curved area partially covers the tapered ABH tip, where the inertia effect is diminished but the stiffness effect is relatively enhanced. As a result, the initial curvature coupled with the typical nonlinear features of ABH beams leads to a hardening tendency in the first three modes (N1-N3), which differs from that of uniform beams.

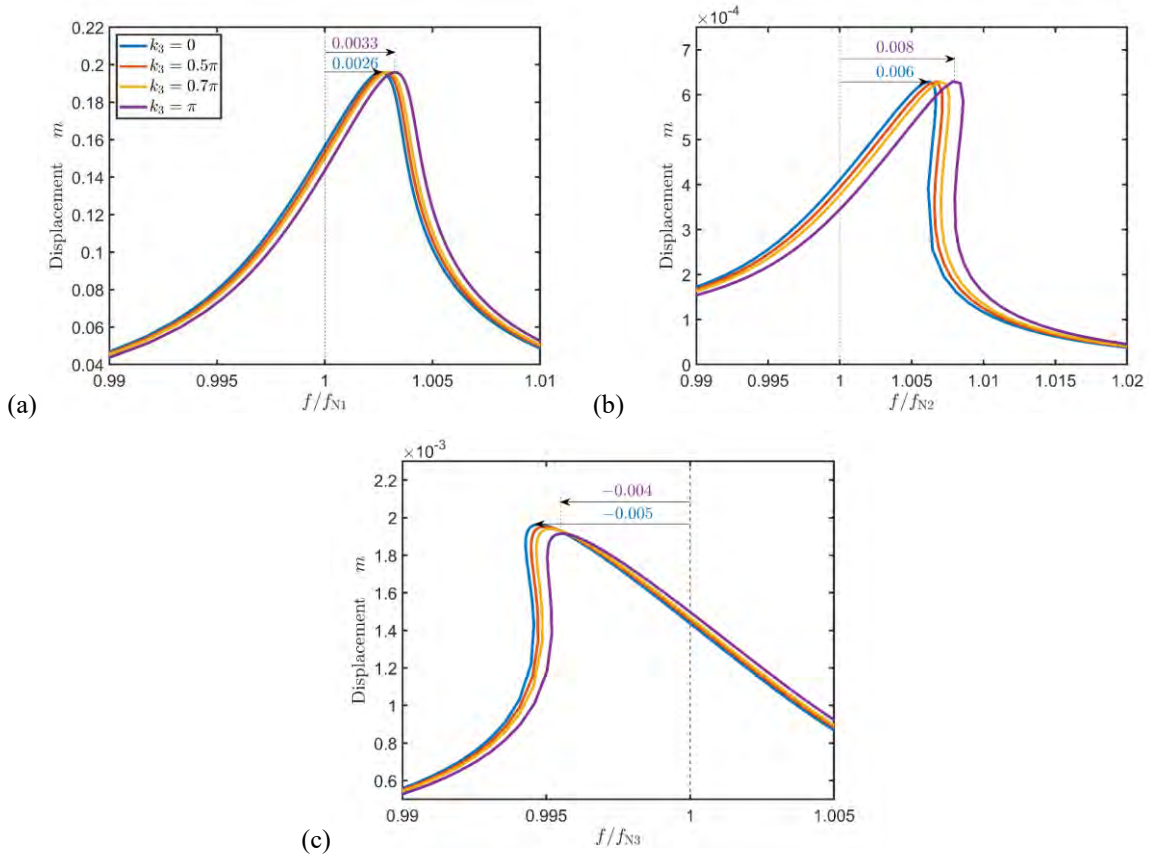

Fig 3.8 NFR curves of the locally curved ABH beam: (a) Mode N1, $r_c = 0.108$, $F_{ext} = 50$ N, (b) Mode N2, $r_c = 0.108$, $F_{ext} = 5$ N, (c) Mode N3, $r_c = 0.218$, $F_{ext} = 5$ N.

3.3.2.3 Effect of embedded platform

In addition to the initial curvature, the platform, as an embedded ABH part of uniform

thickness over the tip, is another substantial component to be considered. Not only this can result from the manufacturing process as one type of geometric imperfections, but it can also be intentionally added to achieve enhanced ABH effects as illustrated in a previous study [64]. The platform length is then parametrically investigated from both linear and nonlinear perspectives. Unlike adding an extended platform to an ABH beam, the platform in this study is embedded within the ABH beam as shown in Fig 3.9. The current ABH beam consists of three components, and the thickness profile is given by

$$h=\begin{cases} h_s, & x_s \le x < x_{pf} \\ \varepsilon_{pf}\left(x-x_{pf}\right)^m + h_s, & x_{pf} \le x < x_m \\ h_u, & x_m \le x \le x_e \end{cases}, \tag{3.7}$$

where h_s is the half thickness of the platform, which is identical to the truncation thickness of the abovementioned updated model; x_{pf} is the end point of the platform; m is the same power exponent tabulated in Table 3.3, and ε_{pf} can be determined once x_{pf} is given. As in the initial curvature study, the length of the embedded platform is described by a dimensionless factor r_{pf}, defined by

$$r_{pf}=\frac{x_{pf}-x_s}{l_{ABH}}. \tag{3.8}$$

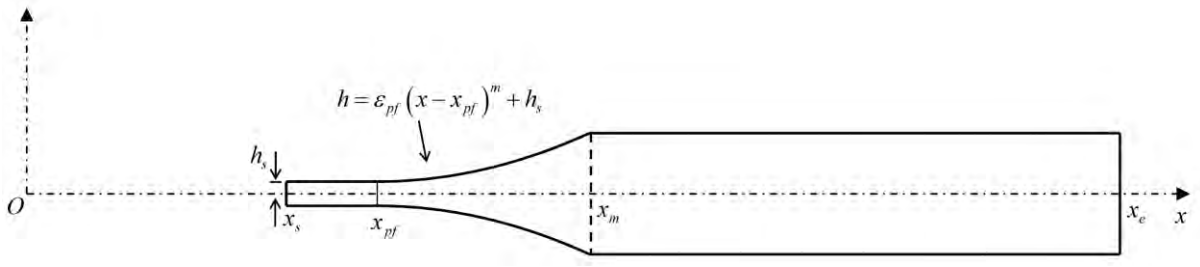

Fig 3.9 Schematic diagram of a platform-embedded ABH beam.

The first two modes (N1 and N2) are investigated in the following. Fig 3.10 shows the linear FRF curves of the ABH beam with the different value of r_{pf}. The frequency is normalized by the first natural frequency of the experimental results (f_{M1}) and the simulation results (f_{N1}), respectively. As seen in the closeup of Fig 3.10(a), compared to the perfect ABH beam (dashed line), a dramatic frequency reduction occurs in the second mode (N2) of the configuration $r_{pf} = 0$, which shows a reduced frequency gap between modes N1 and N2. As observed in Fig 3.10, with increasing r_{pf}, the frequency gap narrows and reaches a minimum near $r_{pf} = 0.03$, while it broadens when $r_{pf} > 0.03$. As $r_{pf} = 0 \rightarrow 0.04$, the peak of mode N1 decreases while the peak of mode N2 increases, and both peaks fluctuate by more than 30 dB. This is due to the change in mode shapes, as shown in Fig 3.12, in which the shadowed zone denotes the ABH portion. In Fig 3.12(a) for mode N1, the ideal ABH beam does not exhibit any local deformation, but rather an overall bending vibration. However, with the introduction of a platform, the local waves start to propagate into the ABH part, showing an amplified ABH effect of the first mode in comparison to the perfect ABH beam. This phenomenon is also reported in the literature [64], where the extended platform in the ABH beam enhances damping effect of the first mode when damping material is deployed over the region. Moreover, the second mode in Fig 3.12(b) shows stronger wave compression for larger r_{pf}. Both results illustrate that the platform (even a short one) can significantly affect the resonant frequencies and the mode shapes of the ABH beam and enhance the ABH effects. For the first two modes (N1-N2), the results show that the configuration with $r_{pf} = 0.036$ exhibits the most similar FRF curve and phase angle curve to the experiment, both in terms of

curve shape and amplitude (Fig 3.10(b) and Fig 3.11). Therefore, this configuration is used in the next section to compare with the nonlinear experimental results.

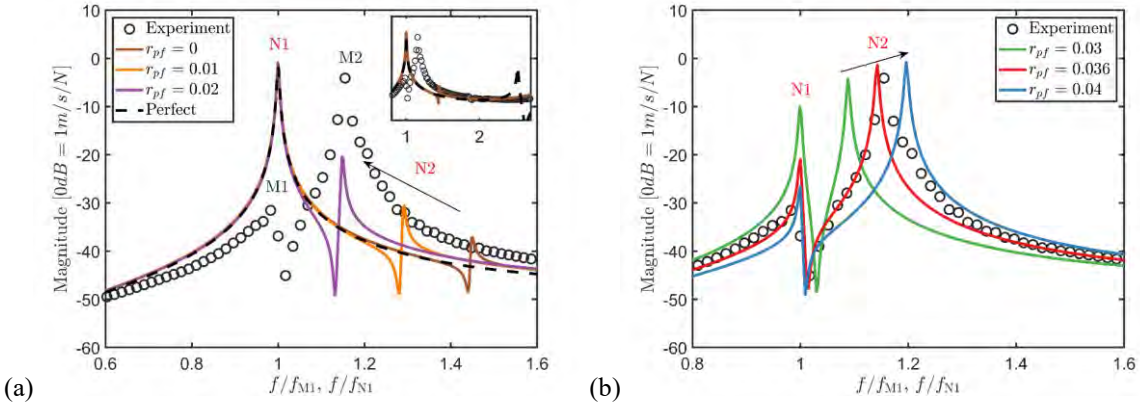

Fig 3.10 FRFs of the ABH beam with an embedded platform: (a) $r_{pf} = 0 - 0.02$, (b) $r_{pf} = 0.03 - 0.04$.

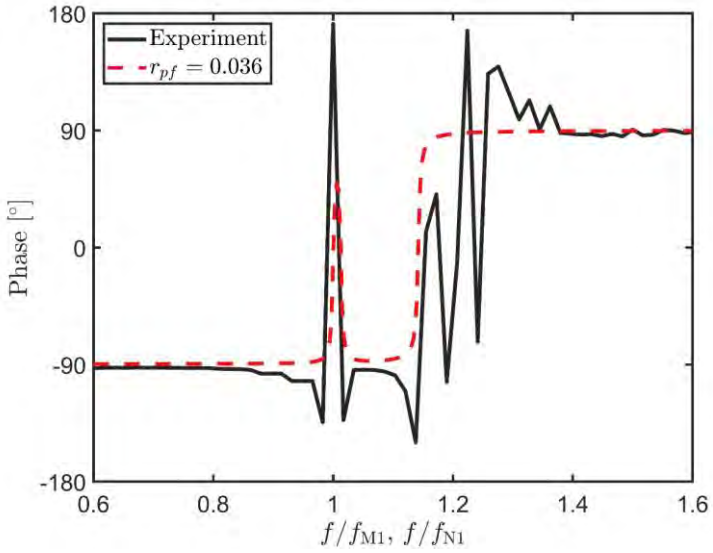

Fig 3.11 Phase angle of the ABH beam with a platform $r_{pf} = 0.036$.

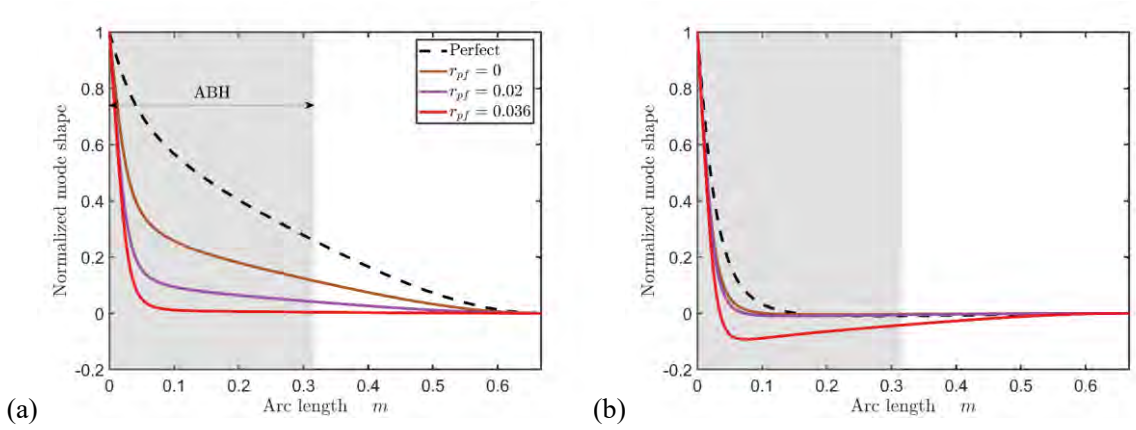

Fig 3.12 Normalized mode shapes of the ABH beam. (a) Mode N1, (b) Mode N2.

Fig 3.13 illustrate the NFR curves of the ABH beam with different platform lengths, for mode N1 (left) and mode N2 (right). For $r_{pf} = 0$ in Fig 3.13(a), the first two modes still exhibit hardening behaviors like the perfect ABH beam as shown in Fig 3.6(a)-(b), but the system exhibits enhanced geometric nonlinearities with a larger frequency shift. More specifically, in the case of mode N2 (Fig 3.13(a)), the configuration ($r_{pf} = 0$) at $F = 5$ N has a frequency shift of 0.019, larger than 0.014 in the perfect one at $F = 10$ N (Fig 3.6(b)). As r_{pf} increases from 0 to 0.036, Fig 3.13(a)-(d) show an increasing hardening tendency in the first mode, but there exists a hardening-to-softening transition phenomenon in the second mode. To be more specific, when $r_{pf} \leq 0.01$, the second mode remains a hardening behavior. For $r_{pf} = 0.03$, the second mode transits from hardening to softening with increasing excitation level. Further to $r_{pf} = 0.036$, the second mode (N2) exhibits complete softening (Fig 3.13(d)). This is due to the change in the results of the nonlinear inertia/stiffness competition. As mentioned earlier, the nonlinear inertia effect in the perfect ABH beam is attenuated by the reduced thickness profile. However, the thickness of the ABH beam with a platform is constant

and stops decreasing towards the free end, which, in turn, prevents the declining nonlinear inertia effect observed in the case without a platform. As a result, a transition from hardening to softening occurs in the second mode (N2) with increasing platform length.

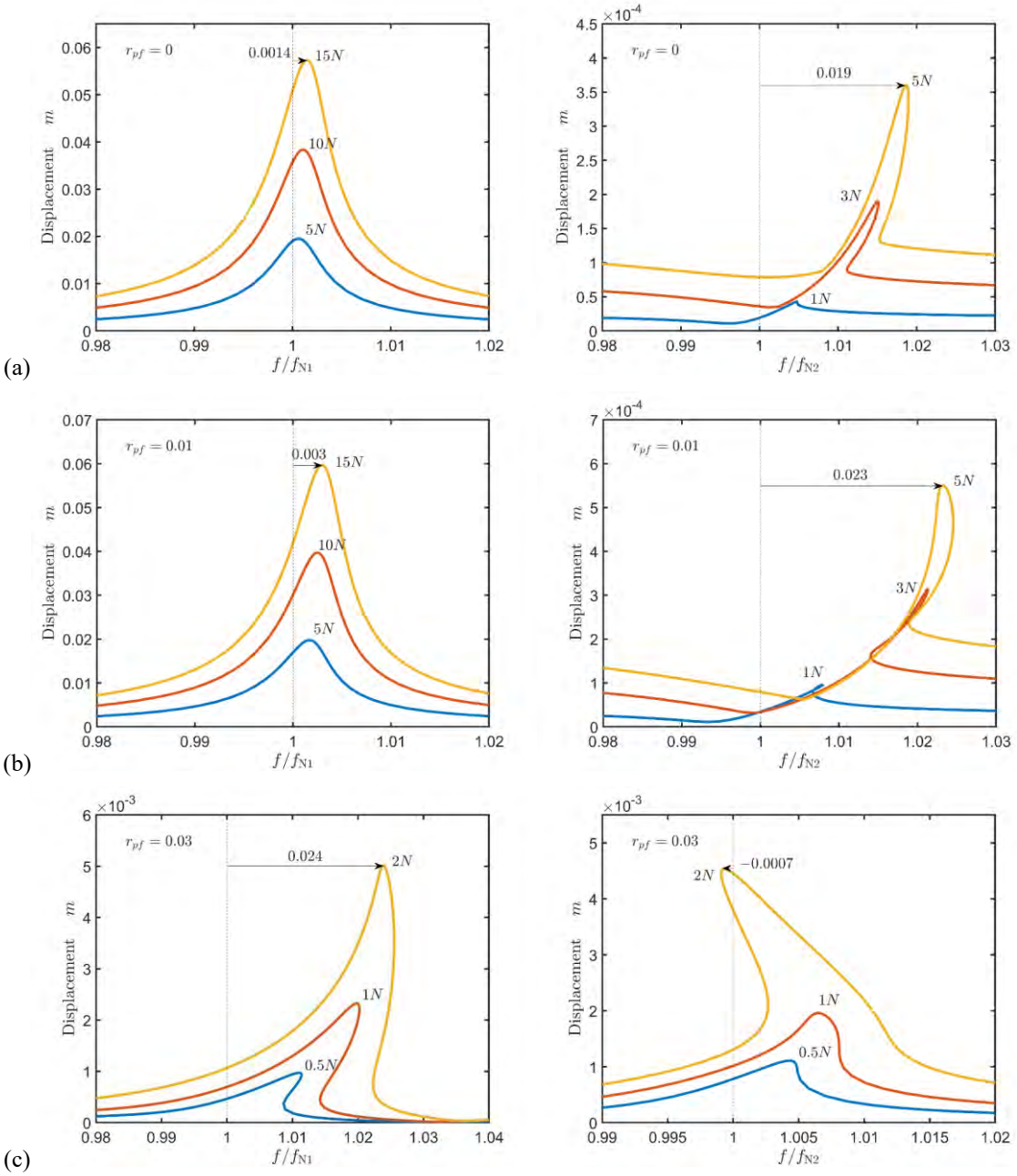

(d)

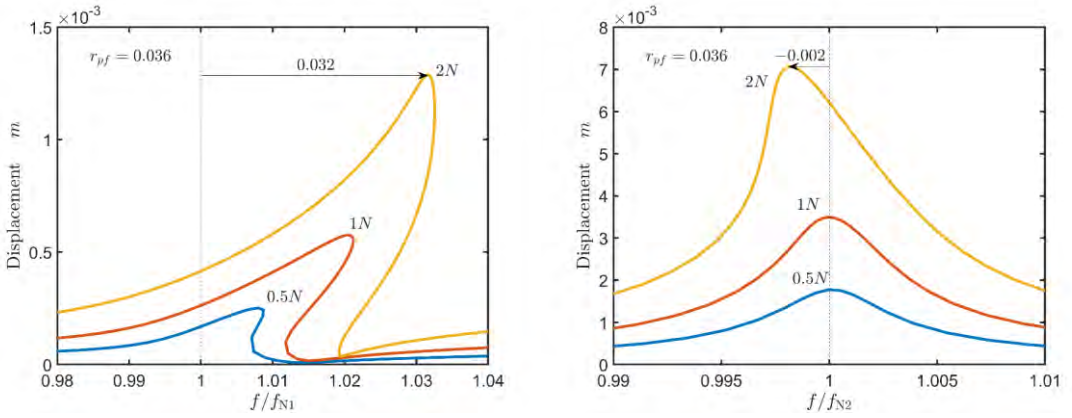

Fig 3.13 NFR curves of the ABH beam with an embedded platform: (a) $r_{pf} = 0$, (b) $r_{pf} = 0.01$, (c) $r_{pf} = 0.03$, (d) $r_{pf} = 0.036$. Left to right column: Mode N1, Mode N2.

3.4 Nonlinear experiments

3.4.1 Nonlinear modal behavior

The platform-embedded ABH beam $r_{pf} = 0.036$ is in perfect agreement with the linear experiments for the first two modes, and demonstrates the softening behavior of the second mode, which are both different from a perfect ABH beam. Therefore, this configuration is experimentally examined to demonstrate the nonlinear behavior of the second mode (M2 and N2) and confirm the geometric imperfection.

To calculate the system response around the resonant frequency, the damping conditions are investigated according to the nonlinear experimental results. Excited by $F = 1$ N, Fig 3.14(a) shows the velocity around mode M2 of the experimental results and mode N2 of the platform-embedded ABH beam ($r_{pf} = 0.036$) with different linear damping loss factors. As

mentioned earlier, the nonlinear experimental approach was implemented through a stepped sine test, and the obtained results are labeled by symbols. The circle symbols stand for experimental results using excitations from low to high frequencies, and the plus symbols represent the results with excitations sweeping in the opposite direction. It can be seen that the simulation result of $\eta = 0.005$ barely shows nonlinear modal behavior. As η decreases to 0.001, the system shows a significant frequency shift, which is very close to the experimental results. However, insufficient damping leads to a significant difference in the magnitude of the simulation and experimental results. Therefore, the nonlinear damping condition must be considered in this case to constraint the peak amplitude. Following the work [103], the quadratic nonlinear damping $\mathbf{C}_{nl}|\overline{\mathbf{x}}|\mathbf{x}$ is employed next, where $\overline{\mathbf{x}}$ is the dimensionless velocity, $\mathbf{C}_{nl}$ is the nonlinear damping matrix defined by $\mathbf{C}_{nl} = \eta_{nl}\mathbf{K}/\omega$, and η_{nl} is the nonlinear damping loss factor. Fig 3.14(b) illustrates the NFR curves with different nonlinear damping loss factors when η is set to 0.001. The optimal result is obtained when the value of η_{nl} is equal to 0.012.

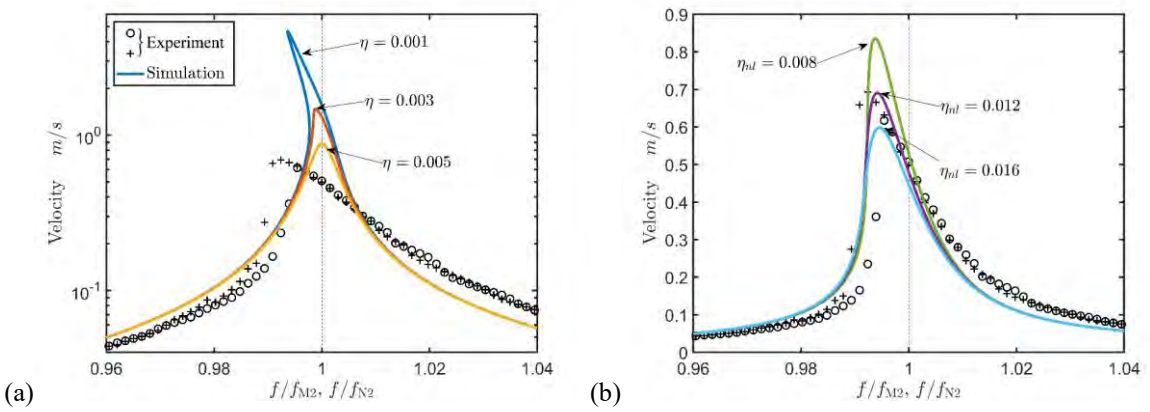

Fig 3.14 Parametric studies of damping loss factors of the platform-embedded ABH beam ($r_{pf} = 0.036$) around modes M2 and N2, $F_{ext} = 1$ N. (a) Linear loss factor η with $\eta_{nl} = 0$, (b) nonlinear loss factor η_{nl} with $\eta =$

0.001.

The damping parameters obtained from the results of $F = 1$ N are applied to the cases for $F = 0.1$ N, 0.3 N, and 0.5 N, as show in Fig 3.15. It illustrates that the simulation results agree well with the nonlinear experimental results, and as the excitation level increases, the second mode (N2) exhibits softening. These results confirm that the major geometric imperfection of the sample is from the platform, which significantly affects the linear and nonlinear system response. Apart from these, this nonlinear system shows enhanced geometric nonlinearities. With $F = 1$ N, mode N2 has a large frequency shift of 0.006 (Fig 3.15(d)). However, the perfect ABH beam, of which mode N1 matches experimental mode M2 in Fig 3.5, requires an extremely large force $F = 100$ N in order to achieve the same frequency shift (Fig 3.6(a)).

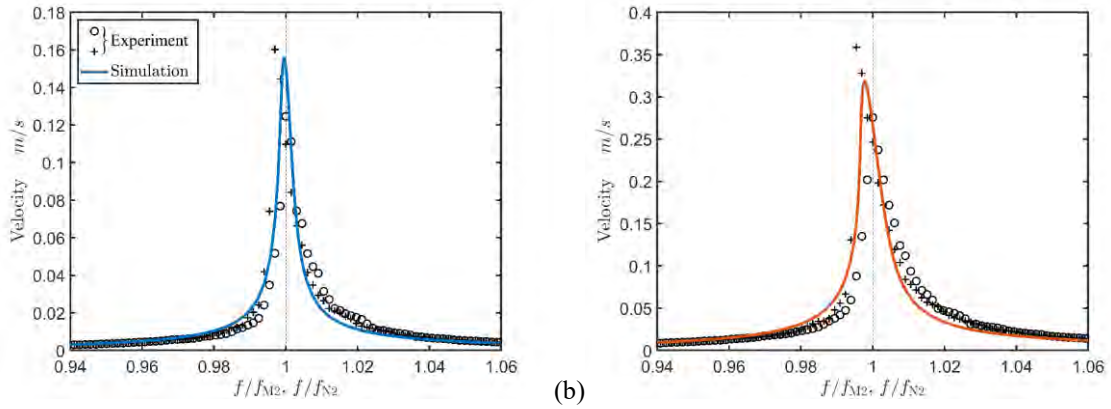

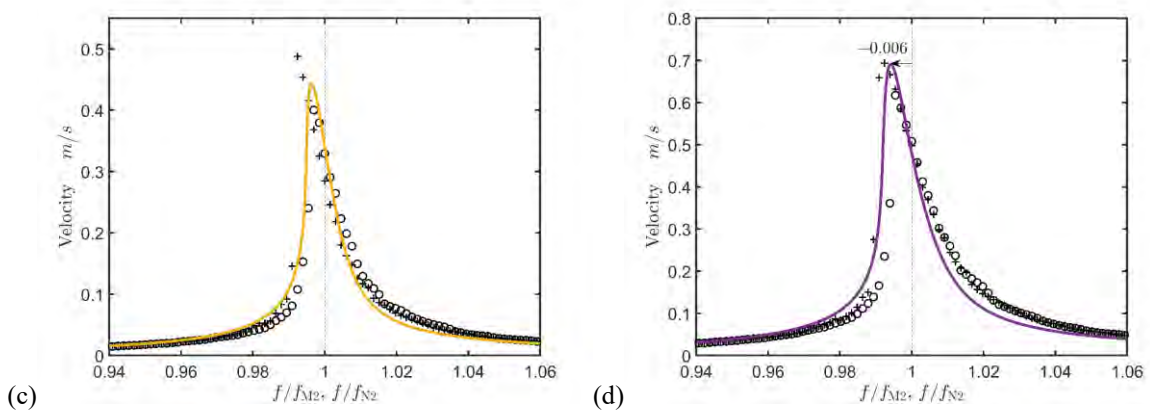

Fig 3.15 Comparisons between the experimental results and NFR curves of the numerical model ($r_{pf} = 0.036$, $\eta = 0.001$, $\eta_{nl} = 0.012$) around modes M2 and N2. (a) $F_{ext} = 0.1$ N, (b) $F_{ext} = 0.3$ N, (c) $F_{ext} = 0.5$ N, (d) $F_{ext} = 1$ N.

The above observation can be further substantiated as follows. Although mode N1 (perfect ABH beam) and mode N2 ($r_{pf} = 0.036$) agree well with experimental mode M2 in the frequency domain, two configurations show distinct mode shapes. As seen in Fig 3.16(a), the configuration $r_{pf} = 0.036$ promotes larger structural deformation at the ABH tip than the perfect ABH beam, thus enabling more energy concentration on the ABH portion. To illustrate this, the potential energy ratio of the ABH portion to the uniform portion Γ_{PE} (as defined in Section 4.3.3) is utilized to quantify the energy distribution in the beam. Fig 3.16(b) shows that the configuration $r_{pf} = 0.036$ achieves significant energy concentration even for a low excitation force of $F = 0.1$ N, which becomes more pronounced with increasing force. Therefore, the current ABH beam with a platform shows extraordinary geometric nonlinearities.

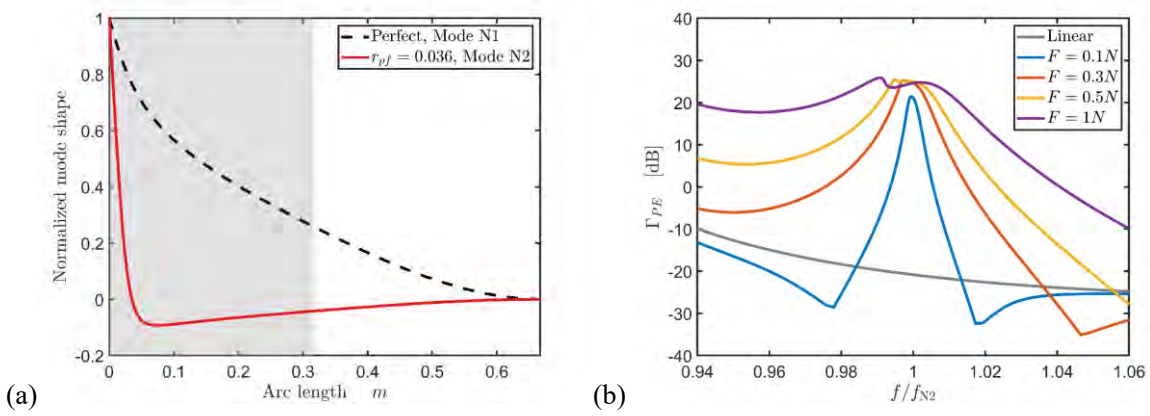

Fig 3.16 (a) Normalized mode shape of the perfect ABH beam for mode N1 and the imperfect ABH beam for mode N2, (b) potential energy ratio of the platform-embedded ABH beam $r_{pf} = 0.036$ with different forces.

3.4.2 Energy transfer

By sweeping below f_{cut-on}, the geometric and mechanical nonlinearity-induced energy transfer for ABH beams is demonstrated in Fig 3.17. The measured beam with geometric properties in Table 3.1 has a cut-on frequency of $f_{cut-on} \approx 228$ Hz, which is plotted by black dashed line in Fig 3.17. Thus, the excitation frequency varied from 25 Hz to 228 Hz at a rate of 1 Hz/s, with a sampling frequency of 12.8 kHz. The free-clamped and the cable constrained ABH beams (detailed in Section 4.4) without damping layers were excited by the voltage level of $U = 0.1V$. Fig 3.17 shows frequency results via FFT method. As seen, above f_{cut-on} (dashed line), both configurations generate higher order harmonics, typically around 300 Hz, indicating energy transfer from low to high frequencies. However, compared to the free-clamped ABH beam, the cable-constrained nonlinear ABH beam exhibits stronger energy transfer. To be more specific, the amplitude increases by 20.6 dB near 300 Hz and by 17.8 Hz

near 450 Hz. Additionally, the nonlinear cable results in noticeable vibration reduction of 14 dB for the first mode and 14.9 dB for the second mode.

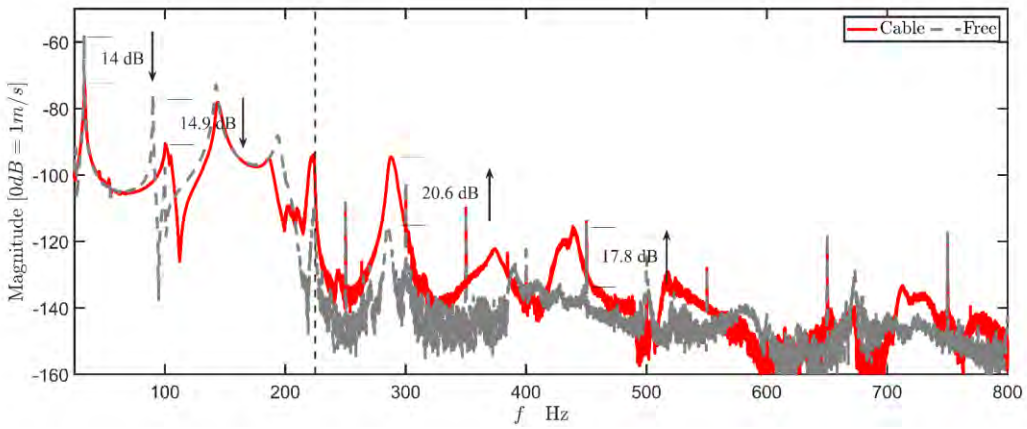

Fig 3.17 Comparison of output velocity for ABH beams with free end and nonlinear cable, $U = 0.1V$.

3.5 Summary

This Chapter investigates the geometrically nonlinear features of an ABH beam with imperfect geometry, both numerically and experimentally. Based on practical considerations, two geometric imperfection factors, initial curvature and platform, are considered to examine their effects on both linear and nonlinear responses of the system. Geometric nonlinearities of the ABH beams are modeled by an inextensible model with initial curvature, after the model updating based on linear experimental result.

Analyses lead to the following conclusions.

(a) Due to the decreasing ABH thickness profile, the nonlinear inertia effects in an ABH

beam generally reduce as compared with a uniform beam, thus resulting an amplified hardening effects in the structural modes.

(b) The initial curvature of the ABH beams, combined with the nonlinear stiffness effects, generally enhances the hardening tendency in the system, albeit limited as evidenced by both linear and nonlinear results.

(c) Numerically predicted nonlinear features are validated through experiments, showing good agreement. More specifically, the first two dominant modes with $r_{pf} = 0.036$ agree well with experimentally measured ones, thus confirming the existence of the platform in the tested ABH sample. As the platform length increases from 0 to 0.036, the second mode of the imperfect ABH beam exhibits a transition from hardening to softening, resulting from the increased nonlinear inertia effect induced by the platform. Finally, the platform-induced softening behavior in the second mode is also confirmed by nonlinear experiments.

(d) Sweeping results show that geometric nonlinearity can transfer energy from low frequencies to high frequencies, which facilitates the enhancement of low-frequency ABH effect. However, compared with mechanical nonlinearity, the effect of geometric nonlinearity is limited for the ABH beams. Meanwhile, stronger geometric nonlinearity may require a much larger structure size, which is unacceptable for current manufacturing levels and design requirements. Therefore, in order to achieve the final goal of this study, intentional nonlinearity

through mechanical coupling is proposed in the next Chapter.

Chapter 4. Enhanced Acoustic Black Hole Effect through Energy Transfer Enabled by Intentional Mechanical Nonlinearity

4.1 Introduction

As discussed in previous Chapters, the frequency limit hinders the application of ABH at low frequencies. Previous efforts focused on linear systems, such as spiral ABH beam and metamaterials with limited success, since some of the existing techniques compromised the acceptability of the structures and challenged current manufacturing capabilities. Therefore, how to improve the ABH effect below the cut-on frequency is still a bottleneck problem.

Intrinsic or intentional nonlinearities can be a useful approach to solve the problem. As shown in Fig 3.17 in Chapter 3, geometric nonlinearity can enable energy transfer into the frequency range where the ABH effect functions. Nevertheless, the energy transferred due to geometric nonlinearity is minimal, so not really meaningful in practice. To increase energy transfer with reasonable structural dimensions, intentional nonlinearity can be considered as an alternative. For example, vibro-impact ABH (VI-ABH) was investigated [113, 114]. The system used to investigate the issue was shown to generate significant energy transfer from low to high frequencies, conducive to passive vibration control at low frequencies. But the proposed process is difficult to control and might damage the fragile ABH structure if the contact points are located around the ABH portion. A nonlinear energy sink (NES) was also integrated into

the ABH structure to achieve targeted energy transfer (TET) [115-117]. In these systems, the energy of a base structure can be irreversibly transferred to the NES through nonlinear energy interactions [71] and then dissipated through NES damping. The major drawback is that there is an energy barrier in the NES, so that a low or excessively high input energy cannot trigger energy interactions to realize the TET. In addition, energy transfer was also achieved by electromechanical coupling with nonlinear capacitances in a resonant shunt which is connected to an ABH structure through piezoelectric materials [118], where a reduction in vibration amplitude was observed at low resonant frequencies. However, the circuit-induced nonlinearities in the mechanical system are relatively weak and therefore of limited benefits. Despite these efforts, research on ABH structures with strong nonlinearities, flexible tuning, and wide energy bandwidths remains understudied. Thus, this Chapter presents a feasible solution by incorporating nonlinear cables with cubic stiffness into an ABH beam.

4.2 Nonlinear ABH beam

Fig 4.1 shows a schematic diagram of a symmetrical cantilever ABH beam partially covered by two damping layers near its free end, with its end point connected to a grounded cable along its width-wise direction. The whole ABH beam consists of an ABH part and a uniform part, and their half thickness profiles are given by

$$h(x)=\begin{cases}\varepsilon x^2, & x_0 \le x \le x_m \\ h_u, & x_m < x \le x_e\end{cases}, \tag{4.1}$$

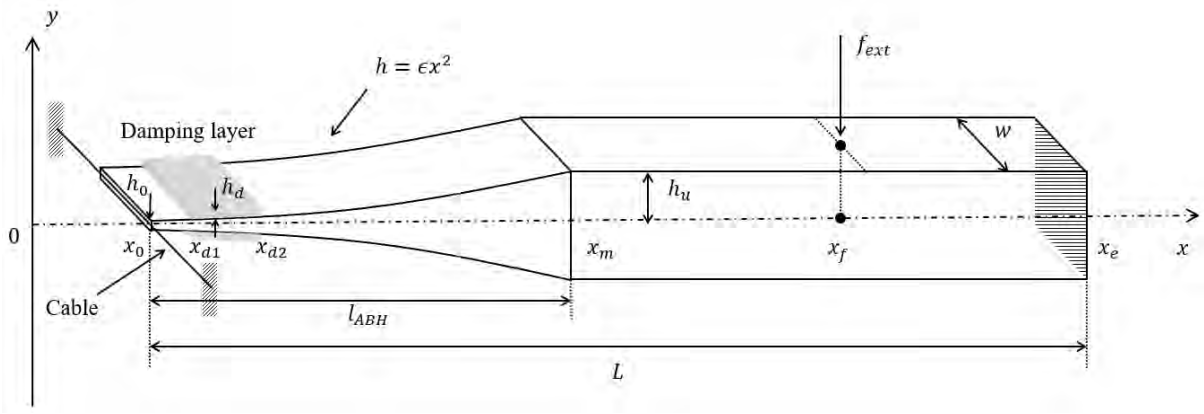

Fig 4.1 Schematic picture of a cantilever ABH beam with damping layers and grounded nonlinear cables.

where ε is a constant, and h_u is the half thickness of the uniform portion. The entire ABH beam has length L from x_0 to x_e, and the ABH portion with length l_{ABH} has the same starting point but ends at x_m. Since $x_0 > 0$, the ABH beam has a truncated thickness $2h_0$ at the end. Each damping layer has a thickness h_d and covers the ABH portion from x_{d1} to x_{d2}. k_{nl} denotes the stiffness of the grounded nonlinear cable attached to the ABH beam at the end tip x_0, where nonlinear effects are expected to arise due to the large local amplitude. Meanwhile the right end of the beam is clamped. An external force f_{ext} is applied at the location of x_f. The base beam has a width w and a rectangular cross-section with area $A = 2wh$, a moment of inertia $I = 2wh^3/3$, and is made of a homogenous material with density ρ_b, Young's modulus E_b, and structural damping loss factor η_b. The damping layers have the same width w, but different material parameters ρ_d, E_d, η_d, denoted by the subscript d.

The cross-section of the beam shown in Fig 4.2 has a transverse amplitude of vibration v that results in a strain $\Delta l_c/l_c = \sqrt{1 + (v/l_c)^2} - 1$ to produce a longitudinal force $F =$

$E_c A_c \Delta l_c / l_c$ along the cable direction, where l_c is the cable length without tension, E_c is the elastic modulus, and A_c is the area of the cross-section. Considering the vertical direction, the cubic nonlinear force generated by the cable, which is vertically applied to the beam, is written as

$$F_{nl} = 2F \frac{v}{\sqrt{l_c^2 + v^2}} \approx k_{nl} v^3 , \tag{4.2}$$

by keeping the nonlinear strain to the second order through Maclaurin expansion, and the corresponding cubic nonlinear stiffness is given by $k_{nl} = E_c A_c / l_c^3$, which can be easily tuned by the length of the cable. Obviously, the shorter the cable length, the stronger the nonlinear effect.

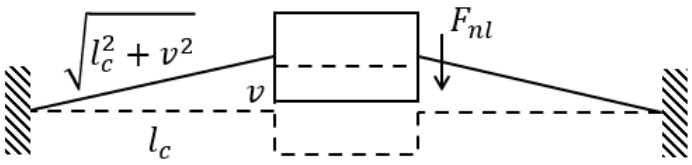

Fig 4.2 Schematic plot of the beam cross section with two grounded cables.

Based on Euler-Bernoulli beam assumptions, the displacement field of the beam can be written as

$$(u, v) = \left\{ -y \frac{\partial v}{\partial x}, v \right\}, \tag{4.3}$$

where (u, v) is the displacement of an arbitrary point on the beam and damping layer. Considering small deformations and rotations, the moment is represented by $M = EIv''$, so that the kinetic energy E_k, the potential energy E_p (including bending moment and nonlinear

force) of the entire configuration and the work done by the external force W are expressed as

$$\begin{aligned} E_k &= \frac{1}{2}\int_{x_0}^{x_e} \rho A \dot{v}^2 dx \\ E_p &= \frac{1}{2}\int_{x_0}^{x_e} EIv''^2 dx + \frac{1}{4}\int_{x_0}^{x_e} k_{nl} v^4(x,t)\delta(x-x_0)dx, \\ W &= \int_{x_0}^{x_e} f_{ext}(t) v(x,t)\delta(x-x_f)dx \end{aligned} \tag{4.4}$$

where $v = \partial v/\partial t,\ v'' = \partial^2 v/\partial x^2,\ \delta(x)$ is the Dirac delta function (for any function $f(x)$, we have $\int f(x)\delta\ x - x_0\ dx = f(x_0)$). Based on the assumption of perfect bounding between the damping layer and the base beam, the mass and moment items in Eq.(4.4) should be modified to fully couple the effects of the damping layer [13] and written as

$$\begin{aligned} EI(1+i\eta) &= \begin{cases} E_b I_b\left[1+i\eta_b + E_2\left(h_2^3+3h_2^2+3h_2\right)(1+i\eta_d)\right], & x_{d1} \le x \le x_{d2} \\ E_b I_b(1+i\eta_b), & \text{otherwise} \end{cases} \\ \rho A &= \begin{cases} \rho_b A_b(1+\rho_2 h_2), & x_{d1} \le x \le x_{d2} \\ \rho_b A_b, & \text{otherwise} \end{cases} \end{aligned}, \tag{4.5}$$

where $\rho_2 = \rho_d/\rho_b,\ E_2 = E_d/E_b,\ h_2 = h_d/h_b$, and the damping effect is involved by the complex modulus, i.e., $EI = EI(1+i\eta)$. Therefore, the Lagrangian of this system writes

$$\mathcal{L} = E_k - E_p + W, \tag{4.6}$$

where $\mathcal{L}(v, v'', v)$ depends on the displacement v, the deformed curvature v'', and the velocity v. The corresponding Euler-Lagrange equation with higher order derivatives [130] should be written as

$$\frac{\partial}{\partial t}\left(\frac{\partial \mathcal{L}}{\partial \dot{v}}\right) - \frac{\partial \mathcal{L}}{\partial v} - \frac{\partial^2}{\partial x^2}\left(\frac{\partial \mathcal{L}}{\partial v''}\right) = 0, \tag{4.7}$$

so, the governing equation of motion with the consideration of the damping effect and the cubic nonlinear stiffness is given by

$$\rho A\ddot{v}-\left(\bar{E}Iv''\right)''+k_{nl}v^3\left(x,t\right)\delta\left(x-x_0\right)=f_{ext}\left(t\right)\delta\left(x-x_f\right), \tag{4.8}$$

with boundary conditions

$$\begin{aligned} &v=v'=0, && x=x_e \\ &F=k_{nl}v^3, M=0, && x=x_0 \end{aligned}, \tag{4.9}$$

where F is the shear force, and M is the moment.

After modeling the coupled nonlinear vibration equations, numerical simulations are performed in the time and frequency domains through discrete forms of the governing equation. Adopting 1D beam elements, the displacement v in the element is approximated by the combination of the node degree-of-freedoms (DOF) $[d]_e$ and the shape function $[N]$ obtained by Hermite interpolation, i.e., $v\approx[N][d]_e$, where $[N]=[N_1\ N_2\ N_3\ N_4]$, and $[d]_e=[v_1\ v_1'\ v_2\ v_2']^T$, with the superscript T being transpose of a vector or matrix. The mass and stiffness element matrices and the force vector were calculated via a Galerkin process as

$$\begin{aligned} \mathbf{m}&=\int_0^{l_e}[N]^T\,\rho A[N]ds_e \\ \bar{\mathbf{k}}&=\int_0^{l_e}[N'']^T\,\bar{E}I[N'']ds_e \\ \mathbf{f}&=\int_0^{l_e}[N]^T\,fds_e \end{aligned}, \tag{4.10}$$

and then assembled in global matrices. Hence, the matrix form of the governing equation is expressed by

$$\mathbf{M}\ddot{\mathbf{x}}+\bar{\mathbf{K}}\mathbf{x}+\mathbf{f}_{nl}\left(\mathbf{x}\right)=\mathbf{f}_{ext}\left(\omega,t\right), \tag{4.11}$$

where **x** is the vector of generalized DOFs, **M** is the mass matrix, $\bar{\mathbf{K}}$ is the complex stiffness matrix, and $\mathbf{f}_{nl}$, $\mathbf{f}_{ext}$ are the nonlinear force and external force vectors, respectively. Neglecting the nonlinear and external forces, and assuming a periodic solution **x** with angular

frequency ω, i.e., $\mathbf{x} = \mathbf{a}e^{i\omega t}$, the characteristic equation of the linear system is

$$\bar{\mathbf{K}}\mathbf{M}^{-1}\mathbf{a} = \omega^2\mathbf{a}\,. \tag{4.12}$$

The complex natural frequency ω_n is the square root of the eigenvalues given in Eq.(4.12). The modal loss factor of the linear system, utilized in the following to demonstrate the efficient ABH damping effect, is the ratio of the imaginary and real parts of ω_n^2 [13] , which writes

$$\eta = \frac{\mathrm{Im}\left(\omega_n^2\right)}{\mathrm{Re}\left(\omega_n^2\right)}\,. \tag{4.13}$$

Unlike the linear system, the resonant frequency of the nonlinear system depends on the response amplitude, and the nonlinear normal modes are no longer orthogonal, which requires specific numerical treatments. Owing to its excellent capability to tackle weakly and strongly nonlinear problems, the harmonic balance (HB) method combined with a continuation approach [110] is used in the following to obtain the nonlinear frequency response (NFR) curves, as shown in Fig 4.3. Any point Q satisfying the target function $h\left(\boldsymbol{x},\omega\right) = 0$ in the HB method, will be the solution of the nonlinear problem and will form a "solution branch". Due to the continuation method (path-following), these solution points are continuous along the branch, where Q_k is the *k*-th point, and P in Fig 4.3 represents the peak point along the curve. Alternatively, the Generalized-α (G-α) method [111], a time-integration method for both linear and nonlinear cases, is adopted to predict the nonlinear dynamic behaviors in the time domain, and results are often used to confirm the NFR curves in the frequency domain, as detailed in Section 2.3.2.

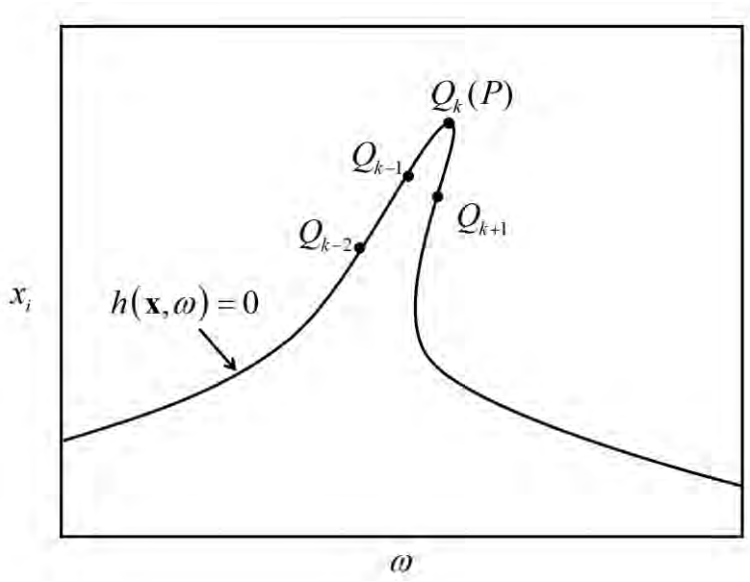

Fig 4.3 Diagram of a NFR curve in the frequency domain.

4.3 Numerical results and analyses

This section focuses on numerical simulations of an ABH beam to demonstrate ABH-induced features in the linear system and the enhanced ABH effect below the cut-on frequency through intentional nonlinearity. Both the cantilever ABH beam and the damping layer are made of isotropic and homogeneous materials with the geometric and material parameters listed in Table 4.1. The damping matrix was given through an equivalence principle, defined as $\mathbf{C} = \mathrm{Im}(\overline{\mathbf{K}})/\omega$. In order to capture local wave patterns, the element distribution in the ABH portion was arranged in a geometric sequence, with the smallest element at the free end tip, whereas equally spaced elements covered the rest uniform portion of the ABH beam. Mesh independence studies were carried out for the linear and nonlinear cases, using three sets of meshes ranging from coarse to fine, as discussed in Section 4.3.1. Accordingly, a regular mesh

of 30 elements was used to simulate linear and nonlinear cases. The first three natural frequencies in the current configuration are $f_1 = 30.94$ Hz, $f_2 = 91.66$ Hz, $f_3 = 174.44$ Hz.

Table 4.1 Geometric and material parameters of the beam and damping layer.

Geometric parameters	**Material parameters**
ABH beam	
$x_0 = 63$ mm, $x_m = 400$ mm, $x_e = 750$ mm	$\rho_b = 7850\ \mathrm{kg/m^3}$
$x_f = 700$ mm, $l_{ABH} = 337$ mm, $L = 687$ mm	$E_b = 200$ GPa
$\varepsilon = 3.125 \times 10^{-5}\ \mathrm{mm^{-1}}$, $h_u = 5$ mm, $w = 20$ mm	$\eta_b = 0.005$
Damping layer	
$x_{d1} = x_0, x_{d2} = x_{d1} + 50$ mm	$\rho_d = 950\ \mathrm{kg/m^3}$
$h_d = 0.5$ mm	$E_d = 5$ GPa
	$\eta_d = 0.3$

4.3.1 Convergency study

This section discusses the mesh independence study in linear and nonlinear cases. There are three sets of meshes with a different number of elements, ranging from coarse (18 elements), regular (30 elements) to refined meshes (49 elements), as shown in Fig 4.4. The elements in the ABH portion are arranged according to a geometric sequence, with the smallest element

located at the free end to capture the shortened wavelength, whereas the elements in the uniform portion are equally spaced. The natural frequencies are calculated on three sets of meshes and the results are listed in Table 4.2. It shows that the differences of each mode are less than 1 Hz for modes up to the 5th order. In fact, the regular mesh exhibits converged results in the linear case. The convergency study on the nonlinear case was also carried out. Considering the excitation level of $F_{ext} = 5$ N, NFR curves around the first mode with harmonic number $N_H = 5$ and nonlinear stiffness $k_3 = 10^9$ N/m^3 are illustrated in Fig 4.5. The results show that all meshes have converged outcomes. Therefore, a regular mesh of 30 elements is used in the following investigations. Meanwhile, the choice of the number of harmonics N_H is according to a convergence study as follows. Fig 4.6 shows the NFR curves of the damped ABH beam with $N_H = 1, 3, 5, 7$, respectively. It can be seen that $N_H = 5$ and 7 lead to basically the same result, demonstrating the convergence of the results. Consequently, $N_H = 5$ is used for nonlinear analyses.

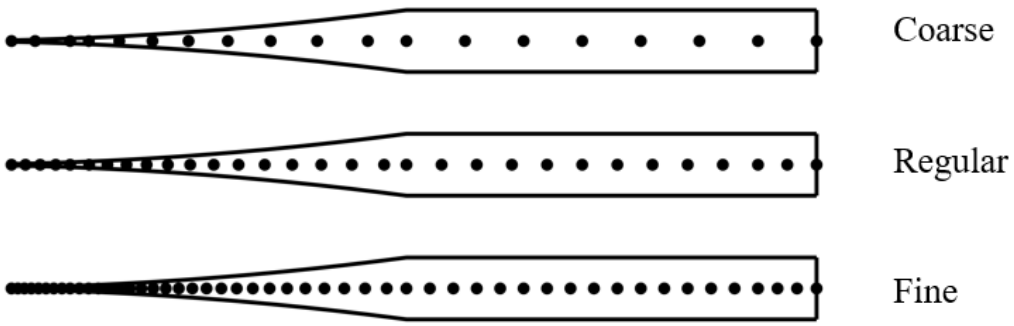

Fig 4.4 Element nodes distribution of 1D beam element in the ABH beam.

Table 4.2 Natural frequencies results calculated from coarse, regular, and fine meshes, respectively.

Mode	**Present** (Hz)		
	Coarse	Regular	Fine
1	30.94	30.94	30.94
2	91.66	91.66	91.66
3	174.46	174.44	174.44
4	288.39	288.31	288.29
5	456.85	456.59	456.54

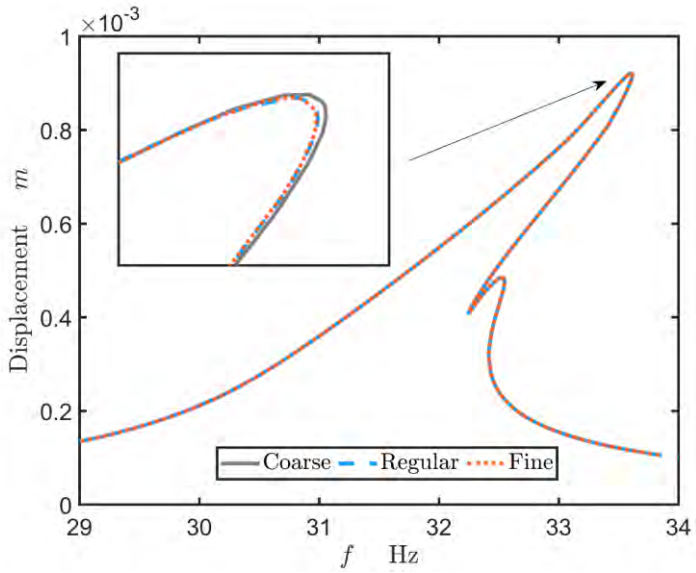

Fig 4.5 NFR curves of the damped ABH beam with different meshes around the first mode with $N_H = 5$, $k_3 = 10^9$ N/m^3 and $F_{ext} = 5$ N.

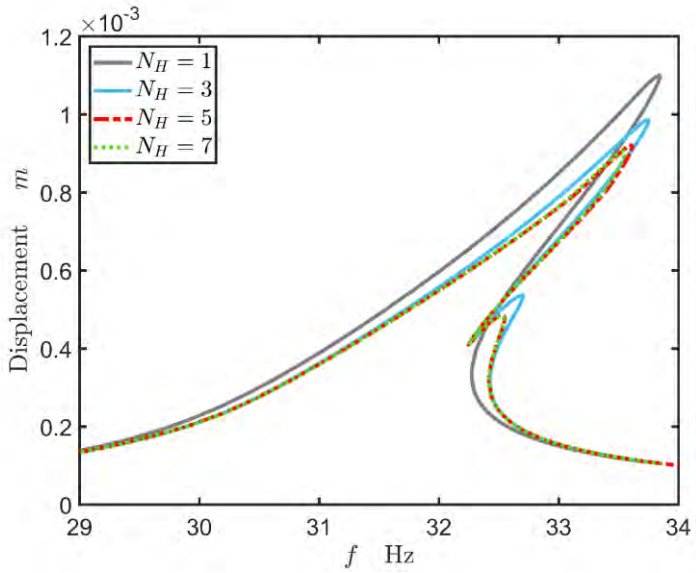

Fig 4.6 NFR curves of the damped ABH beam with different N_H around the first natural frequency with regular mesh, $k_3 = 10^9$ N/m^3 and $F_{ext} = 5$ N.

4.3.2 Linear characteristics of an ABH beam

Linear simulations were first performed in the absence of nonlinear cable. The frequency response functions (FRFs) and mode shapes of the ABH beam with damping layers were calculated by the present coupled model (see Eq.(4.11)) and validated by COMSOL, in which the solid mechanics interface with plane stress assumptions was used. 2911 triangular elements, as shown in Fig 4.7, were employed in the FEM model. It is worth noting that the results of bending-dominated problems can be affected by the interpolation technique of solid elements in the FEM model. Specifically, the linear element subjected to pure bending would produce false shear strain, leading to the well-known “shear locking” phenomenon, which normally causes inaccurate deformation and stress results [131]. High-order interpolation is

recommended to address this issue. To substantiate this point, the natural frequencies of the beam using linear, quadratic, and cubic elements, respectively, are compared in Table 4.3. One can see that, for the first five modes, linear elements result in higher natural frequencies than the quadratic or cubic ones, due to increased stiffness effects. Meanwhile, the quadratic and cubic elements lead to very close and converged results. Therefore, 10-node cubic elements with 20 DOFs are employed in the FEM model to provide reference results.

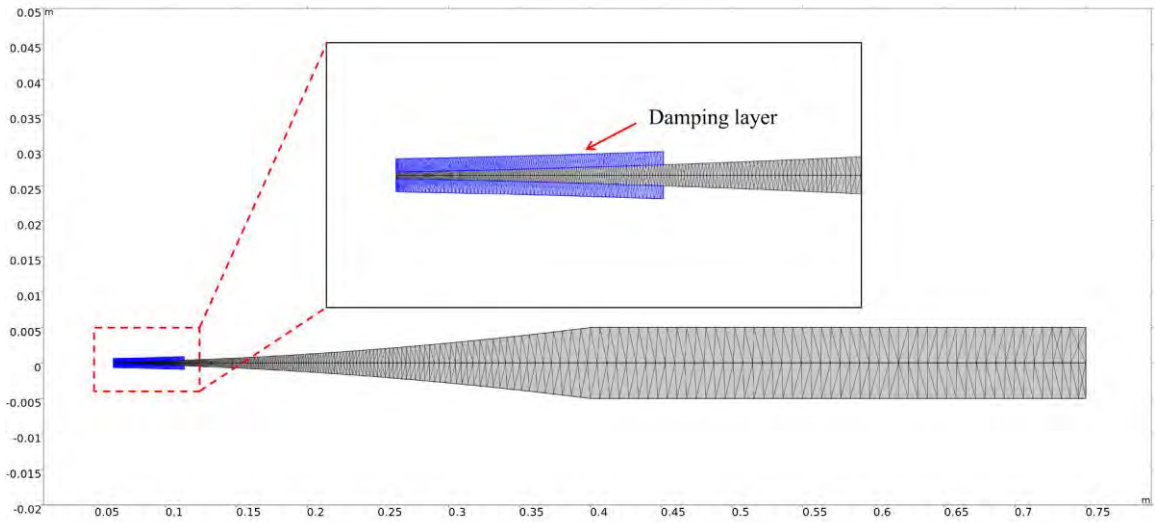

Fig 4.7 Mesh distribution in the FEM model with two damping layers.

Table 4.3 Natural frequencies (Hz) obtained from FEM with elements of different orders.

Modes	Order of element		
	Linear	Quadratic	Cubic
1	41.713	30.939	30.936
2	123.31	91.635	91.632

3	228.31	174.32	174.3
4	381.67	288.01	287.98
5	595.55	456.06	455.97

Fig 4.8 shows the linear FRFs of the ABH beam with the damping layers, at the free end tip $x = x_0$. The results are compared with those of the corresponding uniform beam, which is identical to the damped ABH beam without the reduced thickness. The frequency range on the horizontal axis is from 0 Hz to 2000 Hz with an equal frequency interval of $\Delta f = 1$ Hz . The vertical axis is the cross-point mobility of the free end tip with the external excitation applied at $x = x_f$, which is represented by $20\log_{10}(v/F_{ext})$ dB. It can be seen that the present coupled model shows nice agreements with the FEM model despite the slight deviation of the high frequency resonant frequencies. Compared to the uniform beam, the results show that the ABH beam has a larger response at each mode, especially for lower order modes, due to the reduced stiffness caused by the power-law profile, which can be exploited to generate stronger nonlinear effects. Meanwhile, the ABH beam has a higher modal density, which provides more opportunities for triggering internal resonances for modal energy transfer.

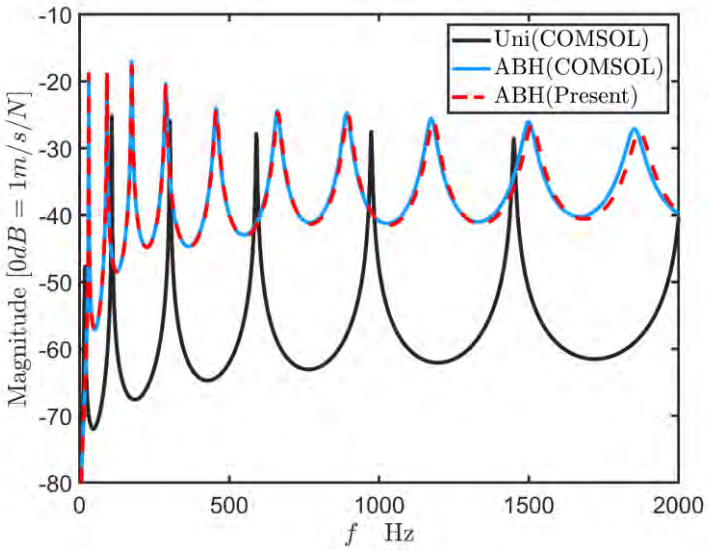

Fig 4.8 Linear FRFs of the uniform beam and the ABH beam at $x = x_0$.

Another ABH-specific feature can be illustrated by examining mode shapes, in which the displacement is normalized by the maximum value at the free end tip and displayed along the arc length of the ABH beam, as depicted in Fig 4.9. Fig 4.9(a)-(d) show that the present model with relatively few elements can capture the local wavelength variations in the ABH portion, which is very close to the FEM model with a refined mesh, even for mode 7. However, there exists a slight deviation near the first trough of this high-order mode, indicating that more elements are required to faithfully represent the local wavelengths of the higher-order modes. Characteristics of mode shapes of the ABH beam are illustrated with the aid of two shadowed zones, where the darker shaded zone I stands for the part covered by the damping layers, and the lighter shaded zone II for the ABH portion. In Fig 4.9(a), mode 1 shows no local deformation in the ABH portion, which rules out the presence of the ABH effect. From Fig 4.9(b)-(d), it can be observed that the incident wave propagates into the ABH portion, and the

wavelength is compressed by the ABH structure. Meanwhile, the deformation in the ABH part is larger than that in the uniform portion, which indicates the existence of energy focusing phenomenon. Therefore, high damping can be achieved by a small amount of damping layers when the locally deformed wave is trapped in the zone I, as shown in Fig 4.9(c)-(d).

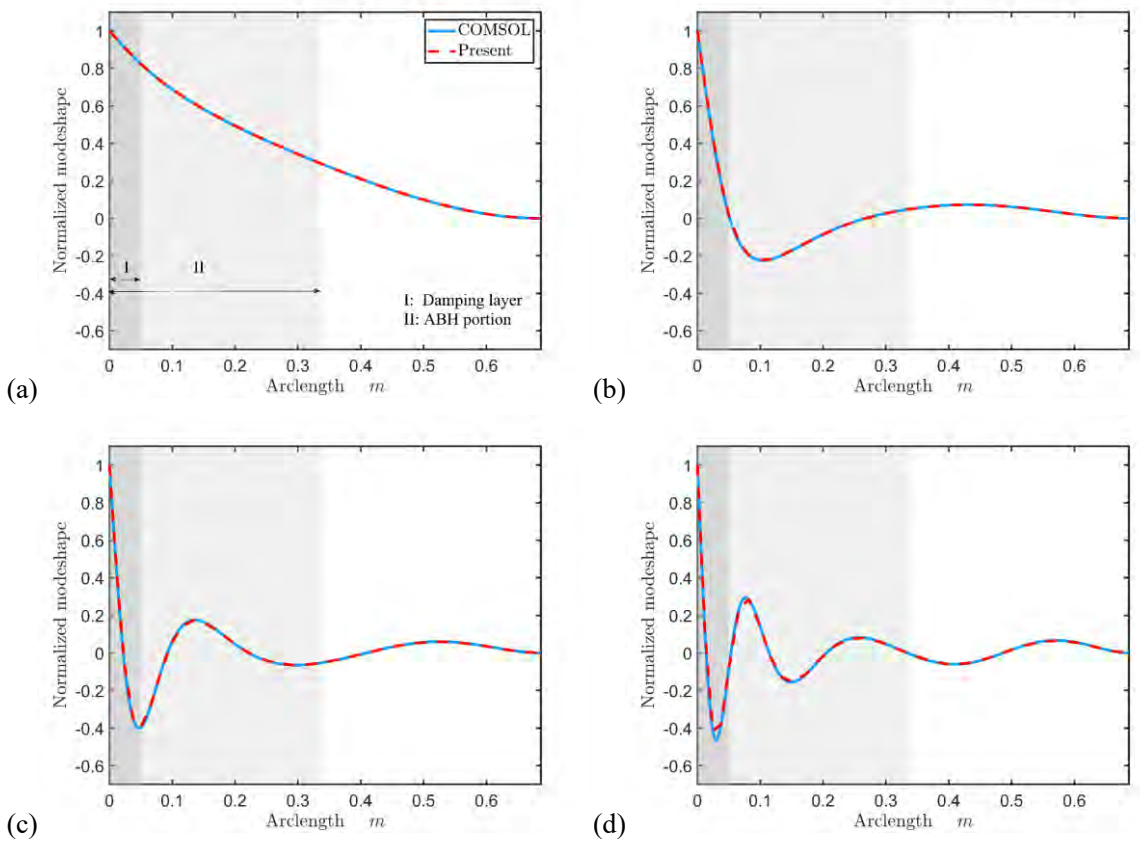

Fig 4.9 Normalized mode shapes with damping layers. (a) Mode 1, (b) Mode 3, (c) Mode 5, (d) Mode 7.

The previously mentioned high damping effect of the ABH in the frequency domain can be quantified by the damping loss factor of the system, denoted by η, as illustrated in Fig 4.10, which can be obtained from Eq.(4.13). The results show that the present model considering the damping layers agrees with the FEM model. Compared to the uniform beam, the ABH beam has a substantially higher damping loss factor, as a result of the ABH effect. Since the

conventional damping assessment method relies on eigenvalues, the resulting indicator can also be referred to as the modal loss factor. However, it is obvious that this method is hardly applicable to nonlinear systems, which require specific treatment. Following Amabili *et al.* [132], the loss factor can also be defined by the energy approach as

$$\eta = \frac{W_c}{2\pi W_{p,\max}}, \tag{4.14}$$

with

$$\begin{aligned} P_c &= \dot{\mathbf{x}}^T \mathbf{C}\dot{\mathbf{x}}, & W_c &= \int_0^T P_c dt \\ P_p &= \dot{\mathbf{x}}^T \left(\mathbf{K}\mathbf{x} + \mathbf{f}_{nl}\right), & W_{p,\max} &= \max_{0\le\tau\le T}\left(\int_0^\tau P_p dt\right) - \min_{0\le\tau\le T}\left(\int_0^\tau P_p dt\right) \end{aligned} \tag{4.15}$$

where P_c, P_p are the power of the damping force and that of the internal force, respectively, and W_c is the work done by the damping force in the period of $T = 2\pi/\omega$, which also represents the dissipated energy, and $W_{p,\max}$ is the maximum storage energy in the system. Apparently, this energy approach can provide a continuous description in the frequency domain, applicable to both linear and nonlinear cases, as long as the power items in Eq.(4.15) can be calculated. Based on the alternating frequency-time (AFT) approach in the HB method, time responses in a period (later validated in Fig 4.14) are provided for the calculation of the power. For the linear system, one harmonic $N_H = 1$ is picked and $N_T = 128$ time points are set in a period to calculate W_c and $W_{p,\max}$ using trapezoidal integration. Depicted by the orange dash-dotted line in Fig 4.10, the result shows that the energy-based approach agrees well with the conventional method for each structural mode. As observed, the loss factor between two adjacent modes does not vary monotonically, but fluctuates (increases, decreases, and increases again). This can be explained from a modal perspective, where multiple modes are excited to

contribute to the loss factor, but not equally, as the excitation frequency moves away from a resonant frequency.

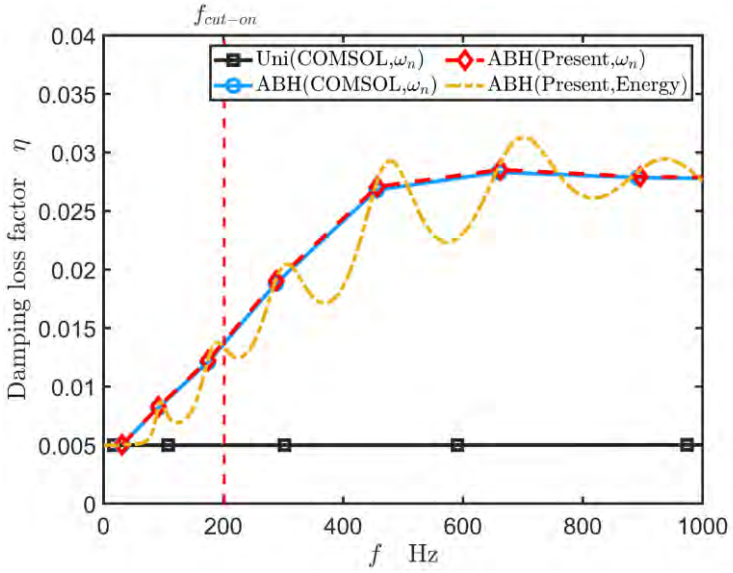

Fig 4.10 Damping loss factors of the uniform beam and the ABH beam.

As expected, the ABH effect mentioned above, reflected by large loss factors, shows a deficiency for the low-order modes, especially below the cut-on frequency (red dashed line in Fig 4.10). This characteristic frequency can be defined by a comparable wavelength $\alpha\lambda$ and ABH length l_{ABH}. By means of the wave velocity $c = \sqrt{\omega}\ EI/\rho A\ ^{\frac{1}{4}}$ of the uniform portion and the wavelength $\lambda = c/f$ [64], the cut-on frequency f_{cut-on} defined by the half wavelength (i.e., $\alpha = 0.5$) is

$$f_{cut-on} = \frac{\pi(2h_u)}{2l_{ABH}^2}\sqrt{\frac{E}{12\rho}} \tag{4.16}$$

where $2h_u$ is the thickness of the uniform portion and $f_{cut-on} = 201.53$ Hz for the current configuration. As discussed in [14], the cut-on frequency f_{cut-on} should be treated as an indicator instead of a strict frequency limit.

4.3.3 Nonlinear dynamic features and enhanced ABH effects

As illustrated above, the linear ABH beam is deficient below the cut-on frequency. However, the energy-based approach suggests that high-order modes could somehow be involved to contribute to the high damping effect, which could be achieved by nonlinearity-induced high-order harmonics. Therefore, the ABH beam with an embedded nonlinear cable is investigated in both time (G-α method) and frequency (Fast Fourier Transform method, FFT for short, or HB method) domains to demonstrate the nonlinear dynamic behavior and the enhanced ABH effects. The nonlinear stiffness of the cable is set to $k_{nl} = 10^9\ \mathrm{N/m^3}$ in Eq.(4.2), to ensure sufficient nonlinearity level in the system. As to be shown in the later experimental section, such stiffness can be readily achieved through a proper cable design. The parameters used in the HB method are $N_H = 5$ and $N_T = 128$. The G-α method selects slight artificial damping to ensure the robustness of the algorithm with $\rho_\infty = 0.99$ ($\rho_\infty = 1$ for no artificial damping) and performs the simulations at a sweeping rate of 15 Hz/min with $f_s = 12.8$ kHz.

4.3.3.1 Systematic enhancement of the ABH effect below f_{cut-on}

Sweeping from 1 Hz to 202 Hz (below f_{cut-on}), the time responses of the linear and nonlinear ABH beams with damping layers were computed for different external excitation

levels of $F_{ext} = 1$ N, 3 N, 5 N and 20 N. The fft function in MATLAB was then used to calculate the frequency responses, as shown in Fig 4.11. The vertical axis shows the displacement of the free end tip of the beam, v, expressed in dB $(20\log_{10} v)$. Fig 4.11 illustrates that all nonlinear resonant frequencies f_{NL} of the ABH beam are shifted to higher frequencies due to the cubic nonlinear stiffness, typical of the well-known hardening phenomenon. More specifically, in the strongly nonlinear case of 20 N, the third nonlinear resonant frequency $f_{NL,3}$ in Fig 4.11(d) reaches the cut-on frequency (vertical dashed line), which is much greater than the linear third resonant frequency. Multiple harmonics of the nonlinear frequency $f_{NL,1}$ can be observed in Fig 4.11(a)-(b), in particular the third $3f_{NL,1}$ and fifth $5f_{NL,1}$ harmonic components. As seen in Fig 4.11(a), the nonlinearity causes a 2.9 dB reduction in the peak of the first mode compared to the linear system. From Fig 4.11(a) to (d), the system exhibits a stronger nonlinear response, and the nonlinear system leads to enhanced vibration suppression compared to the linear system. The peak drop reaches a maximum of 11.06 dB in Fig 4.11(d). The vibration suppression is also present for the second mode, with an amplitude reduction of 13 dB at 20 N. However, an adverse nonlinear phenomenon occurs for the third mode, where the peak increases with the excitation force, rather than decreasing for the first two modes (Fig 4.11(b)-(c)). This is to be discussed in the later section. Nonetheless, the observed feature changes with the excitation level, as exemplified by the 2.9 dB amplitude reduction found for the third mode in Fig 4.11(d).

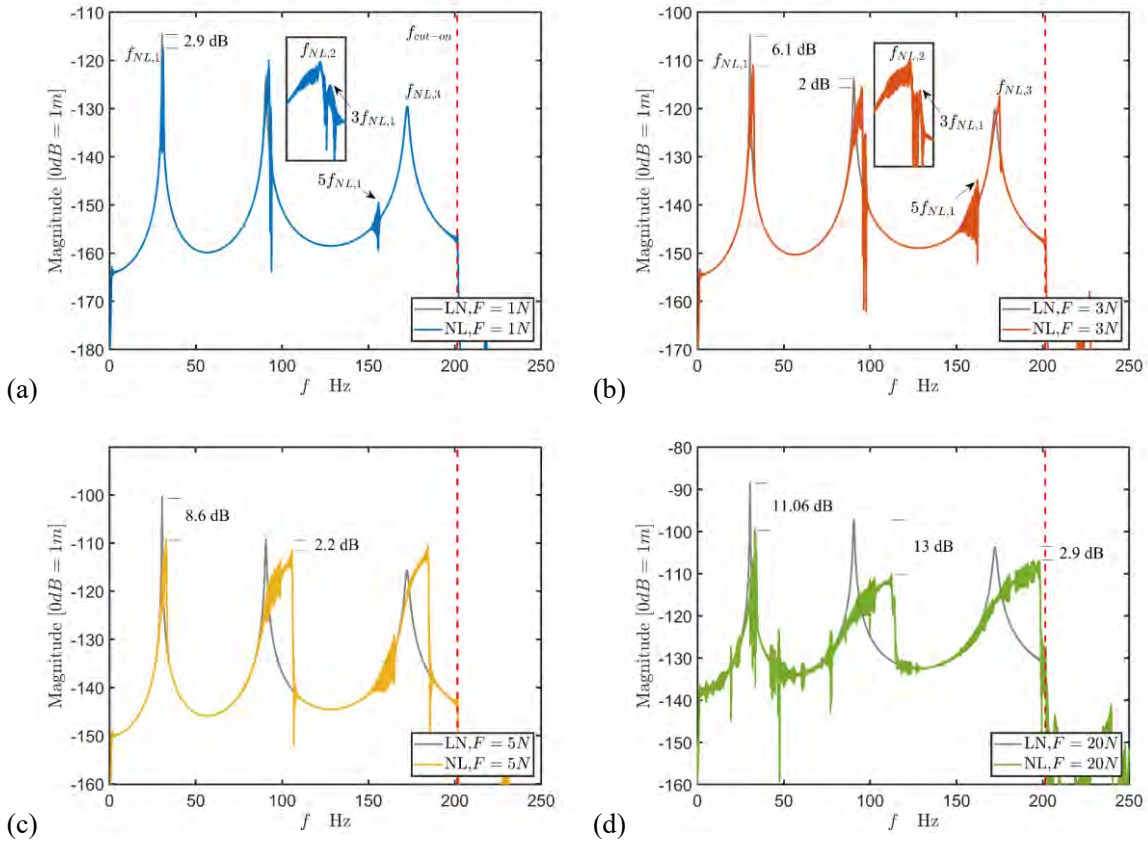

Fig 4.11 FFT results of a sweep below the cut-on frequency for the linear (LN) and nonlinear (NL) damped ABH beams, $F_{ext} = [1\ 3\ 5\ 20]$ N.

Fig 4.12 shows the results of the nonlinear damped ABH beam at higher frequencies. Numerical simulations were performed for nonlinear undamped ($\eta_d = 0$) and damped ($\eta_d = 0.3$) ABH beams with the same procedure as in the previous case. As seen in Fig 4.12(a)-(d), beyond f_{cut-on}, peaks appear at high frequencies and rise with the force level, which is not achievable for the linear system. However, the increase in amplitude at high frequencies decreases due to damping, with some amplitudes dropping by more than 20 dB compared to the undamped state. This demonstrates that nonlinearity transfers the system energy from low to high frequencies, which is, in turn, dissipated by the highly damped ABH feature, resulting

in an enhanced ABH effect at low frequencies. In addition, when the nonlinear effect is sufficiently intense, as in Fig 4.12(d), continuous spectral lines indicate that chaos occurs and almost all modes are excited. The chaotic phenomenon exhibits superior vibration suppression in the low-order modes and more energy is transferred to a higher-frequency range resulting in an improved ABH effect. However, this process is due to an extremely high excitation level, which may pose a threat to the fragile ABH tip and is difficult to control.

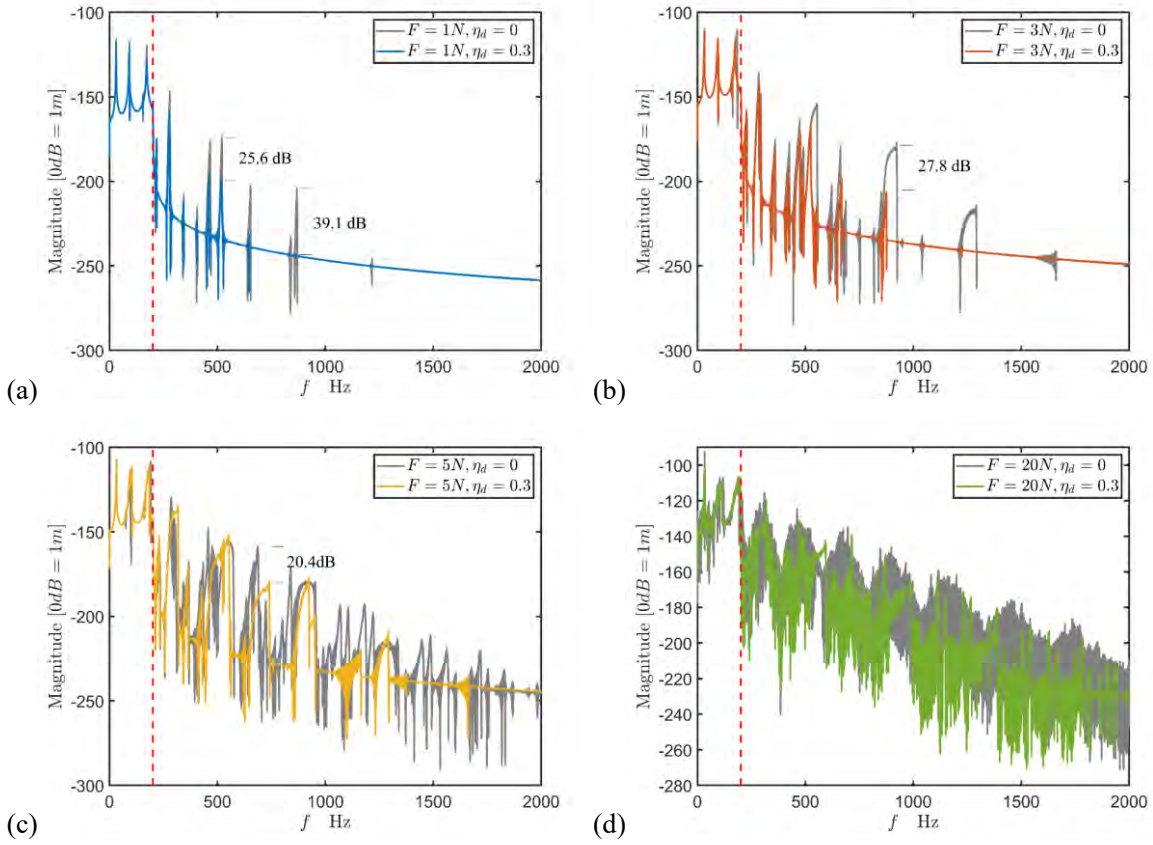

Fig 4.12 FFT results of a sweep for the undamped ($\eta_d = 0$) and damped ($\eta_d = 0.3$) nonlinear ABH beams,

$$F_{ext} = [1\ 3\ 5\ 20]\ \text{N}.$$

4.3.3.2 Quantification of the enhanced ABH effect

Although nonlinearity systematically enhances the ABH effect below the cut-on frequency, the ABH features with nonlinear effects should be quantified. Inspired by the definition of loss factor for the linear system in Eq.(4.14), the same approach is used in the nonlinear case. As a representative harmonic analysis, the normalized third-order harmonic σ_3 indicates the strength of the nonlinearity in the system, as defined by Eq.(2.58) in Section 2.4.2. With the HB method, the damping loss factor η of the nonlinear damped ABH beam for the first mode is shown in Fig 4.13(a). For $F_{ext} = 0.1$ N, the ABH effect is barely visible in the weakly nonlinear system, because of the unchanged value of 0.005 for η (equal to the structural damping loss factor η_b). As the force level increases from $F_{ext} = 0.1$ N to 5 N, the η curve bulges near the first resonant frequency and shows larger amplitude, e.g., $\eta(P_5) = 0.0237$ is 4.74 times greater than $\eta(P_{0.1}) = 0.005$, where P is the peak point on the curve defined as in Fig 4.3. At the same time, large external forces (≥ 1 N) transform the η curves into an L-shaped form, similar to the third harmonic σ_3 in Fig 4.13(b). This similarity in curve shapes clearly evidences the relationship between η and σ_3. Note that the peak points in η and σ_3 curves also correspond in the frequency domain. Indeed, as can be observed in Fig 4.13(a)-(b), the maximum of the η curve plotted in Fig 4.13(a) also represents the maximum of the σ_3 curve. Also note the calculation is based on the same method used for linear system defined in Eq.(4.14). The observed L-shape variation is a result of the drastic drop of the loss factor after reaching the maximum damping values, corresponding to the third harmonics. The increased η thus mainly originates from the third harmonic σ_3, and the ABH effect on the first mode is

then indirectly imposed by high-order harmonics.

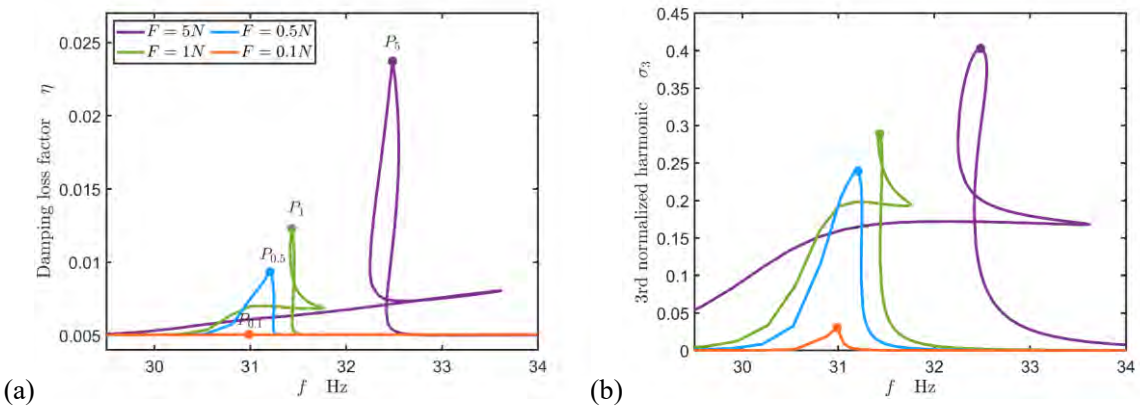

Fig 4.13 (a) Damping loss factor, and (b) the third normalized harmonic close to the first mode. Dot ● in (a) represents the maximum on the curve, and the point with same sequence in (b).

To further substantiate the effect of the increased η and that of the enhanced ABH, free decay analyses are performed. To this end, the initial conditions to trigger the system response corresponding to a targeted point $\eta(P)$ should be determined. For example, for the point $\eta(P_{0.1})$ with $F_{ext} = 0.1\ N,\ f = 31$ Hz, Fig 4.14 shows the steady-state time responses of the normalized displacement, velocity, and acceleration in a period. One observes a good agreement between the G-α and HB methods. The initial values used for the free decay calculation corresponding to $\eta(P_{0.1})$ are the values marked by dots. Note for some frequencies, multiple solutions might exist (Fig 4.13). Therefore, time domain (G-α) method can hardly determine the initial conditions corresponding to a particular point, e.g. $\eta(P_5)$ in Fig 4.13(a). This, however, can be readily done by the HB method with the above procedure.

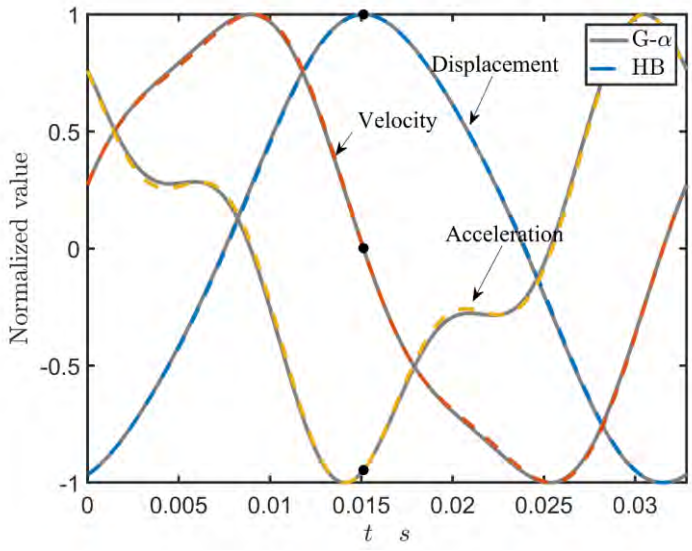

Fig 4.14 Normalized time-domain system responses with $F_{ext} = 0.1$ N, $f = 31$ Hz (frequency at highest point in Fig 4.13(a)). Dot ● on the displacement curve represents the maximum value during a period, and the other two points on velocity and acceleration curves are the corresponding values at the same time.

Free decay tests are carried out using the G-α method with $f_s = 12.8$ kHz for a duration of 5 seconds. Fig 4.15 illustrates the results for $[P_{0.1}, P_1, P_5]$, which are normalized by the initial values. Fig 4.15(a) shows that the greater value of η leads to a faster decay rate of the displacement. Meanwhile, the acceleration results in Fig 4.15(c) show that the higher order harmonics attenuate more quickly, and this behavior is particularly evident up to 0.5 seconds, as further confirmed by the corresponding spectrograms Fig 4.15(b) and (d). On the other hand, according to the time responses, the energy decay curves are calculated. For the linear case, the solution of a single DOF system $x + 2\xi\omega_n x + \omega_n^2 x = 0$ is $x = A(t)cos\omega_n t$, whose amplitude is enveloped by $A(t) = ae^{-\xi\omega_n t}$ [133]. Therefore, the total energy can be expressed in terms of the maximum potential energy, which gives

$$E(t)=\frac{1}{2}kA^2=\frac{1}{2}ka^2e^{-\eta\omega_n t}, \tag{4.17}$$

with $\eta=2\xi$. The total energy of a multi-DOF system with cubic nonlinearity can be numerically calculated at each point in time according to

$$E(t)=\frac{1}{2}\dot{\mathbf{x}}^T\mathbf{M}\dot{\mathbf{x}}+\frac{1}{2}\mathbf{x}^T\mathbf{K}\mathbf{x}+\frac{1}{4}\mathbf{x}^T\mathbf{f}_{nl}. \tag{4.18}$$

For the linear analytical solution of the first mode, a value of 0.005 for η is used in Eq.(4.17). Both the results of the linear and nonlinear normalized energies, hereafter denoted E, are presented in logarithmic form in Fig 4.16. The energy decay curves of the weakly nonlinear and linear systems are straight, due to the fact that the slope in the line function $\ln E(t)=-\eta\omega_n t$ is constant and depends only on η and ω_n of the linear system, and that the comparison of the two different systems confirms the numerical approach in Eq.(4.18). As nonlinearity increases, Fig 4.16 shows that the energy dissipates rapidly, as evidenced by the fact that the energy loss (i.e., $1-E$) in the linear system is 0.6260 at $t=1\ s$, while it is increased by 34.1% to 0.8395 in the nonlinear system (P_5). Meanwhile, the energy decay curve presents a particular phenomenon over time. Specifically, the P_1 and P_5 results exhibit fast decay curves with a steep slope until 0.5 seconds, which slow down with increasing time and eventually become parallel to the curve of the linear system after 1.5 seconds. These results indicate that the energy of the high-order harmonics dissipates rapidly in the beginning, but as the response decreases, the nonlinearity diminishes, and the system begins to behave linearly.

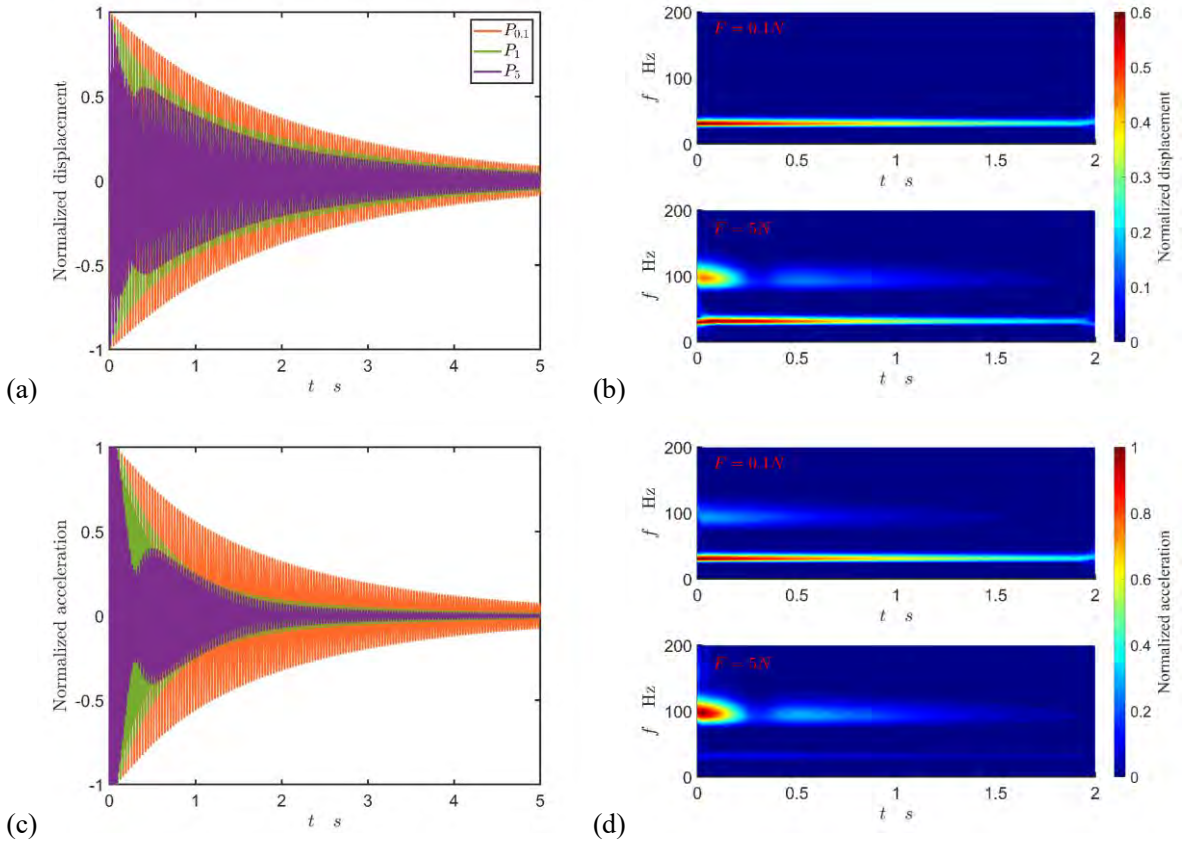

Fig 4.15 Free decay curves and spectrograms for the first mode. (a)-(b): normalized displacement, (c)-(d): normalized acceleration.

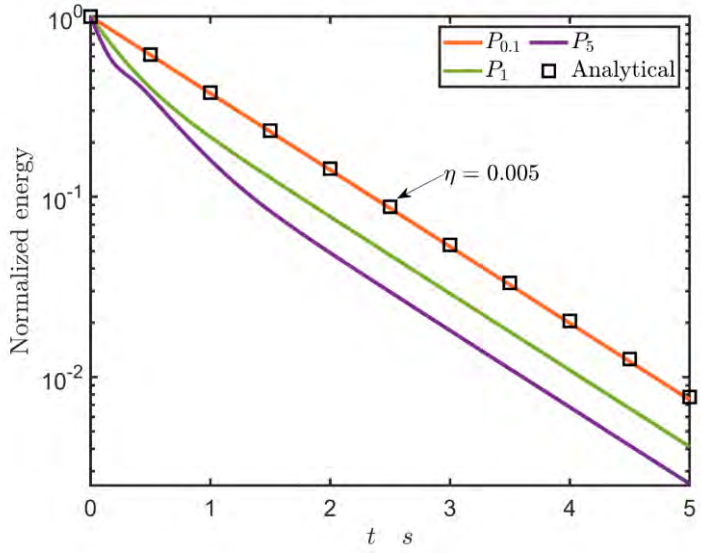

Fig 4.16 Free decay curves of normalized energy for the first mode.

To investigate what happens to other modes, the foregoing procedures are applied to the second mode and the corresponding results are depicted in Fig 4.17. In Fig 4.17(a) and (b), despite some fluctuations, the damping loss factor of the second mode becomes greater as the excitation level rises and is greatly influenced by the third harmonic, which is the main reason for the improved ABH effect. In Fig 4.17(c)-(d), the second mode shows a rapid decay of the acceleration curves with stronger nonlinearity. At time $t = 1\ s$, the energy loss of the P_5 curve is enhanced from 0.8395 (the first mode) to 0.9944 (the second mode), an increase of 18.45%, which indicates the presence of higher-order harmonics for the second mode.

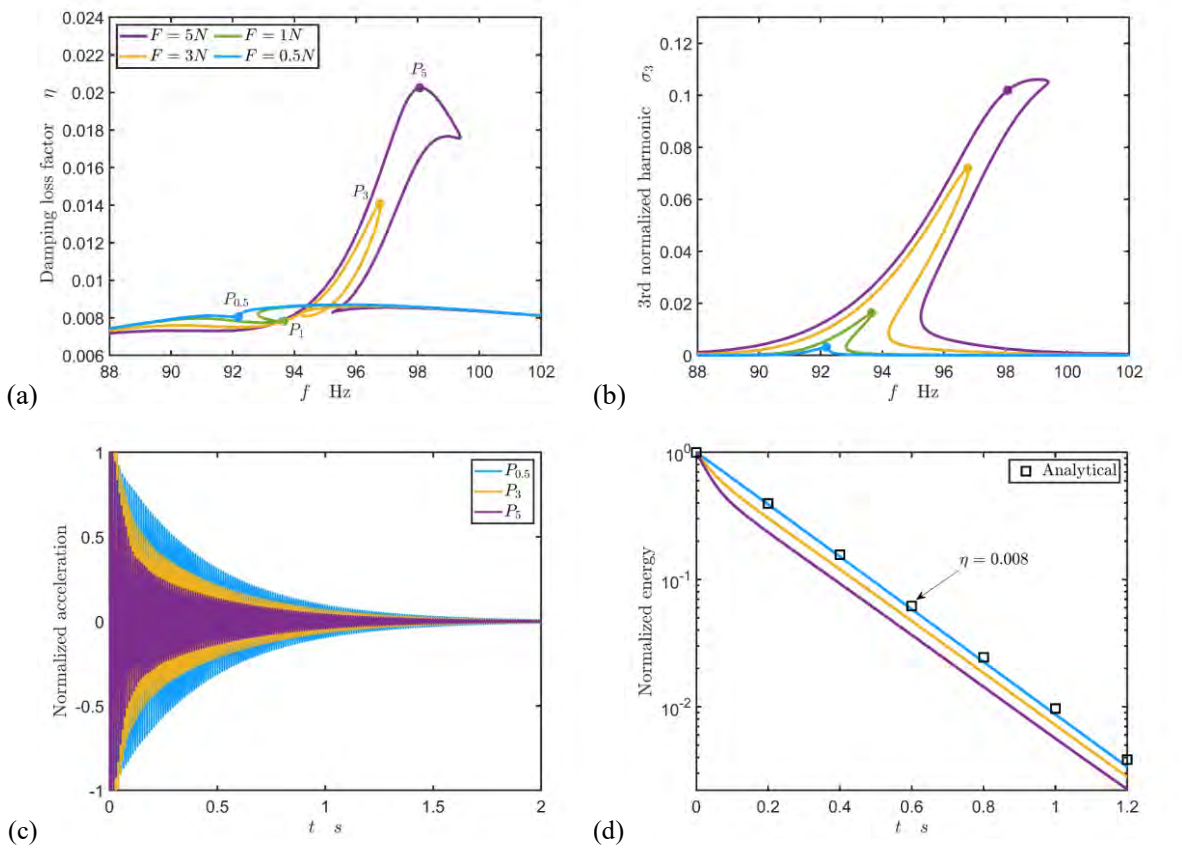

Fig 4.17 (a) Damping loss factor around the second mode, and (b) the third normalized harmonic. Free decay curves: (c) Normalized acceleration, (d) normalized energy.

In Fig 4.18, the overall enhanced ABH effect is illustrated by the damping loss factor for the linear and nonlinear systems for $F_{ext} = 5$ N. At low frequencies, e.g., around the first and second modes, the ABH effect is amplified by the nonlinearity, which has little effect on the system beyond the cut-on frequency. Therefore, the nonlinear damped ABH beam provides an effective solution to enhance the ABH effect. It is noteworthy that η decreases near the third mode, which supports the observation made in Fig 4.11(b)-(c).

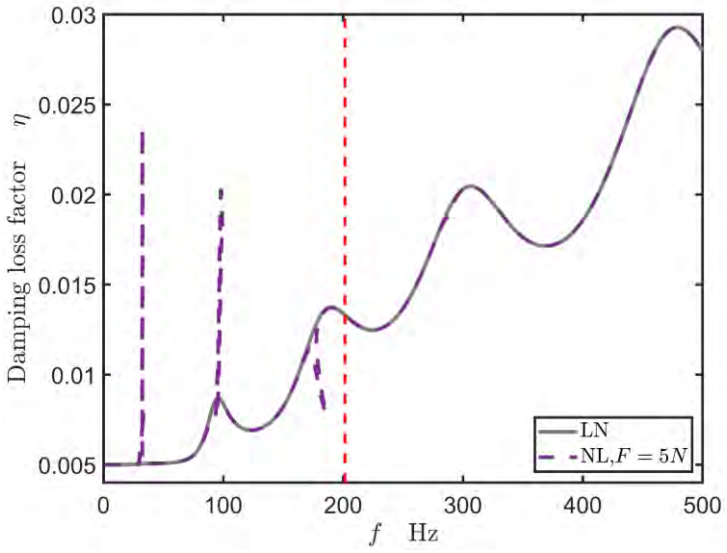

Fig 4.18 Damping loss factors of the linear and nonlinear systems for $F_{ext} = 5$ N.

The observed variations in modal damping for the first three modes, as well as that of the vibration amplitudes, are further scrutinized from the perspective of energy distribution in ABH beam. To this end, the ratio of the potential energy (PE) of the ABH beam part covered by the damping layers (from x_{d1} to x_{d2} but $\eta_d = 0$) to the PE of the rest of the beam, i.e., $\Gamma_{PE} = 10log\ (W_{PE,DP}/W_{PE,rest})$, is calculated to quantify the energy distribution in the beam. The

reason for choosing potential energy for analyses is due to its close link with the deformation of the structure, especially that of the damping layer, which is the main source of energy dissipation. As shown in Fig 4.19, as the excitation frequency increases, the curve corresponding to the linear case shows generally increasing energy concentration in the ABH part of the beam where damping layers are installed. Increasing nonlinearities in the system, however, alter the energy distribution in the beam, more significantly around resonance frequencies. For the first two modes, strong nonlinearities with a high excitation level favor the energy concentration in the damped ABH portion, thus conducive to energy dissipation by the damping layers. This is consistent with the analyses made above in terms of damping loss (Fig 4.18) and vibration amplitude (Fig 4.11). However, Fig 4.19 also shows that less energy is trapped to the damping layer part with increasing forcing level for the 3rd mode. This phenomenon, though not quite common, is similar to the one reported in our previous work on a linear ABH beam without damping layers [134]. In fact, unlike the idealized infinite ABH tapers that were widely used in the literature to discuss wave propagation, finite ABH beams with realistic boundaries might localize the flexural wave energy within a specific beam portion. This obviously depends on the system setting and parameters. More specifically, the case investigated in [134] is due to the discontinuity created by the excitation force. As a result, energy localization occurs between the excitation point and the boundary at specific frequencies so that very little energy would reach the ABH section. The phenomenon was referred to as ABH loss effect [134]. The situation can be changed by changing system parameters. In the present case, similar phenomenon appears for the third mode, which can be

alleviated, for example, by adjusting the position of the grounded cable. In the present case, with the ground cable installed at the ABH tip ($x = 63$ mm), energy is mainly distributed outside the damped area around the 3rd mode, thus affecting energy dissipation by the damping layers. By relocating the grounded cable a bit away from the tip at ($x = 87$ mm), Fig 4.20 displays the damping loss factor ($F = 40$ N) of the system. It can be seen that all three dominant modes below the cut-on frequency (including the previously deficient 3rd mode in Fig 4.18) now show increased damping loss factors, thus ensuring effective energy transfer to higher frequencies like analyzed previously.

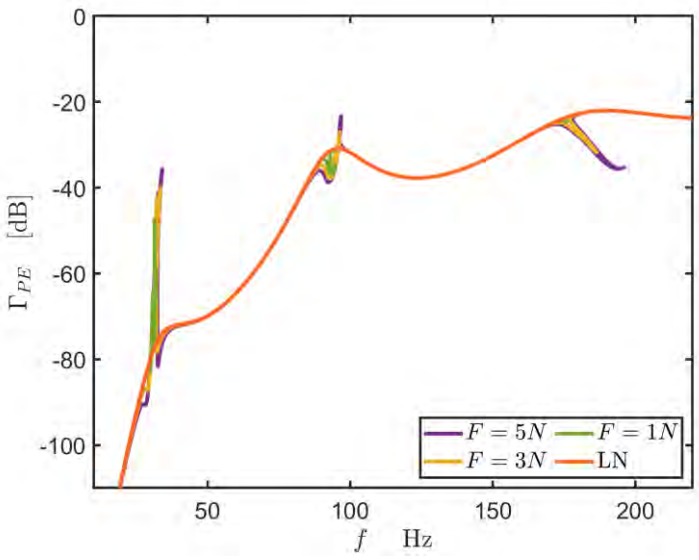

Fig 4.19 Γ_{PE} of the nonlinear system with the grounded cable at the ABH tip and $\eta_d = 0$.

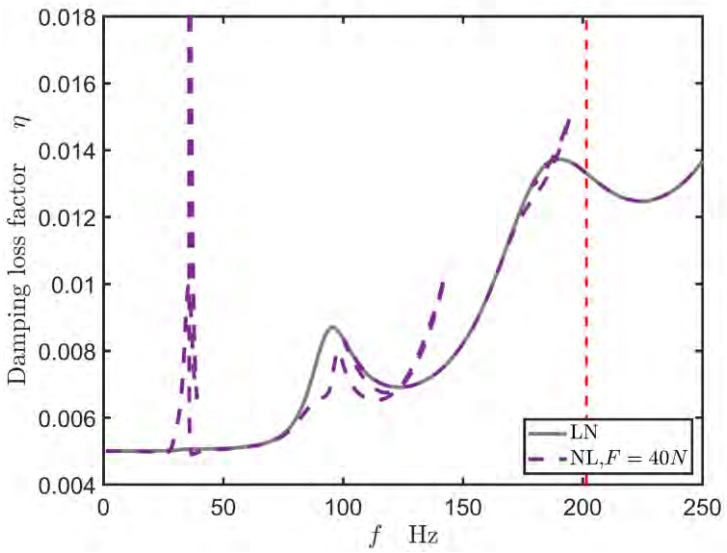

Fig 4.20 Damping loss factors of the nonlinear system with the grounded cable at $x = 87$ mm.

4.4 Experimental confirmation

Experiments were designed and carried out. The purpose is to confirm the energy transfer phenomenon and the enhanced ABH effect in the cable constrained nonlinear ABH beam, instead of validating the simulation model. The experimental configuration and setup are shown in Fig 4.21. The uniform portion of the ABH beam was clamped in a bench vice and excited by an electrodynamic shaker (TIRA TV51075). The impedance head (DYTRAN 5860B) was connected to the shaker by a nylon stinger and was glued to the ABH beam to transmit the force signal. The single metallic cable was secured by a 3D-printed rigid plastic structure that was bolted to a vibration isolation table. The laser vibrometer (Polytec NLV-2500-5) measured the velocity of the beam surface. The Simcenter Testlab software with multiple input/output (MIMO) generated excitation signals and collected force and velocity signals. The properties

of the ABH beam tested in the experiment are the same as the parameters listed in Table 4.1, except that $x_0 = 83$ mm and $x_f = 600$ mm. Therefore, the current configuration has an ABH length of 317 mm and a cut-on frequency of $f_{cut-on} \approx 228$ Hz (defined by Eq.(4.16)). The steel cable has a circular cross section with a diameter of 0.4 mm. By adjusting the two supports, the cable lengths at the top and bottom are both 40 mm, so the estimated value of the nonlinear stiffness is $k_{nl} = 3.93 \times 10^8$ N/m^3 according to Eq.(4.2). As depicted in Fig 4.21(left), the tapes (3M DT17, black) with a thickness of 0.43 mm and a length of 30 mm were symmetrically adhered to both surfaces of the ABH beam and placed near the end to absorb the vibrational energy.

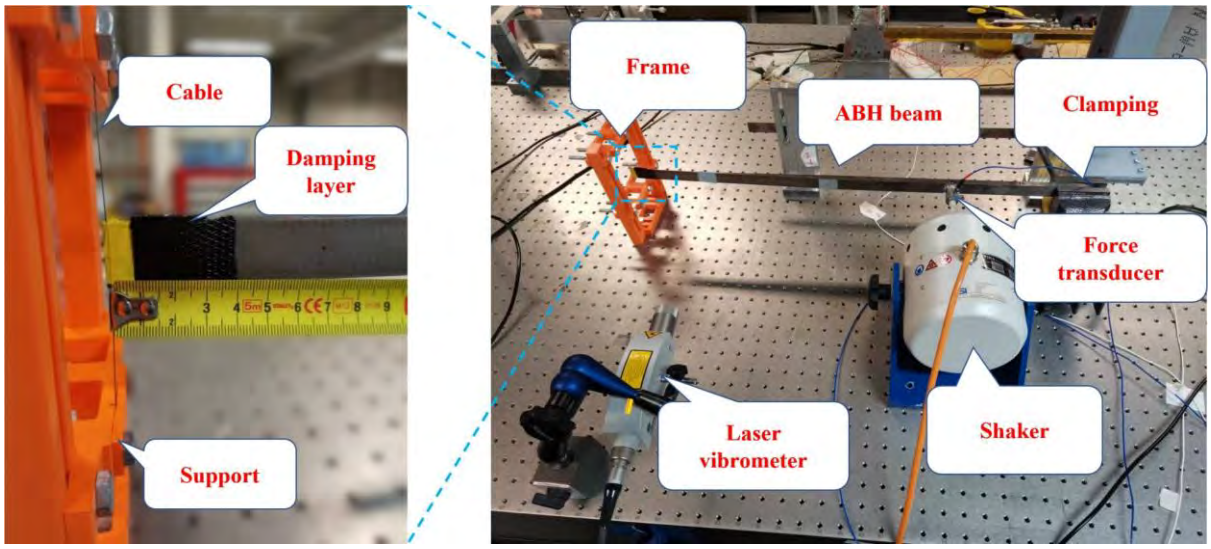

Fig 4.21 Experimental configuration and setup.

The linear FRFs and the coherence of a bare ABH beam at $x = 200$ mm are plotted in Fig 4.22, and the resonant frequencies of the first five modes are listed in Table 4.4. The frequency band is capped at 450 Hz with a resolution frequency $\Delta f = 0.39$ Hz. A periodic chirp wave was exploited for the FRF test, and the average results over 40 times were realized

to mitigate the transient behavior. The amplitude is plotted in Fig 4.22(a). Except for the region close to the resonant frequencies, the coherence in Fig 4.22(b) presents 1. The five dominant resonant frequencies are marked in the diagram. The remaining small peaks are disregarded. The cut-on frequency of the tested ABH beam is a bit lower than the fourth resonant frequency but greater than the first three modes.

Table 4.4 Resonant frequencies of the experimental setup without the damping layers and the cable.

Mode	1	2	3	4	5
f Hz	33.2	91	157	226.6	346.5

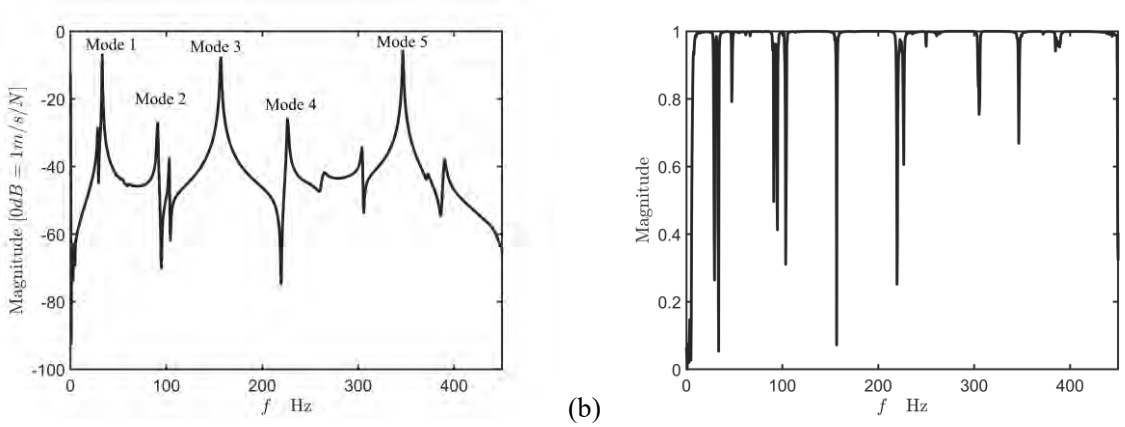

(a) (b)

Fig 4.22 Experimentally measured displacement at $x = 200$ mm of a bare ABH beam without the cable. (a) FRF, (b) coherence.

Sweeping tests were performed to demonstrate the enhanced ABH effect below f_{cut-on} with intentional nonlinearity. The excitation frequency varied from 25 Hz to 228 Hz at a rate of 1 Hz/s, with a sampling frequency of 12.8 kHz. The cable constrained ABH beam without

damping layers was excited by three different voltage levels, i.e., $U = [0.01\ 0.03\ 0.1]V$. Frequency results are given via FFT in Fig 4.23(a). The high excitation levels produce important responses over a wide range of frequencies. For the third mode, the amplitude increases by 8.7 dB and 9.3 dB for $U = 0.01 \rightarrow 0.03\ V$ and $U = 0.03 \rightarrow 0.1\ V$, respectively. However, the amplitude drops dramatically beyond f_{cut-on} (red dashed line), which is consistent with the frequency content of the input signal. Therefore, the response higher than f_{cut-on} is induced by nonlinearity which transfers energy from low to high frequencies. This effect is amplified by the excitation level. More specifically, near 300 Hz, the amplitude increases by 16.3 dB from $U = 0.01\ V$ to $0.03\ V$ and by 18.3 dB from $U = 0.03\ V$ to $0.1\ V$. Similar phenomena can be observed at higher frequencies around 370 Hz, 450 Hz, and 520 Hz, but this phenomenon diminishes as the frequency increases. This suggests that efficient energy transfer occurs near excitation frequencies, and that energy can be transferred to higher-frequency ranges.

For $U = 0.1\ V$, the results of the damping effect are shown in Fig 4.23(b). 0d, 1d, and 2d in the legend stand for no damping layer, one, and two damping layers on both sides of the beam, respectively. The second resonant frequency is noticeably lower due to the additional damping. In contrast, the other two modes exhibit little variation. It is worth noting that the damping layers have a limited influence on vibration suppression of any mode below f_{cut-on}, which exhibits the deficiency of the ABH beam at low frequencies. Above f_{cut-on}, however, it shows a significant peak reduction near 300 Hz. Compared to the result without damping

layer (0d), one damping layer (1d) reduces the peak by 9.7 dB, while two damping layers (2d) reduce the peak further by 9.9 dB. In addition, a reduction in amplitude can be observed at higher frequencies, e.g., 10.56 dB at 450 Hz and 13.36 dB at 520 Hz. Nevertheless, the damping effect decreases with increasing frequency due to limited energy transfer at high frequencies.

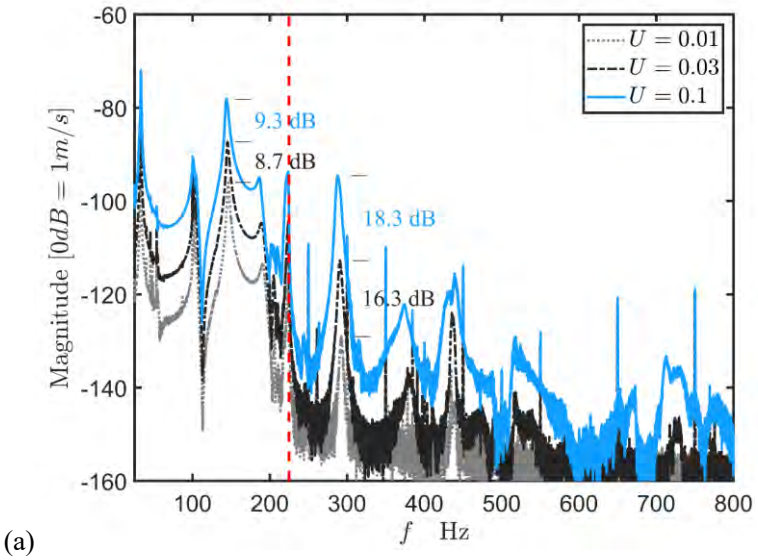

(a)

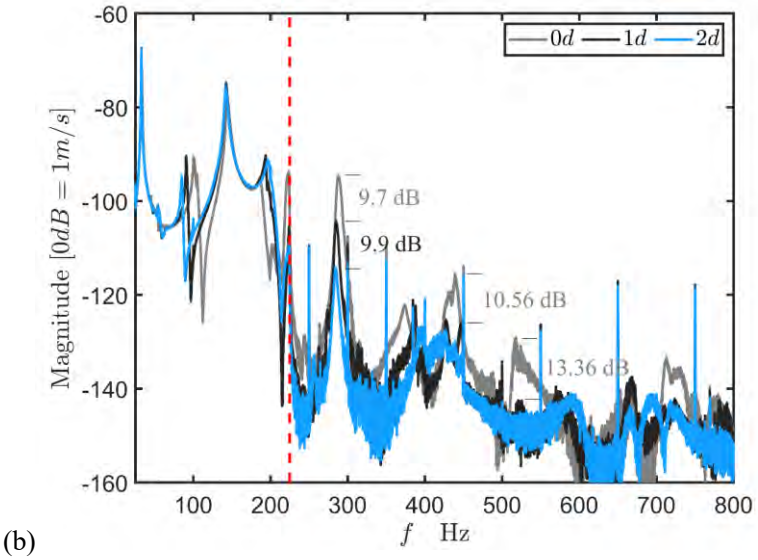

(b)

Fig 4.23 Measured velocity (sweep below the cut-on frequency) of the nonlinear ABH beam with the cable. (a). Different excitation voltages without damping layers, (b) multiple damping layers with $U = 0.1\ V$.

4.5 Summary

In this Chapter, a cantilever ABH beam connected to a grounded cubic stiffness cable was studied. Based on the Euler-Bernoulli assumptions, a coupled model with partial viscoelastic coating was established by considering the grounded nonlinear cable through the Lagrangian equation. The numerical method used in this paper was first validated by COMSOL using the linear FRFs and mode shapes. The typical ABH effect in the linear system was illustrated by the damping loss factor η. Since the eigenvalue approach is inapplicable to the nonlinear system, an energy-based method was adopted and validated for damping evaluation.

The systematic enhancement of the ABH effect at the low frequency range was shown by sweeping analysis below the cut-on frequency. It is shown that intentional nonlinearity attenuates the vibration amplitude below the frequency limit, and transfers energy from low to high frequencies, where the transferred energy is subsequently efficiently dissipated by the ABH damping effect. Moreover, this enhancement of the ABH effect could be quantified by the damping loss factor, which was computed by the HB method in the frequency domain. As the external force increases, large third harmonic is triggered, leading to an increase in the damping loss factor of most dominant lower-order modes. Free decay tests show that the energy loss of higher order harmonics is rapid.

Finally, the energy transfer phenomenon and the enhanced ABH effect are confirmed by experiments. By sweeping below the cut-on frequency, the experimental results illustrate the

significant energy transfer phenomenon at a high excitation level and the exceptional vibration suppression beyond the frequency limit due to the ABH damping effect. Overall, the numerical and experimental results demonstrate a simple and effective method to enhance the ABH effect at low frequencies by introducing the intentional mechanical nonlinearity, thereby paving the way for extending the application of the ABH structure to the low frequency range.

Chapter 5. Conclusions and Future Work

5.1 Conclusions

With the ever-increasing demand for efficient vibration/noise control, the development and conceptualization of novel structures have been a major concern of the vibration and noise control community. In this regard, emerging techniques based on ABH principles with light weight and high damping features provide a feasible solution and have attracted grooming interests in recent years. Despite the promise that the ABH-featured structures hold, the ABH effect shows a deficiency at low frequencies below the so-called cut on frequency, which hinders the practical application of ABH structures in the low-frequency range. Considerable efforts are needed to achieve broadband ABH effects to push the ABH-based technology up to a practical level.

In addition to other techniques discussed in the literature, a straightforward way of achieving the above objective is to enlarge the effective ABH dimensions, but at the expense of generating two troublesome issues, i.e., geometric nonlinearities and imperfections (an initially curved configuration with fragile part where manufacturing accuracy is difficult to guarantee). This may affect the expected ABH effects. Meanwhile the issue is scientifically relevant in terms of developing necessary analysis tools and understanding the underlying physical mechanisms, since these problems also challenge numerical modeling, simulation techniques and physical insights. Therefore, from a scientific perspective, the first part of this

thesis (Chapter 2) focuses on developing an inextensible model with initial curvature. Specific techniques are proposed to numerically implement the developed model with increased accuracy and robustness. Then, the proposed model is used to examine the geometric nonlinearities of ABH beams with imperfect geometry in Chapter 3. To efficiently enhance the ABH effect within reasonable structure size, intentional mechanical nonlinearity is implemented through a grounded cable with cubic stiffness, investigated in Chapter 4. The major conclusions of this work are summarized as follows.

(1) In this part of the thesis, an inextensible condensation model with the consideration of initial curvature is established by combining a geometrically exact model and the shortening effect. The proposed model explicitly shows different nonlinear stiffness and inertia terms arising from the initial curvature, as well as their interplay in the system equation. The HB method is modified to address nonlinear inertia. Meanwhile, an OS technique is adopted and integrated into the generalized-α method for the calculation of time domain system responses.

(2) For a uniform cantilever beam, initial curvature and curved arclength both lead to a decrease in the resonance frequencies, more obvious when the beam is severely bent. Confirmed by the time-domain results from the generalized-α method, nonlinear frequency responses of the first mode are shown to experience a hardening-softening transition with the increasing initial curvature, which indicates the significance of initial curvature and inertia-induced features.

(3) By exploiting the developed model in Chapter 2, perfect or imperfect ABH beams with geometric nonlinearities are examined in Chapter 3. For a perfect ABH beam, the nonlinear inertia effects generally reduce as compared with a uniform beam due to the decreasing ABH thickness profile, thus resulting an amplified hardening effects in the structural modes. Specifically, the first two modes exhibit hardening for the current ABH beam. Meanwhile, the initial curvature of the ABH beams, combined with the nonlinear stiffness effects, generally enhances the hardening tendency in the system, which is significantly different from the uniform beam. However, the effect of initial curvature is limited to both linear and nonlinear results. By intentionally introducing a platform of uniform thickness at the tip of the beam, both linear and nonlinear simulation results change dramatically as the length of platform increases. As the platform length increases from 0 to 0.036, the second mode of the imperfect ABH beam exhibits a transition from hardening to softening, resulting from the increased nonlinear inertia effect induced by the platform. The platform-induced softening behavior in the second mode is confirmed by nonlinear experiments.

(4) Experiments show that geometric nonlinearity can transfer energy from low to high frequencies. However, the effect of geometric nonlinearity is limited.

(5) To enhance the energy transfer and achieve more appreciable ABH effects, Chapter 4 introduces mechanical nonlinearity and establishes a coupled model with partial viscoelastic

coating. The proposed model based on the Euler-Bernoulli assumptions considers the grounded nonlinear cable through the Lagrangian equation. The damping loss factor η is used to demonstrate the typical ABH effect in the linear system, and an energy-based method is adopted to illustrate ABH effects in the nonlinear linear system.

(6) A systematic enhancement of the ABH effect at the low frequency range is shown by sweeping analysis below the cut-on frequency. It is shown that intentional nonlinearity attenuates the vibration amplitude below the frequency limit, and transfers energy from low to high frequencies, where the transferred energy is subsequently efficiently dissipated by the ABH damping effect. Moreover, this enhancement of the ABH effect could be quantified by the damping loss factor, which was computed by the HB method in the frequency domain. As the external force increases, large third harmonic is triggered, leading to an increase in the damping loss factor of most dominant lower-order modes. Free decay tests show that the energy loss of higher order harmonics is rapid.

(7) The intentional nonlinearity-induced energy transfer phenomenon and the enhanced ABH effect are confirmed by experiments. By sweeping below the cut-on frequency, experimental results illustrate the significant energy transfer phenomenon at a high excitation level and the exceptional vibration suppression beyond the frequency limit due to the ABH damping effect.

5.2 Suggestions for future research

This thesis mainly focuses on the investigation of ABH beams with geometric and mechanical nonlinearity through theoretical, numerical, and experimental studies. Hopefully, the research findings provide inspiration for further exploration in future research.

(1) As a general approach, the inextensible condensation model with initial curvature can, in principle, be applied to a wider range of engineering applications. Conventionally, long and large ABH structures take up a lot of space and are therefore difficult to use in real life. In this regard, a spiral ABH beam saves space occupation, and can be further used for vibration absorber and energy harvesting. For such a structure, geometric nonlinearity and initial curvature should be addressed first. Meanwhile, the presently established model involves certain assumptions which may not be directly applied to largely deformed or extremely curved structures. Therefore, future research could focus on extending/improving the proposed model by removing some restrictive assumptions.

(2) Based on the analysis of nonlinear forces and nonlinear inertia, the HB method is modified and applied to inertia-dominant problems. Due to the generic treatments, the modified HB method can accommodate more situations, such as nonlinear damping and material nonlinearity. Moreover, nonlinear normal modes (NNMs) related to nonlinear inertia problems can be efficiently calculated through the HB-based method.

(3) An imperfect ABH beam with a residual platform exhibits strong nonlinearity compared with a perfect ABH beam. Therefore, the extension of the platform could be used to further enhance geometric nonlinearity, thus improving the ABH effect. At the same time, the platform can be clamped and used as a strong nonlinear source to further improve the energy transfer efficiency.

(4) So far, most of the studies on nonlinear ABHs have focused on vibration suppression. There is a lack of appropriate research on energy harvesting using nonlinear ABHs, which could be given more attention.

As a final remark, exploration of the ABH-based technology for concrete engineering application is always a top priority, considering the rapid development of the basic research on ABH at fundamental level. This is no exception with the currently investigated nonlinear based techniques, for which more practical and more efficient ways to trigger the desired system nonlinearities should be exploited.

References

[1] N. Olgac, B.T. Holm-Hansen, A Novel Active Vibration Absorption Technique: Delayed Resonator, Journal of Sound and Vibration, 176 (1994) 93-104.

[2] W. Thomson, Theory of Vibration with Applications, CRC Press, 1993.

[3] A. Pelat, F. Gautier, S.C. Conlon, F. Semperlotti, The acoustic black hole: A review of theory and applications, Journal of Sound and Vibration, 476 (2020) 115316.

[4] V.V. Krylov, Acoustic black holes: recent developments in the theory and applications, IEEE Transactions on Ultrasonics, Ferroelectrics, and Frequency Control, 61 (2014) 1296-1306.

[5] J. Hongli, H. Wei, Q. Jinhao, C. Li, Mechanics problems in application of acoustic black hole structures, Advances in Mechanics, 47 (2017) 333-384.

[6] M.A. Mironov, Propagation of a flexural wave in a plate whose thickness decreases smoothly to zero in a finite interval, Soviet Physics Acoustics-USSR, 34 (1988) 318-319.

[7] V.V. Krylov, Localized acoustic modes of a quadratic solid wedge, Moscow University Physics Bulletin, 45 (1990) 65-69.

[8] V.V. Krylov, F.J.B.S. Tilman, Acoustic 'black holes' for flexural waves as effective vibration dampers, Journal of Sound and Vibration, 274 (2004) 605-619.

[9] V.V. Krylov, On the velocities of localized vibration modes in immersed solid wedges, The Journal of the Acoustical Society of America, 103 (1998) 767-770.

[10] W. Huang, H. Ji, J. Qiu, L. Cheng, Analysis of ray trajectories of flexural waves propagating over generalized acoustic black hole indentations, Journal of Sound and Vibration,

417 (2018) 216-226.

[11] H. Ji, J. Luo, J. Qiu, L. Cheng, Investigations on flexural wave propagation and attenuation in a modified one-dimensional acoustic black hole using a laser excitation technique, Mechanical Systems and Signal Processing, 104 (2018) 19-35.

[12] V.B. Georgiev, J. Cuenca, F. Gautier, L. Simon, V.V. Krylov, Damping of structural vibrations in beams and elliptical plates using the acoustic black hole effect, Journal of Sound and Vibration, 330 (2011) 2497-2508.

[13] L. Tang, L. Cheng, H. Ji, J. Qiu, Characterization of acoustic black hole effect using a one-dimensional fully-coupled and wavelet-decomposed semi-analytical model, Journal of Sound and Vibration, 374 (2016) 172-184.

[14] L. Zhang, G. Kerschen, L. Cheng, Electromechanical Coupling and Energy Conversion in a PZT-Coated Acoustic Black Hole Beam, International Journal of Applied Mechanics, 12 (2020) 2050095.

[15] L. Zhao, S.C. Conlon, F. Semperlotti, Broadband energy harvesting using acoustic black hole structural tailoring, Smart materials and structures, 23 (2014) 065021.

[16] F. Maugan, S. Chesne, M. Monteil, M. Collet, K. Yi, Enhancement of energy harvesting using acoustical-black-hole-inspired wave traps, Smart Materials and Structures, 28 (2019) 075015.

[17] H. Ji, Y. Liang, J. Qiu, L. Cheng, Y. Wu, Enhancement of vibration based energy harvesting using compound acoustic black holes, Mechanical Systems and Signal Processing, 132 (2019) 441-456.

[18] S.C. Conlon, J.B. Fahnline, F. Semperlotti, Numerical analysis of the vibroacoustic properties of plates with embedded grids of acoustic black holes, The Journal of the Acoustical Society of America, 137 (2015) 447-457.

[19] L. Ma, L. Cheng, Sound radiation and transonic boundaries of a plate with an acoustic black hole, The Journal of the Acoustical Society of America, 145 (2019) 164-172.

[20] L. Ma, L. Cheng, Topological optimization of damping layout for minimized sound radiation of an acoustic black hole plate, Journal of Sound and Vibration, 458 (2019) 349-364.

[21] J. Deng, O. Guasch, L. Maxit, N. Gao, Sound radiation and non-negative intensity of a metaplate consisting of an acoustic black hole plus local resonators, Composite Structures, 304 (2023) 116423.

[22] J. Deng, N. Gao, Broadband vibroacoustic reduction for a circular beam coupled with a curved acoustic black hole via nullspace method, International Journal of Mechanical Sciences, 233 (2022) 107641.

[23] H. Ji, X. Wang, J. Qiu, L. Cheng, Y. Wu, C. Zhang, Noise reduction inside a cavity coupled to a flexible plate with embedded 2-D acoustic black holes, Journal of Sound and Vibration, 455 (2019) 324-338.

[24] X. Wang, H. Ji, J. Qiu, L. Cheng, Wavenumber domain analyses of vibro-acoustic decoupling and noise attenuation in a plate-cavity system enclosed by an acoustic black hole plate, The Journal of the Acoustical Society of America, 146 (2019) 72-84.

[25] L. Tang, L. Cheng, Ultrawide band gaps in beams with double-leaf acoustic black hole indentations, The Journal of the Acoustical Society of America, 142 (2017) 2802-2807.

[26] L. Tang, L. Cheng, Broadband locally resonant band gaps in periodic beam structures with embedded acoustic black holes, Journal of Applied Physics, 121 (2017) 194901.

[27] L. Tang, L. Cheng, Periodic plates with tunneled Acoustic-Black-Holes for directional band gap generation, Mechanical Systems and Signal Processing, 133 (2019) 106257.

[28] S. Nair, M. Jokar, F. Semperlotti, Nonlocal acoustic black hole metastructures: Achieving broadband and low frequency passive vibration attenuation, Mechanical Systems and Signal Processing, 169 (2022) 108716.

[29] J. Deng, N. Gao, X. Chen, Ultrawide attenuation bands in gradient metabeams with acoustic black hole pillars, Thin-Walled Structures, 184 (2023) 110459.

[30] L. Ma, S. Zhang, L. Cheng, A 2D Daubechies wavelet model on the vibration of rectangular plates containing strip indentations with a parabolic thickness profile, Journal of Sound and Vibration, 429 (2018) 130-146.

[31] Y. Wang, J. Du, L. Cheng, Power flow and structural intensity analyses of Acoustic Black Hole beams, Mechanical Systems and Signal Processing, 131 (2019) 538-553.

[32] J. Deng, O. Guasch, L. Zheng, A semi-analytical method for characterizing vibrations in circular beams with embedded acoustic black holes, Journal of Sound and Vibration, 476 (2020) 115307.

[33] J. Deng, L. Zheng, P. Zeng, Y. Zuo, O. Guasch, Passive constrained viscoelastic layers to improve the efficiency of truncated acoustic black holes in beams, Mechanical Systems and Signal Processing, 118 (2019) 461-476.

[34] W. Huang, H. Ji, J. Qiu, L. Cheng, Wave Energy Focalization in a Plate With Imperfect

Two-Dimensional Acoustic Black Hole Indentation, Journal of Vibration and Acoustics, 138 (2016).

[35] T. Zhou, L. Tang, H. Ji, J. Qiu, L. Cheng, Dynamic and Static Properties of Double-Layered Compound Acoustic Black Hole Structures, International Journal of Applied Mechanics, 09 (2017) 1750074.

[36] H. Ji, N. Wang, C. Zhang, X. Wang, L. Cheng, J. Qiu, A vibration absorber based on two-dimensional acoustic black holes, Journal of Sound and Vibration, 500 (2021) 116024.

[37] L. Zhao, F. Semperlotti, Embedded Acoustic Black Holes for semi-passive broadband vibration attenuation in thin-walled structures, Journal of Sound and Vibration, 388 (2017) 42-52.

[38] L. Ma, T. Zhou, L. Cheng, Acoustic Black hole effects in Thin-walled structures: Realization and mechanisms, Journal of Sound and Vibration, 525 (2022) 116785.

[39] V. Krylov, Propagation of plate bending waves in the vicinity of one- and two-dimensional acoustic 'black holes', in: Proceedings of the First International ECCOMAS Thematic Conference on Computational Methods in Structural Dynamics and Earthquake Engineering, Rethymno, Crete, Greece, 2007.

[40] O. Aklouche, A. Pelat, S. Maugeais, F. Gautier, Scattering of flexural waves by a pit of quadratic profile inserted in an infinite thin plate, Journal of Sound and Vibration, 375 (2016) 38-52.

[41] V. Kralovic, V. Krylov, Damping of flexural vibrations in tapered rods of power-law profile: Experimental studies. Proc. IOA, 2007, 29(5), 66-73, Proceedings of the Institute of Acoustics,

29 (2007) 66-73.

[42] E.P. Bowyer, V.V. Krylov, Damping of flexural vibrations in turbofan blades using the acoustic black hole effect, Applied Acoustics, 76 (2014) 359-365.

[43] T. Zhou, L. Cheng, A resonant beam damper tailored with Acoustic Black Hole features for broadband vibration reduction, Journal of Sound and Vibration, 430 (2018) 174-184.

[44] T. Zhou, L. Cheng, Planar Swirl-shaped Acoustic Black Hole Absorbers for Multi-directional Vibration Suppression, Journal of Sound and Vibration, 516 (2022) 116500.

[45] S. Park, J.Y. Lee, W. Jeon, Vibration damping of plates using waveguide absorbers based on spiral acoustic black holes, Journal of Sound and Vibration, 521 (2022) 116685.

[46] H. Sheng, M.-X. He, Q. Ding, Vibration suppression by mistuning acoustic black hole dynamic vibration absorbers, Journal of Sound and Vibration, 542 (2023) 117370.

[47] E.P. Bowyer, V.V. Krylov, Experimental study of sound radiation by plates containing circular indentations of power-law profile, Applied Acoustics, 88 (2015) 30-37.

[48] P.A. Feurtado, S.C. Conlon, An Experimental Investigation of Acoustic Black Hole Dynamics at Low, Mid, and High Frequencies, Journal of Vibration and Acoustics, 138 (2016).

[49] X. Li, Q. Ding, Sound radiation of a beam with a wedge-shaped edge embedding acoustic black hole feature, Journal of Sound and Vibration, 439 (2019) 287-299.

[50] P.A. Feurtado, S.C. Conlon, Transmission loss of plates with embedded acoustic black holes, The Journal of the Acoustical Society of America, 142 (2017) 1390-1398.

[51] J. Deng, L. Zheng, Noise reduction via three types of acoustic black holes, Mechanical Systems and Signal Processing, 165 (2022) 108323.

126 [52] E. Bowyer, V. Krylov, A review of experimental investigations into the acoustic black hole
127 effect and its applications for reduction of flexural vibrations and structure-borne sound, in:
128 InterNoise 2015 the 44th International Congress and Exposition on Noise Control Engineering,
129 San Francisco, USA, 2015.
130 [53] M.A. Mironov, V.V. Pislyakov, One-dimensional acoustic waves in retarding structures
131 with propagation velocity tending to zero, Acoustical Physics, 48 (2002) 347-352.
132 [54] X. Zhang, L. Cheng, Broadband and low frequency sound absorption by Sonic black holes
133 with Micro-perforated boundaries, Journal of Sound and Vibration, 512 (2021) 116401.
134 [55] S. Li, J. Xia, X. Yu, X. Zhang, L. Cheng, A sonic black hole structure with perforated
135 boundary for slow wave generation, Journal of Sound and Vibration, 559 (2023) 117781.
136 [56] L. Zhao, S.C. Conlon, F. Semperlotti, An experimental study of vibration based energy
137 harvesting in dynamically tailored structures with embedded acoustic black holes, Smart
138 Materials and Structures, 24 (2015) 065039.
139 [57] H. Li, O. Doaré, C. Touzé, A. Pelat, F. Gautier, Energy harvesting efficiency of unimorph
140 piezoelectric acoustic black hole cantilever shunted by resistive and inductive circuits,
141 International Journal of Solids and Structures, 238 (2022) 111409.
142 [58] Z. Liu, X. Zhang, Y. Mao, Y.Y. Zhu, Z. Yang, C.T. Chan, P. Sheng, Locally Resonant Sonic
143 Materials, Science, 289 (2000) 1734-1736.
144 [59] B. Assouar, B. Liang, Y. Wu, Y. Li, J.-C. Cheng, Y. Jing, Acoustic metasurfaces, Nature
145 Reviews Materials, 3 (2018) 460-472.
146 [60] G. Ma, M. Xiao, C.T. Chan, Topological phases in acoustic and mechanical systems,

147 Nature Reviews Physics, 1 (2019) 281-294.
148 [61] A. Martin, M. Kadic, R. Schittny, T. Bückmann, M. Wegener, Phonon band structures of
149 three-dimensional pentamode metamaterials, Physical Review B, 86 (2012) 155116.
150 [62] C. Sugino, S. Leadenham, M. Ruzzene, A. Erturk, On the mechanism of bandgap
151 formation in locally resonant finite elastic metamaterials, Journal of Applied Physics, 120
152 (2016) 134501.
153 [63] J.Y. Lee, W. Jeon, Wave-based analysis of the cut-on frequency of curved acoustic black
154 holes, Journal of Sound and Vibration, 492 (2021) 115731.
155 [64] L. Tang, L. Cheng, Enhanced Acoustic Black Hole effect in beams with a modified
156 thickness profile and extended platform, Journal of Sound and Vibration, 391 (2017) 116-126.
157 [65] J.Y. Lee, W. Jeon, Vibration damping using a spiral acoustic black hole, The Journal of the
158 Acoustical Society of America, 141 (2017) 1437-1445.
159 [66] J. Deng, O. Guasch, L. Maxit, N. Gao, A metamaterial consisting of an acoustic black hole
160 plate with local resonators for broadband vibration reduction, Journal of Sound and Vibration,
161 526 (2022) 116803.
162 [67] Y. Yu, X.-x. Jia, H. Ouyang, Y. Du, Y. Peng, Dynamic properties investigation of an
163 acoustic black hole beam with dynamic vibration absorber based on analytical method, Journal
164 of Sound and Vibration, 570 (2024) 118053.
165 [68] S. Quaegebeur, G. Raze, L. Cheng, G. Kerschen, A virtual acoustic black hole on a
166 cantilever beam, Journal of Sound and Vibration, 554 (2023) 117697.
167 [69] E.N. Lorenz, Deterministic Nonperiodic Flow, Journal of Atmospheric Sciences, 20 (1963)

130-141.

[70] K. Vorotnikov, Y. Starosvetsky, Nonlinear energy channeling in the two-dimensional, locally resonant, unit-cell model. I. High energy pulsations and routes to energy localization, Chaos, 25 7 (2015) 073106.

[71] A.F. Vakakis, O.V. Gendelman, L.A. Bergman, D.M. McFarland, G. Kerschen, Y.S. Lee, Nonlinear targeted energy transfer in mechanical and structural systems, Springer Science & Business Media, 2008.

[72] D.D. Quinn, A. Triplett, A. Vakakis, L. Bergman, Energy Harvesting From Impulsive Loads Using Intentional Essential Nonlinearities, Journal of Vibration and Acoustics, 133 (2011) 011004.

[73] B. Lossouarn, J. Deü, G. Kerschen, A fully passive nonlinear piezoelectric vibration absorber, Philosophical Transactions of the Royal Society A: Mathematical, Physical and Engineering Sciences, 376 (2018).

[74] K. Asadi, J. Yu, H. Cho, Nonlinear couplings and energy transfers in micro- and nano-mechanical resonators: intermodal coupling, internal resonance and synchronization, Philosophical Transactions of the Royal Society A: Mathematical, Physical and Engineering Sciences, 376 (2018).

[75] A.H. Nayfeh, D.T. Mook, Nonlinear oscillations, John Wiley & Sons, 2008.

[76] A.M. Yu, J.W. Yang, G.H. Nie, X.G. Yang, An improved model for naturally curved and twisted composite beams with closed thin-walled sections, Composite Structures, 93 (2011) 2322-2329.

189 [77] Z. Yi, I. Stanciulescu, Nonlinear normal modes of a shallow arch with elastic constraints
190 for two-to-one internal resonances, Nonlinear Dynamics, 83 (2016) 1577-1600.
191 [78] W. Qiao, T. Guo, H. Kang, Y. Zhao, Softening–hardening transition in nonlinear structures
192 with an initial curvature: a refined asymptotic analysis, Nonlinear Dynamics, 107 (2022) 357-
193 374.
194 [79] H. Ding, L.-Q. Chen, Nonlinear vibration of a slightly curved beam with quasi-zero-
195 stiffness isolators, Nonlinear Dynamics, 95 (2019) 2367-2382.
196 [80] J.E. Lagnese, Boundary stabilization of thin plates, SIAM, 1989.
197 [81] J.E. Lagnese, G. Leugering, Uniform stabilization of a nonlinear beam by nonlinear
198 boundary feedback, Journal of Differential Equations, 91 (1991) 355-388.
199 [82] H. Koch, I. Lasiecka, Hadamard Well-posedness of Weak Solutions in Nonlinear Dynamic
200 Elasticity-full von Karman Systems, in: A. Lorenzi, B. Ruf (Eds.) Evolution Equations,
201 Semigroups and Functional Analysis: In Memory of Brunello Terreni, Birkhäuser Basel, Basel,
202 2002, pp. 197-216.
203 [83] F. Alijani, M. Amabili, Non-linear vibrations of shells: A literature review from 2003 to
204 2013, International Journal of Non-Linear Mechanics, 58 (2014) 233-257.
205 [84] M. Amabili, Nonlinear vibrations and stability of shells and plates, Cambridge University
206 Press, 2008.
207 [85] C. Touzé, A. Vizzaccaro, O. Thomas, Model order reduction methods for geometrically
208 nonlinear structures: a review of nonlinear techniques, Nonlinear Dynamics, 105 (2021) 1141-
209 1190.

[86] G.R. Bhashyam, G. Prathap, Galerkin finite element method for non-linear beam vibrations, Journal of Sound and Vibration, 72 (1980) 191-203.

[87] J. Lee, G. Kerschen, T. Detroux, Harmonic Balance Computation of the Nonlinear Frequency Response of a Thin Plate, (2017).

[88] M. Amabili, Theory and experiments for large-amplitude vibrations of rectangular plates with geometric imperfections, Journal of Sound and Vibration, 291 (2006) 539-565.

[89] C. Touzé, C. Camier, G. Favraud, O. Thomas, Effect of Imperfections and Damping on the Type of Nonlinearity of Circular Plates and Shallow Spherical Shells, Mathematical Problems in Engineering, 2008 (2008) 678307.

[90] W. Lacarbonara, H.N. Arafat, A.H. Nayfeh, Non-linear interactions in imperfect beams at veering, International Journal of Non-Linear Mechanics, 40 (2005) 987-1003.

[91] Z. Yi, L. Wang, H. Kang, G. Tu, Modal interaction activations and nonlinear dynamic response of shallow arch with both ends vertically elastically constrained for two-to-one internal resonance, Journal of Sound and Vibration, 333 (2014) 5511-5524.

[92] M.H. Ghayesh, M. Amabili, Coupled longitudinal-transverse behaviour of a geometrically imperfect microbeam, Composites Part B: Engineering, 60 (2014) 371-377.

[93] A.H. Nayfeh, P.F. Pai, Linear and nonlinear structural mechanics, John Wiley & Sons, 2008.

[94] P.F. Pai, A.H. Nayfeh, A fully nonlinear theory of curved and twisted composite rotor blades accounting for warpings and three-dimensional stress effects, International Journal of Solids and Structures, 31 (1994) 1309-1340.

231 [95] O.A. Bauchau, C.H. Hong, Large displacement analysis of naturally curved and twisted
232 composite beams, AIAA Journal, 25 (1987) 1469-1475.
233 [96] A. Ibrahimbegović, On finite element implementation of geometrically nonlinear
234 Reissner's beam theory: three-dimensional curved beam elements, Computer Methods in
235 Applied Mechanics and Engineering, 122 (1995) 11-26.
236 [97] M.R.M. Crespo da Silva, C.C. Glynn, Nonlinear Flexural-Flexural-Torsional Dynamics
237 of Inextensional Beams. I. Equations of Motion, Journal of Structural Mechanics, 6 (1978)
238 437-448.
239 [98] D. Culver, K. McHugh, E. Dowell, An assessment and extension of geometrically
240 nonlinear beam theories, Mechanical Systems and Signal Processing, 134 (2019) 106340.
241 [99] A.H. Nayfeh, P.F. Pai, Non-linear non-planar parametric responses of an inextensional
242 beam, International Journal of Non-Linear Mechanics, 24 (1989) 139-158.
243 [100] O. Thomas, A. Sénéchal, J.F. Deü, Hardening/softening behavior and reduced order
244 modeling of nonlinear vibrations of rotating cantilever beams, Nonlinear Dynamics, 86 (2016)
245 1293-1318.
246 [101] K. McHugh, E. Dowell, Nonlinear Responses of Inextensible Cantilever and Free–Free
247 Beams Undergoing Large Deflections, Journal of Applied Mechanics, 85 (2018).
248 [102] E. Dowell, K. McHugh, Equations of Motion for an Inextensible Beam Undergoing
249 Large Deflections, Journal of Applied Mechanics, 83 (2016).
250 [103] T.J. Anderson, A.H. Nayfeh, B. Balachandran, Experimental Verification of the
251 Importance of The Nonlinear Curvature in the Response of a Cantilever Beam, Journal of

252 Vibration and Acoustics, 118 (1996) 21-27.
253 [104] A. Kumar, Effect of approximation of curvature/inertia on the nonlinear vibrations of
254 cantilever beam, Structures, 26 (2020) 737-744.
255 [105] H. Farokhi, Y. Xia, A. Erturk, Experimentally validated geometrically exact model for
256 extreme nonlinear motions of cantilevers, Nonlinear Dynamics, 107 (2022) 457-475.
257 [106] M. Amabili, G. Ferrari, M.H. Ghayesh, C. Hameury, H. Hena Zamal, Nonlinear
258 vibrations and viscoelasticity of a self-healing composite cantilever beam: Theory and
259 experiments, Composite Structures, 294 (2022) 115741.
260 [107] Y. Shen, A. Vizzaccaro, N. Kesmia, T. Yu, L. Salles, O. Thomas, C. Touzé, Comparison
261 of Reduction Methods for Finite Element Geometrically Nonlinear Beam Structures, Vibration,
262 4 (2021).
263 [108] B. Cochelin, C. Vergez, A high order purely frequency-based harmonic balance
264 formulation for continuation of periodic solutions, Journal of Sound and Vibration, 324 (2009)
265 243-262.
266 [109] L. Woiwode, N.N. Balaji, J. Kappauf, F. Tubita, L. Guillot, C. Vergez, B. Cochelin, A.
267 Grolet, M. Krack, Comparison of two algorithms for Harmonic Balance and path continuation,
268 Mechanical Systems and Signal Processing, 136 (2020) 106503.
269 [110] T. Detroux, L. Renson, L. Masset, G. Kerschen, The harmonic balance method for
270 bifurcation analysis of large-scale nonlinear mechanical systems, Computer Methods in
271 Applied Mechanics and Engineering, 296 (2015) 18-38.
272 [111] J. Chung, G.M. Hulbert, A Time Integration Algorithm for Structural Dynamics With

Improved Numerical Dissipation: The Generalized-α Method, Journal of Applied Mechanics, 60 (1993) 371-375.

[112] V. Denis, A. Pelat, C. Touzé, F. Gautier, Improvement of the acoustic black hole effect by using energy transfer due to geometric nonlinearity, International Journal of Non-Linear Mechanics, 94 (2017) 134-145.

[113] H. Li, C. Touzé, A. Pelat, F. Gautier, X. Kong, A vibro-impact acoustic black hole for passive damping of flexural beam vibrations, Journal of Sound and Vibration, 450 (2019) 28-46.

[114] L. Zhang, X. Tang, Z. Qin, F. Chu, Vibro-impact energy harvester for low frequency vibration enhanced by acoustic black hole, Applied Physics Letters, 121 (2022) 013902.

[115] H. Li, C. Touzé, A. Pelat, F. Gautier, Combining nonlinear vibration absorbers and the Acoustic Black Hole for passive broadband flexural vibration mitigation, International Journal of Non-Linear Mechanics, 129 (2021) 103558.

[116] M.-X. He, Y. Tang, Q. Ding, Dynamic analysis and optimization of a cantilevered beam with both the acoustic black hole and the nonlinear energy sink, Journal of Intelligent Material Systems and Structures, 33 (2021) 70-83.

[117] T. Wang, Y. Tang, T. Yang, Z.-S. Ma, Q. Ding, Bistable enhanced passive absorber based on integration of nonlinear energy sink with acoustic black hole beam, Journal of Sound and Vibration, 544 (2023) 117409.

[118] L. Zhang, G. Kerschen, L. Cheng, Nonlinear features and energy transfer in an Acoustic Black Hole beam through intentional electromechanical coupling, Mechanical Systems and

Signal Processing, 177 (2022) 109244.

[119] A.H. Nayfeh, W. Lacarbonara, C.-M. Chin, Nonlinear Normal Modes of Buckled Beams: Three-to-One and One-to-One Internal Resonances, Nonlinear Dynamics, 18 (1999) 253-273.

[120] W. Lacarbonara, Nonlinear structural mechanics: theory, dynamical phenomena and modeling, Springer Science & Business Media, 2013.

[121] M. Amabili, Nonlinear damping in large-amplitude vibrations: modelling and experiments, Nonlinear Dynamics, 93 (2018) 5-18.

[122] P.F. Pai, T.J. Anderson, E.A. Wheater, Large-deformation tests and total-Lagrangian finite-element analyses of flexible beams, International Journal of Solids and Structures, 37 (2000) 2951-2980.

[123] P.F. Pai, Problems in geometrically exact modeling of highly flexible beams, Thin-Walled Structures, 76 (2014) 65-76.

[124] J. Webb, Imposing linear constraints in finite‐element analysis, Communications in applied numerical methods, 6 (1990) 471-475.

[125] T.M. Cameron, J.H. Griffin, An Alternating Frequency/Time Domain Method for Calculating the Steady-State Response of Nonlinear Dynamic Systems, Journal of Applied Mechanics, 56 (1989) 149-154.

[126] D. Tang, M. Zhao, E.H. Dowell, Inextensible Beam and Plate Theory: Computational Analysis and Comparison With Experiment, Journal of Applied Mechanics, 81 (2014).

[127] M. Peeters, R. Viguié, G. Sérandour, G. Kerschen, J.C. Golinval, Nonlinear normal modes, Part II: Toward a practical computation using numerical continuation techniques,

315 Mechanical Systems and Signal Processing, 23 (2009) 195-216.
316 [128] E.A. Coddington, N. Levinson, Theory of ordinary differential equations, Tata McGraw-
317 Hill Education, 1955.
318 [129] S. Ereiz, I. Duvnjak, J. Fernando Jiménez-Alonso, Review of finite element model
319 updating methods for structural applications, Structures, 41 (2022) 684-723.
320 [130] F. Riahi, On Lagrangians with Higher Order Derivatives, American Journal of Physics,
321 40 (1972) 386-390.
322 [131] D.L. Logan, A first course in the finite element method, Thomson, 2002.
323 [132] M. Amabili, P. Balasubramanian, G. Ferrari, Nonlinear vibrations and damping of
324 fractional viscoelastic rectangular plates, Nonlinear Dynamics, 103 (2021) 3581-3609.
325 [133] H. Benaroya, M. Nagurka, S.M. Han, Mechanical Vibration: Theory and Application,
326 Rutgers University Press, 2022.
327 [134] L. Tang, L. Cheng, Loss of acoustic black hole effect in a structure of finite size, Applied
328 Physics Letters, 109 (2016) 014102.
329